TIME-RESOLVED MAGNETIC MICROSCOPY USING NEAR- AND FAR-FIELD PICOSECOND HEATING

A Dissertation

Presented to the Faculty of the Graduate School

of Cornell University

in Partial Fulfillment of the Requirements for the Degree of

Doctor of Philosophy

by

Jason Bartell

August 2018

TIME-RESOLVED MAGNETIC MICROSCOPY USING NEAR- AND FAR-FIELD PICOSECOND HEATING

Jason Bartell, Ph.D.

Cornell University 2018

Advanced magnetic microscopies are key to advancing our understanding and application of novel magnetic phenomenon such as skyrmions, spinwaves, and domain walls. However, due to the diffraction-limit of light, achieving the 10 – 100 nanometer spatial resolution and 10 – 100 picosecond temporal resolution required to image these phenomena is beyond the reach of table-top techniques. My dissertation research has been to develop stroboscopic magnetic microscopy techniques that use picosecond thermal gradients to transduce magnetization into a voltage. In magnetic metals, this is accomplished via the anomalous Nernst effect and in ferromagnetic insulator/heavy metal bilayers the signal is due to the longitudinal spin Seebeck effect detected via the inverse spin Hall effect. Using focused, 3 ps laser pulses to heat cobalt and permalloy films, I demonstrate that the anomalous Nernst effect can image magnetization with 10-100 ps temporal resolution, sub-micron spatial resolution, and sensitivity to the in-plane moment of $0.1°/\sqrt{Hz}$. I then show how this sensitivity and resolution can be applied for phase-sensitive ferromagnetic resonance imaging in ultrathin YIG/Pt bilayers in which we observe spatial variation of the resonance field, amplitude, phase, and linewidth. To conclude, I present the development of a near-field scanning optical microscope to create nanoscale thermal gradients and achieve spatial resolution of magnetic textures below the diffraction limit. The advent of these far- and near-field magneto-thermal imaging techniques will enable the table-top measurement of nanoscale magnetization dynamics in thin film devices.

BIOGRAPHICAL SKETCH

Jason Bartell is from State College, PA. He is the son of Kathy and Rodrick Bartell, small business owners, and brother to Nathan and Laura. Jason was homeschooled from the third grade, eventually attending Pennsylvania State University where he met his wife, Lena, and graduated in 2011 with a B.S. in Physics. Enjoyment of physics led him to pursue a PhD in Applied Physics at Cornell University.

To Mom, Dad, Nathan, Maddie

and, most of all, Lena.

ACKNOWLEDGMENTS

Getting to this point, is the result of a lifetime of love, support, and guidance from a vast community spread over different parts of the country. I can never repay my debt to these people; however, I can acknowledge them here, with a few lines, trusting they know much is being left unsaid. This section is a general acknowledgement of a few key players, unfortunately I do not have the space to include everyone here, my sincerest apologies to you all.

The process of becoming a scientist has been the direct result of mentorship from many great scientists. In particular my research advisor, Greg Fuchs, has provided me with invaluable direction, showing me how to operate equipment, finding holes in my arguments, and being a role model. He makes it look easy to be a productive researcher, a broadly knowledgeable scientist, and a good person, even though I know it is not. Thank you to Dan Ralph for joining my committee somewhat last minute as well as for many insightful comments, questions, and suggestions during IRG meetings and while writing papers. To Darrell Schlom, thank you for directing me to get a background in materials science, particularly its view of thermodynamics and kinetics which was helpful to this work. Thank you also, to Alex Gaeta who served on my committee for the majority of my time and provided helpful guidance during the A-exam. I am also exceedingly grateful to my mentors at Penn State: to my research advisor Peter Schiffer, working in his lab is how I first knew I really wanted to do research, and to my academic advisor Richard Robinett, his advice set me in the right direction and his genuine concern for his many advisees was an inspiration.

I would like to thank the entire Fuchs group for making my time fun and productive. In particular, Darryl Ngai, for being my partner while building the microscope for MOKE and developing TRANE, and Jonathan Karsch, who did a lot of pioneering work on tip fabrication

and numerical calculations. Thank you to Evan MacQuarrie, Isaiah Gray, Feng Guo, and Emrah Turgut for all the help in lab, breaking down cardboard boxes, and coffee break conversations. Thank you also to Nick Jungwirth, Yun-Yi Pai, Austin Moehl, Albert Park, Huiyao Chen, and Krishnan Chandler for being great lab mates to work with.

Thank you to the Cornell facility staff that make so much of the research actually move forward: Nate Ellis for being the best machine shop teacher I could ask for, Cynthia Reynolds for helping me navigate Cornell paperwork, Keane Leitch for helping to keep us safe, and Steve Kriske for doing the Sisyphean work of keeping CCMR equipment working. I would also like to acknowledge Dr. Long Ju, for helpful comments and suggestions related to using gold coated Si cantilevers, and Dr. Samuel Berweger for conversations regarding shear-force microscopy and adiabatic nanofocusing.

Becoming a happy, healthy human being is thanks to my Family. My mom and dad, Kathy and Rod, taught me to be curious, think for myself, and be always do my best. They have always been patient and supportive of what I wanted to do even if they do not understand it all the time. My brother Nathan has been my friend all my life and was the first one to teach me that there is always somebody better than you, so be humble and make friends. Finally, to my wife, Lena, thank you for being my partner in this exciting and crazy adventure. I am so proud to be your husband and cannot imagine life without you.

Outside of the lab, I have been blessed by an outstanding group of friends. To my Fallen Creek family, Evan, Greg Stiehl, Ed Lochocki, Sam Ahles, Jessica Abueg, Summer Sarif, Eamonn O'Shea, and Coralie Salesse-Smith, it's been class. What is Thread can never die. To Brett Scheiner, Joel Sleppy, Mickey Carignano, Sam Kachuck, and Kacey Wochna, thank you all for the shared complaints, drinks, meals and hikes.

TABLE OF CONTENTS

LIST OF FIGURES

LIST OF TABLES

CHAPTER 1

INTRODUCTION

When spins of unpaired electrons or orbitals in a material interact and there is a preferential orientation they are magnetic. This is, fundamentally, a quantum interaction that scales up to have macroscopic effects, for instance applying force at a distance. To anybody learning about magnets for the first time, these effects are at first puzzling and then useful, a pattern that has continued to the micrometer and nanometer scales. In nanoscale devices and thin-films, one of the fundamental questions is, what is the magnetization inside the material? This question has been answered in a variety of ways and the work in this dissertation has been centered around a new way of answering this question. Measuring the magnetization inside of a magnetic material is of fundamental importance because interactions within a magnetic material often present as changes in the magnetization. Furthermore, if you want to use magnetic materials for some application then the magnetization and its interaction with external forces determines the device behavior.

In recent decades, magnetic materials have made the biggest impact in information storage. The discovery of giant magnetoresistance (GMR) in 1988 [1], which ultimately won a Nobel prize, laid the foundation of modern hard drives which have increased in density to the point where it is now possible to store over 2 terabytes per square inch [2]. The nonvolatility, radiation hardness, efficiency of storage, and density have motivated research in alternative forms of magnetic information storage in which single bits are written and read electronically using spin-transfer torques. This has been developed into a solid state magnetic random access memory, MRAM, which has speed and energy efficiency advantages over purely charge-based RAM [3].

Microwave circuit components are another area where magnetic materials currently play an important role and where there are active efforts to increase efficiency and decrease size using thin films. Magnetic circulators, isolators, and filters play an invaluable role in modern communication and sensing by making use of the gigahertz resonance of ferromagnetic garnets and the breaking of time-reversal symmetry [4]. Recently, it has been shown that by using spin torque, nanoscale microwave sources can be created and coupled together via spin waves [5,6]. Using antiferromagnetic materials, it may even be possible to create THz frequency sources and components [7,8], although this work is still in its early stages.

As promising as the different applications are, to fully develop them we need to know and/or control the magnetic moment of the material. It is often insufficient to rely on bulk measurements because magnetization can vary on nanometer length scales. In these cases magnetic imaging is required. There are a fairly large number of magnetic imaging techniques, but broadly speaking, they can be classified by the magnetic interaction: measuring the stray field above a sample, measuring the response of electrons, and measuring a magneto-optical interaction.

Measuring the stray field from the surface of the sample is the oldest method of imaging the orientation of the magnetization in a material starting with small magnetic particles that were used to see magnetic domains in iron. The current state of the art relies on a scanning probe geometry. The primary techniques are magnetic force microscopy, MFM [9], scanning superconducting quantum interference device (SQUID) microscopy [10], and scanning nitrogen vacancy (NV) center microscopy [11–13]. Magnetic resonance force microscopy, MRFM [14,15], is related to MFM but it deserves to be mentioned separately since it is the only scanning stray-field based system to measure magnetic dynamics. The lack of true time-domain

resolution is a chief drawback of most stray field measurement methods. Nevertheless, these techniques are some of the most sensitive, capable of detecting the spin of a single electron [16].

The second broad category of magnetic microscopy techniques is based on measuring the interaction of electrons with a magnetized material. The most common of the electron-based magnetic microscopies is Lorentz transmission electron microscopy (TEM) in which electrons passing through a film experience a Lorentz force due to the local magnetization bending their path to the detector. By measuring the deviation of the electron path on the detector the local in-plane magnetization vectors can be reconstructed [17,18]. As an electron microscopy technique, Lorentz TEM has nanometer spatial resolution and has recently been shown to be capable of fs resolution in custom systems [19,20]. In Lorentz TEM, the high spatiotemporal resolution has the drawback of requiring careful sample preparation and has only a limited range of in-situ sample environments (temperature, field, etc.). Spin-polarized scanning tunneling microscopy (STM) is the other dominate electron-based magnetic microscopy [21]. Unlike Lorentz TEM in which electrons pass through a sample, spin-polarized STM measures the tunneling of electrons into the surface of a sample. If the electrons tunneling from the tip to the sample are spin-polarized by means of a magnetic tip, the tunneling probability will depend of the magnetization of the sample. The atomic resolution of STM is maintained enabling spin-polarized STM to measure and control the moments of single atoms [22]. Although time-resolved spin-polarized STM has yet to be demonstrated, time-resolved unpolarized STM has been [23], suggesting that femtosecond, atomic resolution magnetic microscopy is possible in principle. The biggest disadvantage of spin-polarized STM is that it is so sensitive to the surface that many samples of interest are not measurable. In addition, insulating magnetic samples must be thin enough to tunnel through only a few atomic layers. The last electron-based microscopy worth mentioning is

scanning impedance microscopy or scanning microwave microscopy [24]. This is an inherently dynamical technique in which a microwave antenna is brought into the near-field of the sample and the absorption is measured. If there is ferromagnetic resonance of the sample under inspection the scattering parameters of the antenna are changed. The resolution of this technique is on the order of the antenna, typically tens of nanometers, and the range of frequencies can be tens of gigahertz.

The last category of magnetic microscopy techniques is magneto-optical microscopy. The most common form of magneto-optical microscopy measures the change of polarization of light when it reflects of a surface, Kerr effect microscopy, or passes through it, Faraday effect microscopy. Since the first demonstration by Foyler and Fowly [25,26], Kerr and Faraday effect microscopy has become ubiquitous in studies of magnetism thanks to the advent of inexpensive, high quality light sources, optics, photodetectors, and cameras. Femtosecond pulsed lasers in particular have given magneto-optical techniques higher temporal resolution than the other magnetic microscopies, enabling study of ultrafast magnetic dynamics [27]. Unfortunately, the spatial resolution of magneto-optical microscopy is still restricted by the diffraction limit to have Abbe resolution of $\frac{\lambda}{2\,NA}$, where λ is the wavelength of the light and NA is the numerical aperture of the lens. By using x-rays the spatial resolution has been demonstrated down to 10-21 nm [28,29]. X-ray imaging is typically accomplished either by using a zone plate to focus the x-rays or by diffractive imaging techniques [30,31]. In addition to the higher resolution, x-rays can access the inner shell electrons so that imaging can be done with elemental selectivity.

The focus of this dissertation is the development and application of a fourth class of magnetic imaging technique, time-resolved magneto-thermal magnetic microscopy. Magneto-thermal microscopy uses the voltage generated by local, thermally driven flux of electrons or

magnons to image the magnetization in a thin film. It is distinguished from the other categories of magnetic microscopy by the role of non-equilibrium of thermodynamics plays in coupling heat flow to magnetization. As such, magneto-thermal microscopy falls in to the category of spin caloritronics and is the first application to come out this burgeoning field [32,33]. The work presented here advances the state of the art in magneto-thermal imaging by demonstrating the ability to measure magnetic metals and insulators with sub-optical diffraction limited spatial resolution and picosecond temporal resolution.

This dissertation describes the development and application of a time-resolved, magneto-thermal microscopy technique and is organized as follows: Chapter 2 provides an overview of the background useful for implementing and interpreting time-resolved anomalous Nernst effect (TRANE) and time-resolved longitudinal spin Seebeck effect microscopy (TRLSSE). Chapter 3 presents our demonstration of TRANE in Co and $Ni_{20}Fe_{80}$ (permalloy, Py) films which shows that the spatiotemporal resolution is determined by the thermal gradient. In Chapter 4, we show TRLSSE microscopy is capable of sub 100 ps temporal resolution in magnetic insulator, normal metal bilayers and apply it to the observation of spatially varying coherent magnetization dynamics in uniformly driven, epitaxial thin film yttrium iron garnet ($Y_3Fe_5O_{12}$), platinum multi-layers. A path toward truly nanoscale resolution with magneto-thermal effects is established in Chapter 5 and Chapter 6. Three different near-field heating, scanning probe geometries are tested in Chapter 5 and we find that sub-diffraction limited spatial resolution is possible. Chapter 6 contains the experimental details of the development and operation of the scanning probe geometry.

CHAPTER 2

SCIENTIFIC BACKGROUND

2.1 The anomalous Nernst effect

The anomalous Nernst effect (ANE) is the generation of a transverse electric field when charges, driven by a thermal gradient, move through a material with broken time-reversal symmetry. In magnetic materials it can be described concisely by $\mathbf{E} = -\mathbf{N}\,\mu_o\mathbf{M} \times \boldsymbol{\nabla}\mathrm{T}$. Here, **E** is the electric field, **N** is the Nernst coefficient, **M** is the magnetization, T is temperature, and μ_o, is the permeability of free space. Bolded letters represent vectors. It is useful to look more closely at the underlying physics of the ANE: how it relates to thermoelectric and thermomagnetic effects, its relation to the anomalous Hall effect (AHE), and how it is measured.

The ANE is the Nernst effect where time-reversal symmetry is broken by a material instead of an external magnetic field. To describe this in more detail, we begin with a discussion of thermoelectric effects, then discuss them in terms of thermomagnetic effects in general, including the Nernst effect, and finally we conclude by relating the Nernst effect to the transverse conductivity via the Mott relation. The following discussion is based largely on refs [34–36].

For out-of-equilibrium, extensive subsystems (primed and unprimed) with parameters *X'* and *X* we can define a general diving force, known as the affinity, ζ, by,

$$\zeta_k \equiv \left(\frac{\partial S^o}{\partial X_k}\right)_{X_k^o} = \frac{\partial S}{\partial X_k} - \frac{\partial S'}{\partial X_k'} = z_k - z'_k \qquad (2.1)$$

Where *S* and *S′* are the entropy of the two different subsystems, $S_k+S'_k=S_k^o$, and $X_k+X'_k=X_k^o$. Using the affinity, we can write the rate of entropy production in the continuous limit as,

$$\frac{dS}{dt} = \sum_k \nabla\zeta_\mathrm{k} \cdot \mathbf{J}_\mathrm{k} \tag{2.2}$$

where $\mathbf{J_k} = \frac{dX_k}{dt}$ is the flux vector. The flux is ultimately the thing of interest, if we assume a Markovian system and linear response we get

$$\mathbf{J}_\mathrm{k} = \sum_j L_{jk}\zeta_j \tag{2.3}$$

where L_{jk} are the kinetic coefficients and functions of the instantaneous local intensive variables. Somewhat non-intuitively, this shows that the flux of a parameter does not just depend on its own affinity, but on the affinities of the other parameters as well. In addition, this gives us a framework to relate the different thermoelectric effects by their measurable coefficients, although writing out all of these relations is beyond the scope of this work. To deal with magnetic fields in this framework, we can apply Onsager reciprocity such that $L_{jk}(\mathbf{H}) = L_{kj}(-\mathbf{H})$. This leads to transverse voltages which, for the case of the anomalous Nernst effect, allows us to relate thermomagnetic effects and thermoelectric conductivity to transport measurements.

The Mott relation relates the Seebeck coefficient to the electrical conductivity. For the anomalous Hall conductivity, σ_{xy}, the anomalous Nernst coefficient is given by [37,38]

$$N = \frac{1}{3}\left(\frac{\pi k_b}{e}\right)^2 e\,T\,\frac{d\left(\sigma_{xy}(E)\right)_\mu}{dE} \tag{2.4}$$

where k_b is Boltzman's constant, e is the electron charge, E is the electric field, and μ is the chemical potential. This relation may also be useful for developing materials with large anomalous Nernst coefficients [38]. While this thermodynamic understanding is helpful in getting a physical picture of what happens when a thermal gradient is applied across a sample, measurements are the only way to really know the Nernst coefficients.

Researchers measure the ANE using three different measurement geometries. The first geometry is a bulk measurement in which a constant temperature gradient is applied in one direction. Most commonly, this is done by clamping one end of the sample to a heater and another end to a heat sink and performing the measurement in vacuum. The key advantage of this technique is that the temperature gradient can be well-known because the whole sample can be assumed to be at a steady state. It is important to note that the analysis is made significantly more complicated if there is any thermal gradient between layered materials or if the substrate is conducting.

The second measurement configuration uses on-chip heating wires [39,40]. The challenge in this case is to be able to quantify the actual thermal gradient across the sample. Different thermal conductivities between the substrate and film of interest, and the thermal resistance at interfaces must be taken into account [41]. To make the temperature estimate more accurate, sensing wires are fabricated on-chip and numerical calculations can be used to determine gradients. Substrate effects can be mitigated by using suspended nitride films measured in vacuum. The membranes are not very thermally conducting so most of the heat travels through the film in one dimension [42]. The process for fabricating these samples, and the substrate, limits sample geometry and materials.

The third primary heating technique is laser heating [43], and it is the technique presented in this dissertation. In laser heating measurements, a pulsed or CW laser is focused onto a thin film that has been patterned into a channel or Hall bar. The voltage across the device is measured as a function of laser power. Although we focused on using the Nernst effect for microscopy, it is possible to determine the Nernst coefficient using laser heating as we show in Chapter 3 and as

was also done in Refs. [44–46]. The main challenge with this technique is accurately determining the heating from the laser, which results in large uncertainties.

2.2 The longitudinal spin Seebeck effect

The longitudinal spin Seebeck effect is the generation of angular momentum flux using a thermal gradient parallel to the direction of a thermal gradient. Named by analogy to the electrical Seebeck effect, the LSSE is the other magneto-thermal effect that we use for microscopy in this dissertation. The LSSE is distinct from the transverse spin Seebeck effect [47,48], and the spin-dependent Seebeck effect, in which charge carriers driven by spin current are spin polarized because they are in a magnetic material. Discussion and application of these effects is beyond the scope of this work. The longitudinal configuration is most convenient because the interpretation of the voltage signals is less complicated by complex thermal profiles at interfaces [41].

The LSSE was first observed in ferromagnetic insulators in 2010 [49], although previous claims of the transverse spin Seebeck effect likely also had a contribution. The existence of the effect was expected based on the same arguments that lead to the Seebeck effect, nevertheless, detection proved challenging because the it required detecting spin transport in ferromagnetic insulators. After the discovery of the spin Hall effect and its inverse [50–53], research in spin transport at ferromagnetic interfaces proceeded rapidly because there was finally a way to measure the angular momentum without the added complication of a metallic ferromagnet.

A mathematical description of the LSSE is typically given either in terms of a three-temperature model [41] or a magnon transport model [54,55]. The magnon model typically begins with a Bose-Einstein distribution of magnons. The magnons then diffuse in the presence of a thermal gradient. This model starts from a more fundamental assumption of a distribution of

spin-waves and provides a good starting point for extrapolating to other thermally driven spin transport and magnon-phonon effects. These include the antiferromagnetic spin Seebeck effect [56] and the magnon-phonon coupling [57]. The primary drawback of the model is that it does not offer much intuitive guidance to experimentalists. Thus, the three-temperature model is often an easier tool for numerical modeling and gaining intuition.

In the three-temperature model, electrons, phonons, and magnons experience an effective temperature, T and have a heat capacity, c [58]. The different particles and quasi-particles at different temperatures can exchange energy with a characteristic relaxation time, τ. Thus, for magnons, the rate of the magnon temperature change can be described by Eq. (2.5).

$$\frac{dT_{magnon}}{dt} = \frac{c_{magnon}}{c_{magnon} + c_{photon}} \frac{T_{phonon} - T_{magnon}}{\tau_{magnon-phonon}} \tag{2.5}$$

The rate of heat transfer between magnons and electrons, and between phonons and electrons can be defined in the same manner. If observation of the LSSE relies on the transfer of energy from phonons to magnons, due to the lack of free electrons in the insulator, the relaxation becomes a bottle neck of ~ 200 ps. This has important implications for the work in this dissertation; if the LSSE only responds over time scales of hundreds of picoseconds, then it will not make a good stroboscopic probe of the magnetic state at gigahertz frequencies.

Before our measurements of YIG/Pt, there were several studies to try and understand the time-dependence of the LSSE. Optical heating has been the workhorse to study this question by virtue of its short heating times. In initial studies relied on MHz frequency modulation of CW laser heating with 50-50 duty cycles [59,60]. The most compressive study found that the LSSE response to laser heating had a frequency dependence and that thicker films has a lower cutoff frequency. They ultimately calculated that the magnon-phonon relaxation rate was ~100 ps in the 30 nm thick films [59].

Pulsed laser heating, using femto, or picosecond pulse durations, provides enhanced temporal resolution and reveals that the time-dependence of the LSSE is not entirely described by a single relaxation constant. In the Myers group, they have used femtosecond pulses to heat YIG crystals microns away from a Pt wire that measured the LSSE. They concluded that the pulsed nature of the laser primarily raised the global temperature of the YIG and that long-wavelength magnons best explained their findings [61]. Meanwhile, local measurements presented in Chapter 4, and time-resolved magneto-optical measurements done by the Cahill group [62] suggest that this interaction can be picoseconds, although it may be strictly at metal/insulator interfaces. All told, the different measurements suggest that thermally generated magnons can exist over a wide range of energies, the short wavelength magnons likely decay before they can propagate very far. Most importantly for this work however, thermal gradients can be generated and detected in picoseconds, enabling time-resolved measurements of magnetization.

CHAPTER 3

TOWARDS A TABLE-TOP MICROSCOPE FOR NANOSCALE MAGNETIC IMAGING USING PICOSECOND THERMAL GRADIENTS [63]

3.1 Chapter abstract

Research advancement in magnetoelectronics is challenged by the lack of a table-top magnetic measurement technique with the simultaneous temporal and spatial resolution necessary for characterizing magnetization dynamics in devices of interest, such as magnetic memory and spin torque oscillators. Although magneto-optical microscopy provides superb temporal resolution, its spatial resolution is fundamentally limited by optical diffraction. To address this challenge, we study heat rather than light as a vehicle to stroboscopically transduce a local magnetic moment into an electrical signal while retaining picosecond temporal resolution. Using this concept, we demonstrate spatiotemporal magnetic microscopy using the time-resolved anomalous Nernst effect (TRANE). Experimentally and with supporting numerical calculations, we find that TRANE microscopy has temporal resolution below 30 ps and spatial resolution determined by the area of thermal excitation. Based on these findings, we suggest a route to exceed the limits imposed by far-field optical diffraction.

3.2 Introduction

Recent advances in magnetoelectronics have demonstrated the potential for spin-based technology, including magnetic random access memory [64,65], nanoscale microwave sources [66,67], and ultra-low power signal transfer [68]. Magnetic microscopy has played a fundamental role in these areas through the illumination of magnetic behavior such as domain wall motion [69,70], magnetic switching [71], and spin wave propagation [72]. Advanced microscopy techniques capable of examining local magnetization dynamics at length and time

scales fundamental to spatiotemporal variations in magnetic systems [73] – typically 10-200 nm [74–78] and 5 – 50 ps – would enable engineering advances and new scientific discoveries.

Currently, magneto-optical measurements are the only table-top approach to stroboscopically measure spatially varying magnetic dynamics. Unfortunately, the spatial resolution available to optical measurements is limited by diffraction to approximately $\lambda/(2\,NA)$, where λ is the wavelength of light and NA is the effective numerical aperture of the focusing optics. Therefore, optical techniques, including the time-resolved magneto-optical Kerr effect (TRMOKE), have a diffraction limited resolution of roughly 200 nm using blue light. One solution is to use radiation with a nanometer-scale wavelength, as in X-ray magnetic circular dichroism (XMCD) experiments, which provide spatial resolution down to 30 nm and time-domain resolution of less than 100 ps [79]. Unfortunately, spatiotemporal XMCD requires synchrotron-based sources which limits its wide-spread use.

To circumvent the spatial limitation imposed by optical diffraction, we propose a new technique for magnetic spatiotemporal microscopy that uses the interaction between magnetization and heat, rather than light. Our method is based on the time-resolved anomalous Nernst effect (TRANE). The geometry for TRANE is depicted in Figure 3.1a. The anomalous Nernst effect (ANE) is a magnetization-dependent, thermoelectric effect [80–82] in which a thermal gradient, transverse to the film's magnetic moment generates an electric field, $\vec{\mathbf{E}}_{\mathbf{ANE}}(\vec{\mathrm{x}},\mathrm{t})$, given by [39]

$$\vec{\mathbf{E}}_{\mathbf{ANE}}(\vec{\mathbf{x}},\mathrm{t}) = -N\,\vec{\boldsymbol{\nabla}}\mathbf{T}(\vec{\mathbf{x}},\mathrm{t}) \times \mu_o \vec{\mathbf{M}}(\vec{\mathbf{x}},\mathrm{t}), \tag{3.1}$$

where N is the anomalous Nernst coefficient, $\vec{\boldsymbol{\nabla}}\mathbf{T}(\vec{\mathbf{x}},\mathrm{t})$ is the thermal gradient, and $\vec{\mathbf{M}}(\vec{\mathbf{x}},\mathrm{t})$ is the magnetic moment. Previous studies have demonstrated that by confining $\vec{\boldsymbol{\nabla}}\mathbf{T}(\vec{\mathbf{x}},\mathrm{t})$ to a micron-scale region in a thin-film ferromagnetic metal, an anomalous Nernst voltage is generated that is

proportional to the local magnetic moment [43,83]. This has inspired proposals for applications that include microscopy and spectroscopy [32,43,83,84]. Up until this point, demonstrations and proposals have used thermal gradients that change slowly and heat a relatively large area of the sample under investigation. Here, we use a localized, pulsed thermal source with a short duty cycle from a focused laser to show E_{ANE} can be localized in both time and space to generate a TRANE signal. By synchronizing a magnetic excitation with thermal pulses, we use TRANE microscopy for stroboscopic measurement of magnetization dynamics.

3.3 Magnetic measurement with pulsed thermal gradients

Figure 3.1b shows a schematic of the measurement setup. We focus a pulsed laser to generate a short-lived, local temperature gradient for each optical pulse, thus creating a corresponding voltage pulse, V_{ANE}. A time-domain homodyne technique is used to convert the V_{ANE} pulses to a DC voltage, V_{TRANE}, which is measured with a lock-in amplifier. V_{TRANE} is proportional to the stroboscopically sampled local magnetization as described in section 3.8.1. In this experiment, we used 792 nm optical pulses with a fluence of 2.3 mJ cm^{-2}, which creates vertical thermal gradients of 3.3×10^{8} K m^{-1}, corresponding to a maximum temperature increase of 30 K (temperature measurement details in section 3.8.2). The first structure we studied was a 30 nm cobalt film patterned into a 18 μm wide cross-structure, shown in Figure 3.1b. Figure 1c shows a hysteresis curve of this sample measured using TRANE, which demonstrates the proportionality between the V_{TRANE} we measure and the local magnetic moment.

To test whether that the optically generated thermal gradients are short-lived, we perform a time-resolved measurement of the V_{ANE} pulses by electrically mixing them with 75 ps electrical reference pulses from a pulse generator (see Figure 3.1b). Figure 3.1d shows our measurement as a function of the delay between the reference pulses and the V_{ANE} pulses. We

find that the resulting signal has a roughly 75 ps full-width at half maximum (FWHM). These data can be understood as the temporal convolution of the V_{ANE} pulses with the reference electrical mixing pulses. Since the convolved signal width is similar to the reference pulse width, the V_{ANE} pulses must be shorter than 75 ps (details in section 3.8.5). As we show with subsequent magnetic resonance experiments, thermal gradients produced in our microscope are actually much shorter-lived.

We now discuss the signal sensitivity of TRANE microscopy, which is dependent on several factors, including the Nernst coefficient, the geometry, and the impedance. For the 18 μm cross structure, we calculate the magnetization angle sensitivity to be $0.73^o/\sqrt{Hz}$ (further information in section 3.8.6). Because of its picosecond duration, the TRANE signal is sensitive to the microwave impedance of the sample, with the strongest signal occurring when the sample impedance matches the 50 Ω impedance of the measurement circuit. In addition, the electrical TRANE signal scales as d^2/w for a probe diameter, d, and a channel width, w [43]. Thus a TRANE signal collected with a nanoscale excitation source (<200 nm) could remain large, provided that w is also scaled down. For comparison, the signal scaling of magneto-optical microscopy is essentially independent of the device geometry above the optical diffraction limit of $d \sim \lambda/(2\,NA) \sim$ 200 nm for blue light.

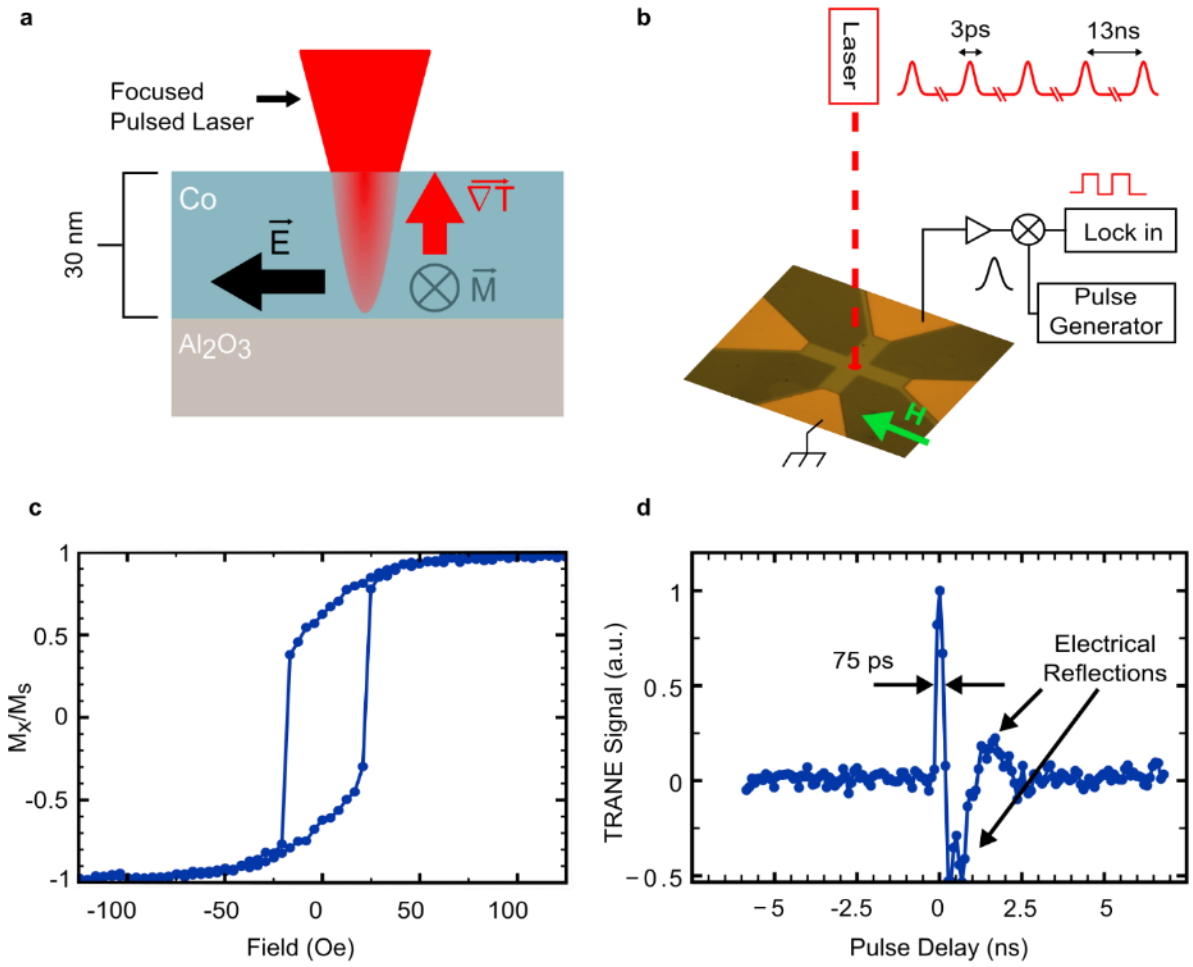

Figure 3.1 The time resolved anomalous Nernst effect for magnetic measurement. a, Schematic diagram of the anomalous Nernst effect in our measurements b, Schematic of the experimental setup. 792 nm pulsed laser light is focused to a diffraction-limited spot on the magnetic film patterned on top of a thermally conductive, electrically insulating substrate. Bonding pads enable detection of the TRANE voltage proportional to the perpendicular magnetic moment. c, TRANE measurement of local hysteresis in the cobalt cross, normalized by the value at saturation, M_s. d, Signal from mixing the ANE voltage pulse with a 75 ps electrical reference pulse. We observe that the width of the initial peak in the mixed signal is 75 ps, indicating that the ANE pulse is < 75 ps. The other, broader features are electrical reflections due to the impedance mismatch of the device and the 50 Ω transmission line.

3.4 Spatial measurement with focused pulsed thermal gradients

Next, we experimentally demonstrate that lateral thermal diffusion does not limit spatial resolution at the scale of a tightly focused laser by imaging the local magnetic moment of the cobalt cross. Scanning the laser across the sample, a map of the magnetization is created (shown in Figure 3.2a) in which, domain walls are visible where the projected moment is zero. For the cobalt films studied here, the domain walls are 150-200 nm wide [85], which is far below the 440 nm Abbe resolution limit we calculate for our apparatus. We use this fact to evaluate the resolution of our TRANE microscope by fitting spatial line cuts (Figure 3.2b) across a magnetic domain wall with the convolution of a step function and a Gaussian function of width, 2δ. The fit yields $\delta = 460 \pm 90$ nm (the fitting procedure is described in section 3.8.7). These results suggest that the main limitation to the spatial resolution is the size of the thermal gradient spot.

To gain a deeper understanding of thermal diffusion in our magnetic thin film samples, we performed time-dependent, finite element simulations of the picosecond heating dynamics. Using numerical simulations, we show in Figure 3.2d (blue curve) that when the laser pulse is at its maximum, the vertical component of the thermal gradient does not spread laterally beyond the pulsed heat source. Interestingly, our simulations show this statement is true even for a hypothetical nanoscale thermal source (dashed red curve in Figure 3.2d).

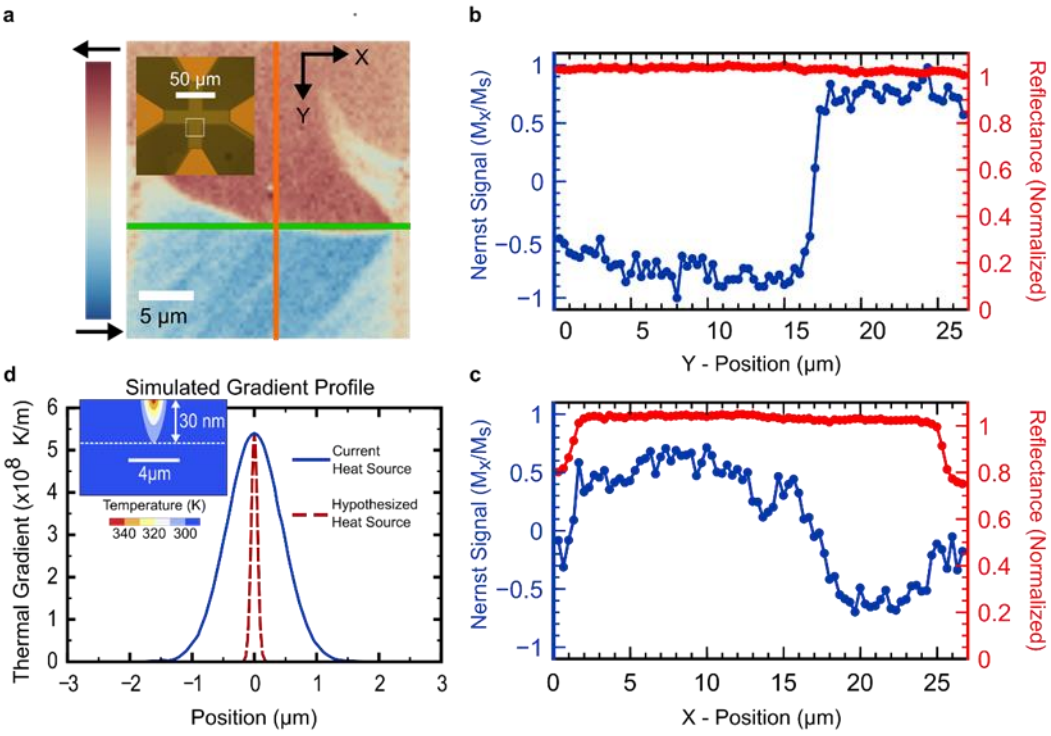

Figure 3.2 Spatial resolution of magnetic imaging using a thermal gradient. a, Image of magnetic structure taken with TRANE. b & c, Line cuts of the image showing the TRANE signal in blue (normalized by the value at saturation, Ms) and the simultaneously measured reflected light in red. b, line cut from top to bottom. c, line cut from left to right we note that the reflected signal drops off at the edge of the cross while the TRANE signal goes to zero without edge artifacts. d, Finite element, time dependent simulation of the vertical component of the thermal gradient at peak applied power along the x-axis as a function of distance from the spot center. The blue line corresponds to a heat source with a diameter equal to the experimental spot size with Abbe resolution of 440 nm. The dashed, red temperature profile corresponds to a hypothesized, nanothermal generation spot diameter of 50 nm, corresponding to a potential source from (for instance) a scanning probe with an Abbe resolution of 25 nm. The inset shows the x-z profile of the temperature at the center of the optical pulse. We note that, because of radial symmetry, the radial (in-plane) gradient gives no signal.

3.5 Stroboscopic measurement of magnetic dynamics

We study TRANE's temporal resolution by stroboscopically measuring ferromagnetic resonance (FMR) in $Ni_{20}Fe_{80}$ (permalloy) wires using the apparatus depicted in Figure 3.3a. To excite magnetization dynamics, a microwave frequency current is passed through an on-chip copper wire to generate an out-of-plane AC magnetic field in the permalloy. The wire axis of the sample is aligned parallel to the applied static magnetic field and the contacts are placed so as to measure the M_y component of the magnetization (perpendicular to both the wire axis and the excitation field). To measure V_{TRANE} for FMR measurements we use an additional step of lock-in detection to reference the signal to both the optical chopping frequency and to a small amplitude field modulation along the direction of the static magnetic field. The dual referenced lock-in detection allows us to reject the contribution from AC currents induced by microwave driving.

In this scheme, the precessing $M_y(t)$ is stroboscopically transduced by the short thermal pulse. By choosing a microwave drive frequency, ω, commensurate with the laser repetition rate, we create a constant relationship between the arrival of laser pulses and the phase of the excitation field. Starting from equation (1), the anomalous Nernst voltage generated at the sample's electrical pick-ups is $V_{ANE}(t) = -\beta\, N\, \nabla T_z(t) M_y(t)$. Because the magnetization precesses at frequency ω, it has a constant phase, ϕ, with respect to the laser repetition rate. Therefore, the expression simplifies to $V_{ANE}(t) \approx -\beta\, \nabla T_z(t)\, m_{y,prec} \cos(\omega t + \phi)$ where β is a proportionality constant and $m_{y,prec}$ is the precessional amplitude along y. The phase is determined by the relative delay between the laser pulses with respect to the AC magnetic excitation and defines which segment of the precessional cycle is probed. The final signal we measure after the amplifiers and mixer is described by an integral over the laser pulse period, T, such that

$$V_{TRANE} \propto m_{y,prec} \int_0^T \nabla T_z(\mathrm{t}) \cos(\omega t + \phi)\, dt. \qquad (3.2)$$

Thus, the magnetic moment is interrogated only when the temperature gradient, $\nabla T_z(t)$, is non-zero. In our case, numerical simulations (see Figure 3.3b) suggest that $\nabla T_z(t)$ is non-zero for approximately 10 ps. We note that if $\nabla T_Z(t)$ persists over a duration comparable to a half period of the precession, π/ω, then V_{TRANE} will integrate to nearly zero. Below we will use this fact to put an upper bound on the time duration of $\nabla T_Z(t)$ by measuring FMR at increasing frequencies. A complete discussion of the stroboscopic time resolution of TRANE microscopy is given in the section 3.8.1.

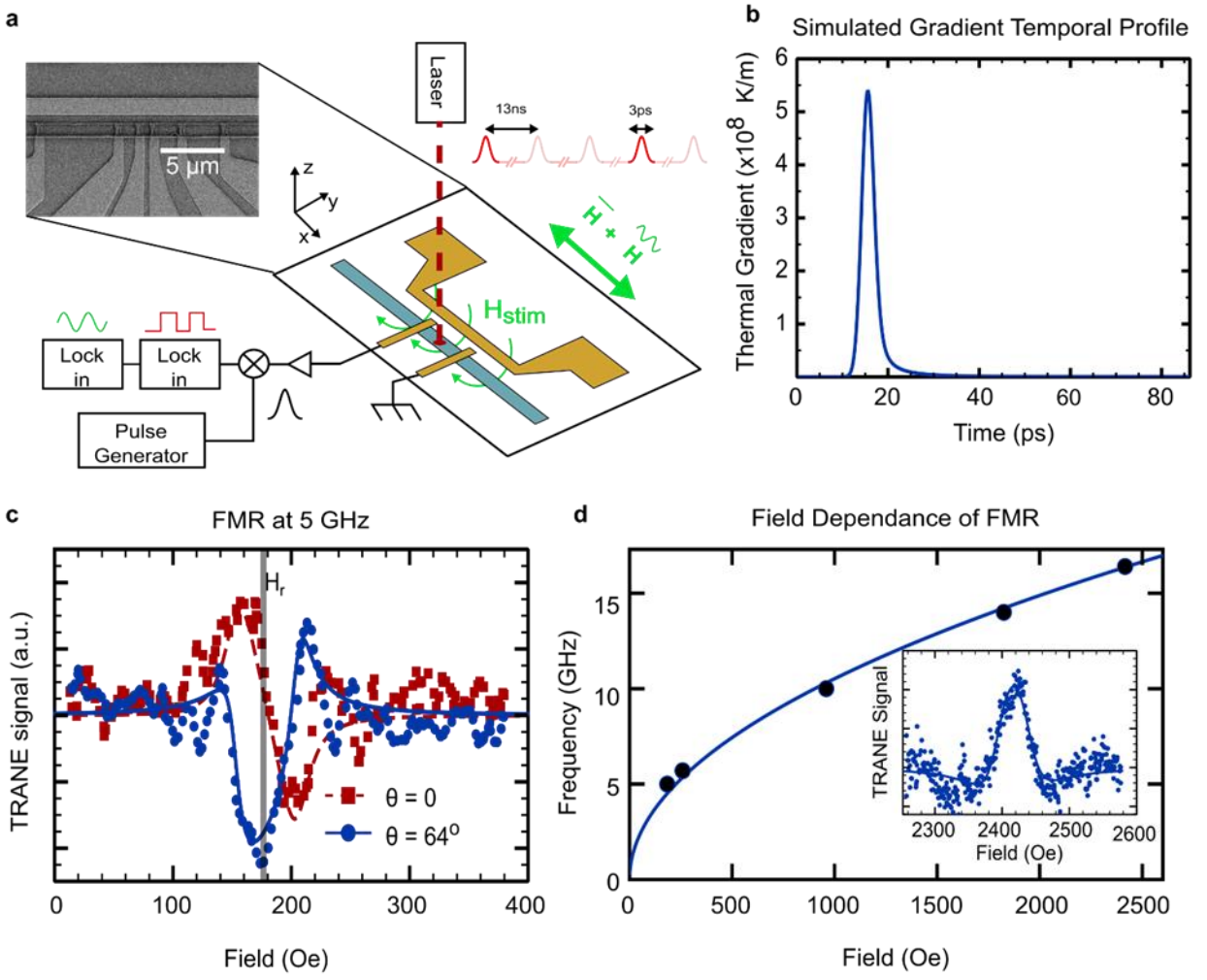

Figure 3.3 Measurement of magnetic dynamics using TRANE. a, Schematic of the experimental setup used to measure FMR in permalloy wires. The 2 μm wide permalloy wire (blue) is stimulated by a 2 μm copper wire 1 μm away from the permalloy wire. The contacts used to measure the TRANE signal were separated by 3 μm. b, Time dependent numerical simulation of the thermal gradient. c, FMR spectra measured using a 5 GHz excitation field and probed at two different phases in the precessional cycle. d, Plot of the resonant frequencies as a function of the resonant field determined by fitting. The solid line is a fit to the Kittel equation. An FMR spectrum measured at 16.4 GHz is shown in the inset. For all the FMR spectra, the points show the data after smoothing over 3 neighboring points. The lines are a fit to the linear combination of symmetric and anti-symmetric Lorentzians after accounting for the modulation frequency.

In Figure 3.3c we plot the stroboscopic TRANE measurement as a function of magnetic field and see an FMR peak corresponding to a maximum oscillation angle. The magnetization is excited by a 5.00 GHz stimulation to a maximum angle of 0.07° at 176 Oe. The measurement sensitivity is $0.093^o/\sqrt{Hz}$, which is improved from the cobalt cross sample chiefly because of the reduced sample width that increases the ratio d^2/w. Figure 3.3c shows two different phases of the same FMR frequency controlled by electrically shifting the time delay between the microwave magnetic field drive and the laser probe by 50 ps. The corresponding shift of the lineshape results from measuring the magnetic moment at a different part of the precessional cycle, testifying that the short-lived thermal gradient is a time-domain probe.

The FMR data are analyzed by fitting to linear combinations of symmetric and anti-symmetric Lorentzian functions modified to account for the magnetic field modulation (see section 3.8.8). From the fits, we extract a phase difference between the two of 64° ± 24°. The discrepancy from our expectation of a 90° shift might be due to phase drift between the excitation and the measurement on laboratory time scales, or because our model accounts only for a single, uniform FMR mode. Close inspection of the two data sets in Figure 3.3c reveals additional features that are anti-correlated between measurement phases. This suggests more complicated magnetic behavior than we model, including the existence of additional magnetic modes that may influence the accuracy of the phase we extract from fitting. Although full imaging and analysis of these modes is a capability of TRANE microscopy, their detailed study is beyond this scope of the present demonstration.

As we increase the frequency of the magnetic excitation, we find that (as expected) the FMR resonance field is well described by the Kittel equation, $\frac{\gamma}{2\pi}\sqrt{(H + N_z M_s)(H + N_y M_s)}$, as shown in Figure 3.3d, where γ is the gyromagnetic ratio and H is the applied field. Here, we use

demagnetizing factors N_y = 0.015, and N_z = 0.985, which are determined separately with measurements of the hard axis magnetic saturation. From these fits we find an effective magnetic moment $4\pi M_s$ = 840 emu/cm^3 and a Gilbert damping parameter, α = 0.009 ± 0.001. The damping in this sample is consistent with separate FMR measurements that we made by electrically monitoring the DC rectification voltage. These results are also in excellent agreement with literature values for permalloy [86,87]. The consistency among our various measurements and prior reports supports the idea that the local, transient heating of the sample during measurement does not significantly alter its dynamical properties as probed by TRANE microscopy.

As mentioned above, The FMR data shown in Figure 3.3d allow us to refine the upper bound of the thermal gradient lifetime. From Eq. (3.2) we see that for V_{TRANE} to stroboscopically measure periodic motion, the thermal gradient decay time must be shorter than one-half the period of magnetic precession, otherwise the signal would average to nearly zero. In the experiment, (inset to Figure 3.3d) we observe strong FMR spectra up to 16.4 GHz (period of 60 ps), which is the highest frequency that we can produce with our microwave electronics. Therefore, we conclude that the thermal gradient must decay in less than 30 ps. This is supported by our time-dependent finite element modeling (Figure 3.3b) which shows the thermal gradient pulse has a full width at half-maximum of 10 ps for these samples.

3.6 Discussion

Although the thermal spot size used in this demonstration is limited by optical diffraction, TRANE microscopy is a viable strategy for high spatiotemporal resolution. The ANE interaction time and the electron thermal carrier wavelength are both short in comparison to the scales of magnetic dynamics and the spatial variation of magnetization. Because thermal gradients are not fundamentally limited by optical diffraction, microscopy based on magneto-thermal interactions

has no fundamental barrier to decreasing the spatial resolution. Therefore, the spatiotemporal resolution of TRANE microscopy is predominantly limited by the generation and evolution of the localized thermal gradient. The thermal gradient diameter – and therefore the minimum resolvable feature – could be reduced below the far-field optical diffraction limit by scanning a light-confining plasmon antenna. Confined local heating using this approach has been previously demonstrated in the context of heat-assisted magnetic recording [88,89].

The above results demonstrate that for the thin film samples studied here, TRANE microscopy has temporal resolution below 30 ps and spatial resolution at the limit of focused light. Introducing this time-domain capability enables the use of TRANE for phase sensitive dynamical microscopy in cases of uniform ferromagnetic excitation as examined here, but it could also be used to image local relaxation dynamics in a pump-probe experiment. Applying these capabilities in a table-top imaging platform with potential for nanoscale spatial resolution could enable unprecedented access to time-resolved magnetization dynamics in support of the burgeoning field of high-speed magnetoelectronics.

3.7 Experimental methods

3.7.1 Sample preparation

For measurements of spatial resolution, 30 nm thick cobalt films were deposited by electron beam evaporation onto sapphire substrates. Photolithography and ion milling was used to pattern the films into square crosses as pictured in Figure 3.2a. For the spatial map of magnetization presented, the cross arms were 18 μm wide. Electrical contact was made by wire bonding to evaporated copper contacts.

The samples used for ferromagnetic resonance measurements were 30 nm thick $Ni_{20}Fe_{80}$ (permalloy) films deposited by DC magnetron sputtering at a base pressure below 10^{-7} Torr. The

films were patterned with e-beam lithography and ion milled into wires 2 μm wide and 950 μm long. Evaporated copper contacts 1 μm wide were fabricated to contact the permalloy wire with a range of separations to enable a DC impedance match close to 50 Ω. The contacts chosen for the measurement were 3 μm apart and had a DC resistance of 74 Ω. The wire we used as a microwave antenna to excite magnetization dynamics was fabricated in a lift-off process to be 2 μm wide, 50 μm long, and 102 nm thick. It was positioned 1 μm away from the permalloy wire and had a DC resistance of 48 Ω.

3.7.2 Thermal gradient generation

Local thermal gradients were generated by focusing light from a Titanium:Sapphire laser (Coherent MIRA 900 dual) tuned to 794 nm with 3 ps pulses and a fluence at the sample of 2.3 mJ/cm^2. The repetition rate was controlled with an electro-optic modulator/pulse picker. We used a repetition rate of 76 MHz for measurements of the spatial imaging and 25.3 MHz for the ferromagnetic resonance measurements. An optical chopper was used to modulate the optical pulse train at 9.7 kHz. To scan the beam, we used a 4-F optical path in combination with a voice-coil controlled fast-steering mirror. The light was focused into a diffraction-limited spot using a 0.90 numerical aperture air objective. The entire apparatus is on a 5 by 10 foot optical table.

To determine the temperature change induced by the laser pulses we measured the temperature increase using electrical measurements in conjunction with numerical simulations. The full temperature measurement analysis is presented in section 3.8.2.

3.7.3 Detection

To detect the V_{ANE} pulses during TRANE measurement of the magnetic moment, we connect the sample voltage contact to a microwave transmission line through a coplanar waveguide soldered to a type-K connector [90]. The signal is passed through a low-pass filter

with a 4 GHz break frequency to attenuate GHz frequency artifacts from inductive electrical coupling between the copper antenna and permalloy wire. After the filter, the signal is amplified by 40 dB with a 0.1-1 GHz bandwidth. The amplified pulse train is sent to the RF port of an electrical mixer, where it is mixed with a 1.5 ns pulse train from a pulse/pattern generator that is referenced to the laser repetition rate. When the two pulse trains temporally overlap on the mixer, a voltage modulated by the optical chopper (and, for FMR, the field modulation) is passed to a low-frequency preamplifier before being sent to a lock-in amplifier.

To determine the amplitude of V_{ANE} pulses prior to amplification and electrical mixing, we calibrated the transfer function of the V_{ANE} measurement circuit by measuring the signal produced by electrically generated reference pulses and systematically varying their widths. We find that our detection circuit transfer coefficient is 0.47 ± 0.04 for a 10 ps signal pulse (see section 3.8.9). Using this calibration, we measure that the anomalous Nernst coefficient in permalloy is $3.7 \pm 0.4\times10^{-6} \frac{V}{T\,K}$, which is consistent with previous reports [39,43,46] accounting for differences in the coefficient that arise due to variations in resistivity and thickness between samples [91].

3.7.4 2D imaging

Imaging the static magnetic moment is performed by measuring the V_{TRANE} along a channel perpendicular to the applied magnetic field so that the maximum signal was obtained during saturation of the magnetic moment. The multi-domain state was prepared by saturating the cross with a 130 Oe field and decreasing the field to 32 Oe. For the data in Figure 3.2a, we used a 250 nm step and a lock-in time constant of 500 ms.

3.7.5 FMR excitation

FMR was excited in the samples using a microwave signal produced by an arbitrary waveform generator (AWG) with a clock referenced to the laser repetition rate. This clock is multiplied up within the AWG to a sampling rate of 19.98 GS/s derived from the 25.3 MHz laser pulse repetition rate. The waveforms from the AWG can be delayed in steps of 50 ps with respect to the laser pulses without re-triggering, allowing resonant behavior of different phases to be observed. For excitation frequencies above 5.7 GHz, the output frequency of the AWG was doubled or quadrupled with electrical frequency multipliers to achieve frequencies up to 16.4 GHz. This excitation signal was then amplified to a power between 13-20 dBm and coupled to the copper stimulation wire.

3.7.6 TRANE detection of FMR

Ferromagnetic resonance was detected by using a second lock in with dual demodulation. In this technique, two modulation sources at different frequencies are used. The signal is extracted by first demodulating the input referenced to the optical chopper. The resulting signal is then sent to a second demodulator (time constant of 1 s) that is referenced to a 5-10 Hz modulation of the magnetic field.

3.8 Supporting theory and measurements

3.8.1 Independence between TRANE temporal resolution and circuit bandwidth.

This section shows how the temporal resolution of TRANE is only dependent on the lifetime of the thermal gradient, not on the bandwidth of the collection circuit. We discuss how the mixer is used to detect the pulsed signal and give relevant details pertaining to circuit bandwidth. An ideal frequency mixer outputs the voltage multiplication between two input ports. Here, we label one input the sample voltage and the second input as the reference or local

oscillator. If we set the local oscillator to a fixed frequency sine wave, then the mixer acts as a homodyne detector at the local oscillator frequency, producing a DC component at the output when the input is the same frequency as the local oscillator. Similarly, the mixer can be used to detect a pulse train. In this case, instead of a sine wave for the local oscillator, we use a reference pulse train with controllable duty cycle and relative delay.

To show the mixer output from a pulse train reference, we express the voltage multiplication in terms of a Fourier series expansion. Here, we define our Fourier expansion as

$$V(t) = \sum_k c_n e^{i\,2\pi kt/T}, \tag{3.3}$$

where T is the period and c_n are the Fourier coefficients defined as

$$c_n = \frac{1}{T}\int_{-T/2}^{T/2} dt\, V(t) e^{-i\,2\pi kt/T}. \tag{3.4}$$

By applying the Fourier series expansion, the DC component of the mixer output is

$$V_m = \frac{1}{V_0}\sum_{k=-K}^{K} c_k^s c_{-k}^r, \tag{3.5}$$

where c_k^s and c_{-k}^r are the Fourier components of the sample voltage and reference voltage respectively. We have a multiplicative factor V_0 which accounts for the amplifier circuit gain and total insertion loss. $K = f_{max}/f_0$ is the cutoff factor set by the bandwidth of the electrical components, f_{max}, with f_0 as the laser repetition rate. We can see from Eq. (3.5) that we can maximize the output signal by setting the reference to have the same Fourier components as the pulsed signal. As expected, with a pulse train as the input signal, it is best to mix with a pulse train as a reference.

The bandwidth of the collection circuit does not affect the temporal resolution of TRANE. To show this, without loss of generality, we assume the temperature gradient is

constant at the laser spot and 0 everywhere else. With this assumption, the time dependent ANE voltage V_{ANE} from the resistor model is given by

$$V_{ANE}(t) = \frac{\pi r^2}{w}(N\,M_s)\nabla T_z(t)m_y(t). \tag{3.6}$$

Where N is the Nernst coefficient, w is the voltage channel width, r is the thermal gradient lateral radius, and M_s is the magnetic saturation. This is for measurement of the y-axis component of the magnetic moment, m_y with a perpendicular-to-the-plane thermal gradient, ∇T_z. Applying this equation to Eq. (3.5), the measured voltage from the collection circuit can be expressed as

$$V_m(t) = \frac{1}{V_0}\left(\frac{\pi r^2}{w}\right)(N\,M_s)\sum_{k=-K}^{K} c_{-k}^{r}\int_{-T/2}^{T/2} dt\left(e^{i\frac{2\pi kt}{T}}\right)\nabla T_z(t)m_y(t). \tag{3.7}$$

The temperature gradient is non-zero only for a short time t_{ANE} ($t_{ANE} \approx 10$ ps according to numerical simulations). Using the fact that $t_{ANE} \ll 1/f_{max}$, which is true for the 1 GHz bandwidth circuit components, we can approximate the measured signal as

$$V_m(t) \approx \left[\frac{1}{V_0}\left(\frac{\pi r^2}{w}\right)(N\,M_s)\left(\sum_{k=-K}^{K} c_{-k}^{r}\right)\right]\int_0^{t_{ANE}} dt\,\nabla T_z(t)m_y(t). \tag{3.8}$$

This shows that TRANE measures the magnetic moment over the time period of t_{ANE}. Therefore, the time resolution of TRANE is determined by the lifetime of the temperature gradient and it is not limited by the frequency bandwidth of the collection circuit.

3.8.2 Determination of laser induced temperature change

The finite element modeling of the thermal gradient evolution used for determining the temperature and thermal decay times was performed using the COMSOL Multiphysics Heat Transfer Module. We consider a single temperature diffusive model in which the laser is treated only as a heat source, rather than considering different the phonon and electrons temperatures.

This is justified by the fact that the optically excited electrons are thermalized on time scales comparable to the laser pulse width of 3 ps [92].

The spatiotemporal evolution of the thermal gradient in our system is calculated numerically with the Fourier diffusion equation using the material parameters given in Table 1. The heat source $Q(\vec{x},t)$, is given by,

$$Q(\vec{x},t) = \frac{Q_o}{2\,\pi\,\delta_x\,\delta_y\,d}\; e^{-\frac{x^2}{2\delta_x^2}-\frac{y^2}{2\delta_y^2}} e^{-\frac{z}{d}}\, e^{-\frac{t^2}{2\tau^2}} \tag{3.9}$$

where, δ_x and δ_y are the Gaussian widths in the x and y direction of the laser spot (440 nm), d is the skin depth (12nm), Q_o is the incident peak power of a single pulse (2.19 W), and τ is the pulse Gaussian temporal width of the 3 ps pulse.

Table 1 Material parameters used for simulation

Material	Thermal Conductivity (W/m K)	Specific Heat (J/g K)	Density (g/cm^3)
Sapphire [93]	30.3	0.764	3.98
Permalloy	46.4 [94]	0.43 [95]	8.7 [96]

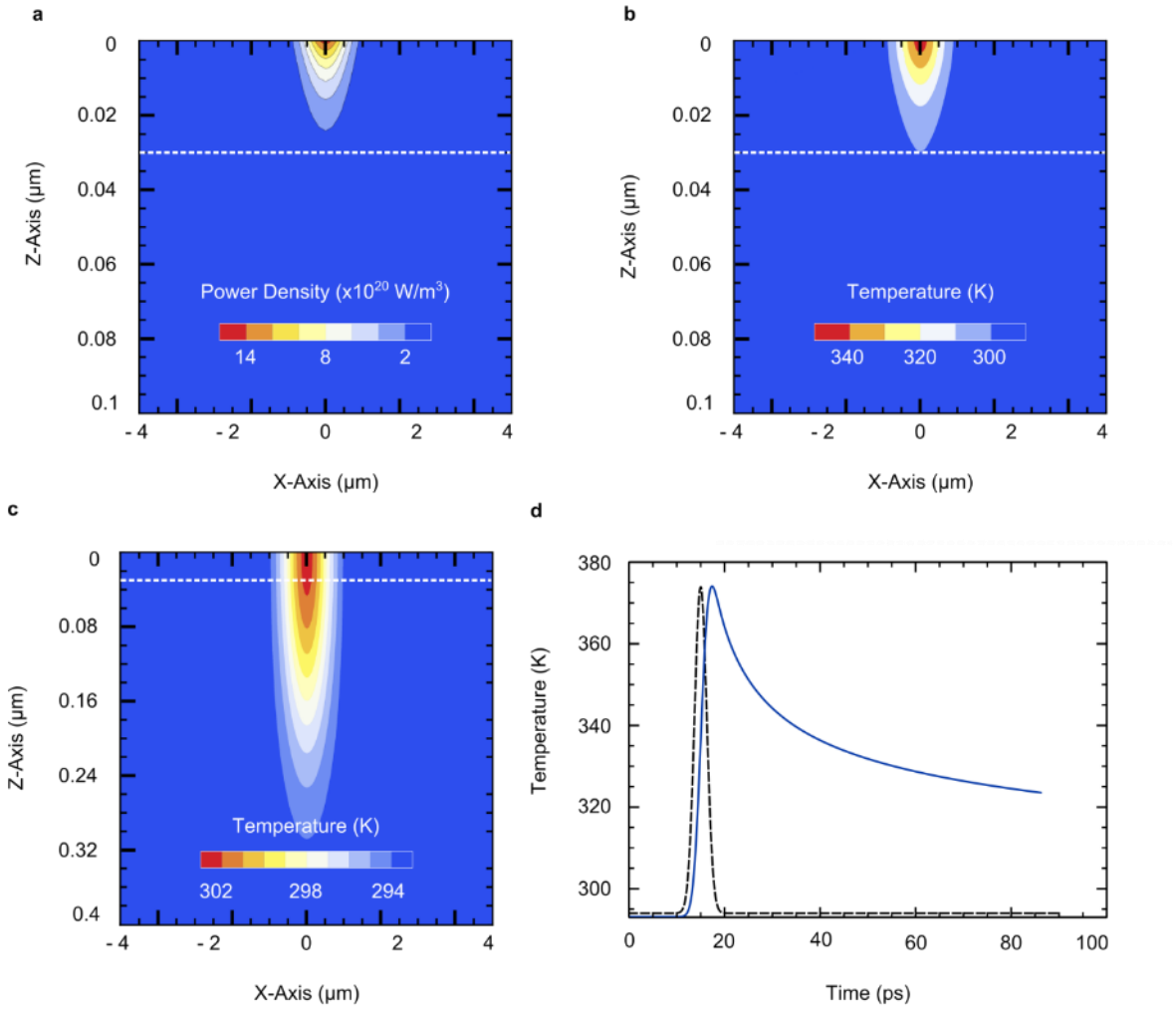

Figure 3.4 Simulated spatial and temporal temperature profiles. **a,** Spatial profile of the heat source, $Q(\vec{x},t)$, for the 440 nm spot size. **b-c,** Temperature profiles across an axial slice of the thermal source of the 440 nm Gaussian width. The dashed line indicates the interface between the permalloy wire and the sapphire. **b,** is the temperature at the peak of the pulse and **c**, is the temperature 982 ps after the peak. **d,** Time dependence of the laser induced temperature increase for 440 nm resolution thermal spot. The dashed line shows the temporal profile of the heat source in arbitrary y – axis for reference.

The results of the simulations yield spatiotemporal profiles of the temperature and thermal gradient shown in Figure 3.4. To apply the simulation for quantitative analysis we need a sample specific scaling factor determined experimentally (See sections 3.8.2-3.8.3).

3.8.3 Experimental measurement of resistance increase

When the laser induces a temperature increase to create the TRANE signal, it also creates an increase in the local resistance. If there is electrical current in the sample, the resistance change creates an additional voltage contribution that is independent of the sample magnetization. In this section, we use the signal from the local resistance change to measure the temperature profile of the sample due to heating from the laser. We determine the local resistance change by measuring the signal dependence on an applied DC electrical current. The DC current is applied to the sample by introducing a bias-tee into the circuit as shown in Figure 3.5. To show the relationship between the resistance change and the measured voltage, we begin with the sample voltage, which is given by

$$V_{sample}(t) = V_{ANE}(t) + I(t)\,R(t), \tag{3.10}$$

where V_{ANE} is the voltage from the anomlaous Nernst effect and $I(t)\,R(t)$ is the Ohmic voltage. For the current scenario, we set a constant applied current, while the resistance and V_{ANE} vary in time. From section 3.8.1, we find the voltage at the mixer output is given by

$$V_m = \frac{1}{V_0}\sum_{k=-K}^{K} c_{-k}^{r}\left[c_n^{ANE} + \int_{-\frac{T}{2}}^{\frac{T}{2}} dt\; I_{DC} R(t) e^{-\frac{i2\pi kt}{T}}\right]. \tag{3.11}$$

By chopping laser power, the lock-in voltage from the mixer signal is given by

$$V_{LI} = \frac{1}{V_0}\sum_{k=-K}^{K} c_{-k}^{r}\left[c_n^{ANE} + I_{DC}\; c_k^{\Delta R}\right], \tag{3.12}$$

where $c_n^{\Delta R} = \int_0^T dt\, \Delta R(t) e^{-i\,(2\pi k)t/T}$ is Fourier series component of the change in the resistance, ΔR, from room temperature. We show the results of these measurements in Figure 3.5b, which displays the expected linear relationship between the collection signal and the applied DC current. We repeat the measurements at various laser powers and plot the slope as a function of laser power in Figure 3.5c. These measurements were performed in the presence of a large saturating magnetic field, so that we can neglect current induced magnetization effects that may change the anomalous Nernst signal. Therefore, by relating the resistance change to a temperature increase, we can quantitatively determine the heating induced by the laser.

It is non-trivial to directly convert this data into a measure of resistance due to the non-linearity of the circuit components. Instead, we compare this data to numerical simulations and calculations. We numerically simulate the temperature profile to calculate its corresponding resistance change and the resulting collection signal. Due to the unknown absorption coefficient of the sample, there is an uncertainty in the absolute value of the temperature change. Therefore, there will be an overall factor which is determined by comparing the simulation results with the measured collection signal. By comparing the slopes of the calculated and measured signals as a function of DC current, we obtain the total temperature change and the temperature gradient.

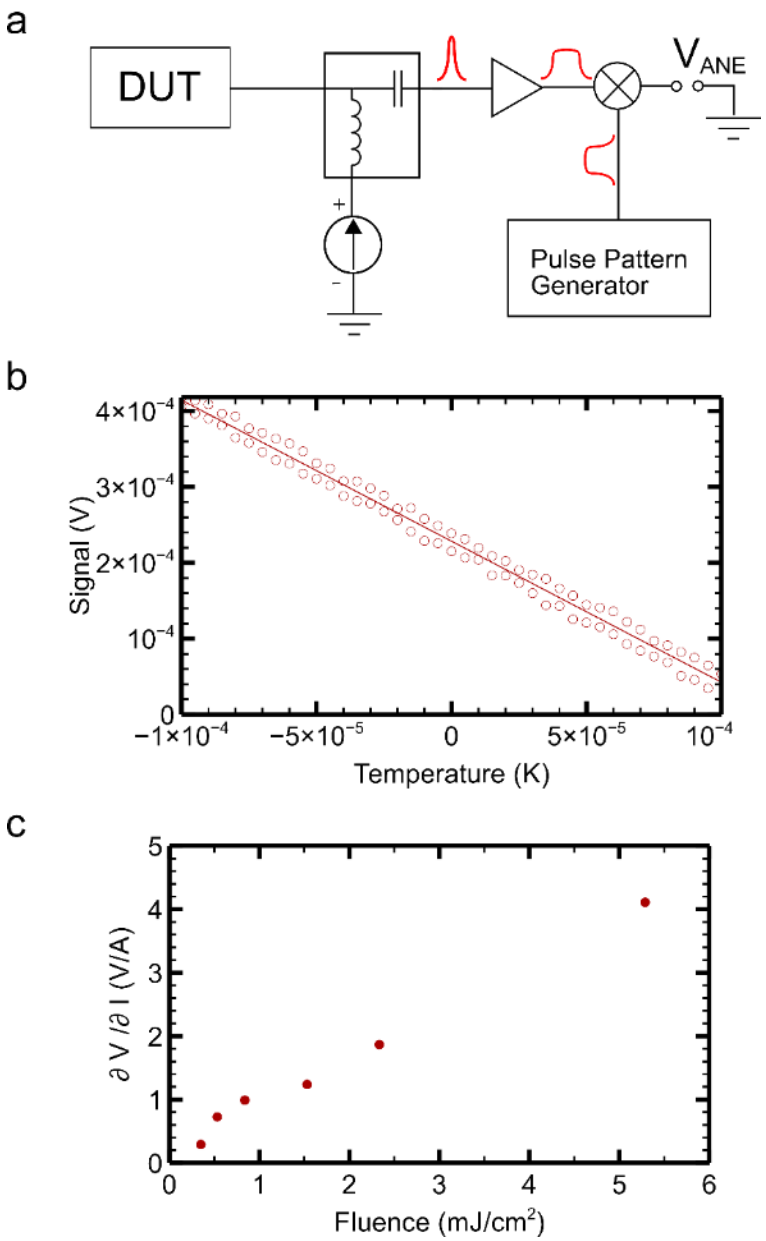

Figure 3.5 Measurement of temperature dependent resistance. **a**, Circuit setup to measure the temperature induced resistance change. **b,** The collection signal as a function of the applied DC current to measure the resistance change due to heating from the laser pulse. **c**, The slope of the collection signal versus applied DC current for various laser powers.

3.8.4 Temperature dependence of resistivity

We measure the temperature dependence of resistivity to map the simulated temperature profile to a total resistance change. We consider the linear response regime of the resistivity dependence on temperature, such that

$$\rho(T) = \rho_0[1 + \alpha(T - T_0)] = \rho_0[1 + \alpha\Delta T], \tag{3.13}$$

where ρ_0 is the resistivity at the base temperature T_0, which we set as room temperature at 293 K, and α is the temperature coefficient of resistivity. To determine the temperature coefficient of resistivity, we measure the 4-point resistance as a function of temperature with a physical property measurement system (PPMS), with the results shown in Figure 3.6. With the 4-point resistance measurement, we remove contributions due to contact resistance, therefore the resistivity is related to the resistance by $\rho = \frac{RA}{L}$, where A is the cross-sectional area and L is the length between the measurement probes. By fitting the data in Figure 3.6, we find the temperature coefficient of resistance in the 30 nm permalloy to be α = 0.0025 Ω/*K*.

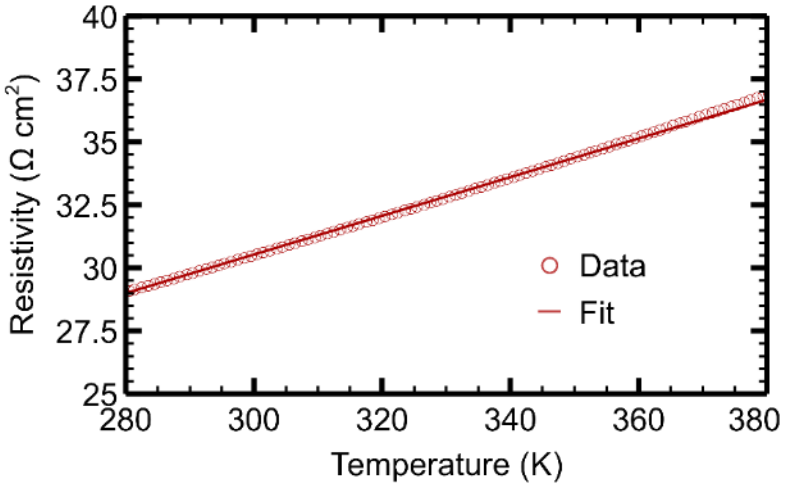

Figure 3.6 Temperature dependent resistivity with the PPMS, we measure the temperature dependence of the resistance of a 30 nm thick permalloy sample.

We calculate the total time-varying resistance induced from laser heating by mapping the numerically simulated temperature profile to a resistivity profile using the measured resistivity versus temperature. The total resistance of the sample in terms of the spatially dependent resistivity is given by

$$R(t) = \left[\int dy\, dz \left[\int dx\, \rho\big(T(\vec{x},t)\big)\right]^{-1}\right]^{-1}, \tag{3.14}$$

where $\rho\big(T(\vec{x},t)\big)$ is the temperature dependent resistivity. Applying the linear temperature dependence of the resistivity gives

$$R(t) = \left[\int dy\, dz \left[\int dx\, \rho_0(1 + \alpha\Delta T(\vec{x},t))\right]^{-1}\right]^{-1}. \tag{3.15}$$

From the measurements of the resistivity temperature dependence, it is safe to assume $\alpha\Delta T \ll 1$. Therefore, we find the total resistance change by performing a series expansion and taking the first order term to be

$$\Delta R(t) = R_0 \int^{V} \frac{d\vec{x}}{V}\, \alpha\Delta T(\vec{x},t). \tag{3.16}$$

This shows that the total resistance change is proportional to the mean temperature change through the length of the wire. Figure 3.7 shows the calculated total resistance change as a function of time for the simulated temporal profile from Figure 3.4b.

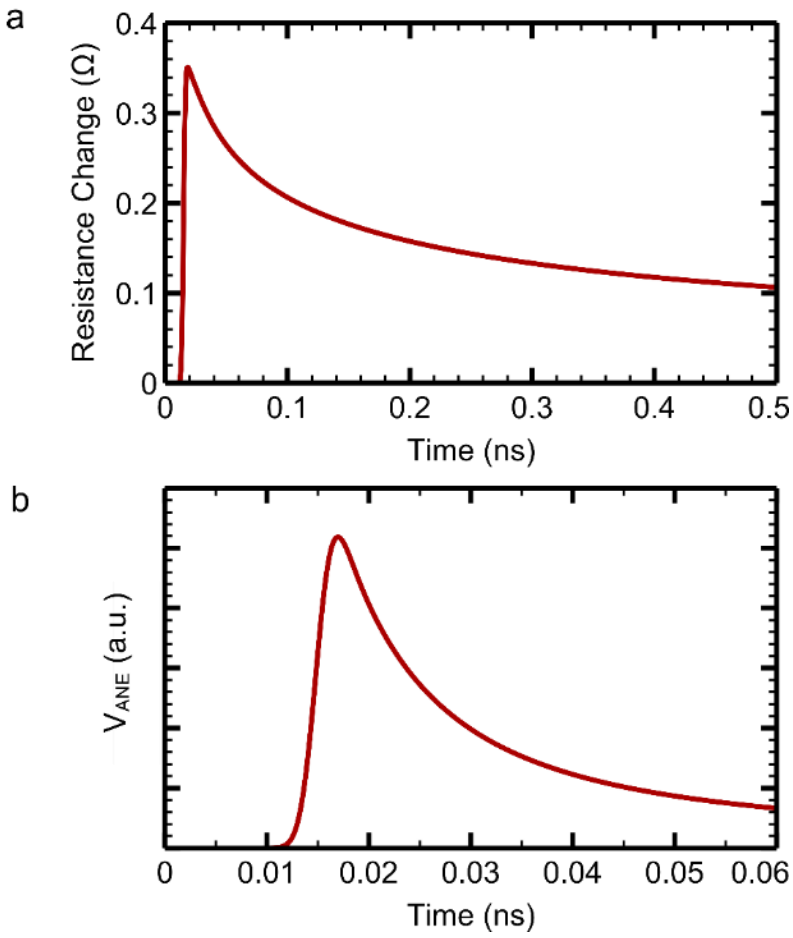

Figure 3.7 Calculated laser induced resistance change and V_{ANE} signal. a, The total resistance change calculated from the numerically simulated temperature change from heating due to the laser. b, The temporal response of the anomalous Nernst voltage. These calculations correspond to a Gaussian laser pulse with its peak at 15 ps.

We note from Figure 3.7 that the decay lifetime for resistance change is much larger than the pulsed anomalous Nernst voltage. This is because the anomalous Nernst voltage is dependent on the vertical component of the temperature gradient while the resistance change is dependent on the overall mean temperature. Therefore, lateral thermal diffusion from the heat source into other regions of the ferromagnet will reduce the vertical thermal gradient, causing the decay in the anomalous Nernst voltage. Conversely, lateral thermal diffusion has less influence on the overall mean temperature, and thus the total resistance changes more slowly.

We determine the temperature profile by scaling the simulated temperature profile in Figure 3.4 to match the measured signal slope in Figure 3.6. This matching is done by taking into account the bandwidth and the collection circuit transfer coefficient as described in section 3.8.9. For the typical laser fluence used of 2.3 mJ/cm^2, we determine a dimensionless scaling factor of 0.4. Physically, this scaling factor accounts for the unknown optical absorption coefficient. Using this factor we calculate a resulting maximum temperature increase of 30 K and a corresponding maximum gradient of 3.3×10^8 K/m. This is ~100 times greater that the value of ~1×10^6 K/m quoted in reference 21 of the main text for a CW laser [43]. This highlights the distinction between pulsed and CW laser measurements. We show the maximum temperature increase for various laser fluences in Figure 3.8. The linearity of temperature increase as a function of laser fluence suggests that the heating from the laser is in the linear response regime.

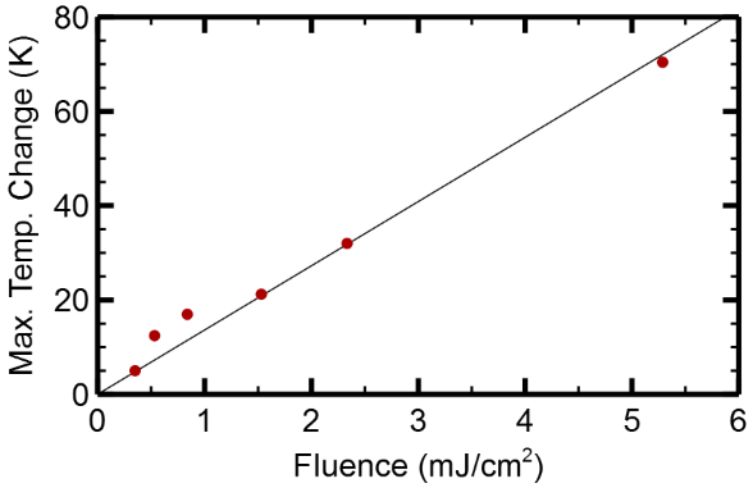

Figure 3.8 Laser induced temperature change. The measured maximum temperature change due to heating from the laser as a function of the laser fluence.

By comparing the measured hard-axis TRANE hysteresis with the resistor model, we measure an anomalous Nernst coefficient of $3.7 \pm 0.4 \times 10^{-6}$ V/K T. This value has the same

order of magnitude as reported in the literature [39,83]. There is no consensus value because the anomalous Hall coefficient for permalloy, which is related to the anomalous Nernst effect through the Seebeck coefficient, is highly dependent on the thickness and resistivity [91]. This suggests that TRANE is a viable technique to measure the anomalous Nernst coefficient in materials without specialized thermal measurement apparatus. The error bars for this measurement include errors from the experimental error in the transfer coefficient and the timing of the mixing pulse. It has ignored the uncertainty of values used in the numerical simulation, which include the laser pulse temporal profile and the material parameters. These errors would change the overall scaling factor used to predict the temperature and anomalous Nernst coefficients, but it does not influence the technique to measure possible variations within the sample.

3.8.5 Temporal convolution using an electrical mixer

For TRANE microscopy to be a truly stroboscopic, time-domain method, the voltage induced by the thermal gradient has to decay faster than the probed dynamical behavior because the thermal gradient lifetime defines the interaction time between the magnetization and the probe. Direct measurement of the V_{ANE} voltage pulse using an oscilloscope is difficult due to the short temporal duration (ps scale) and the small voltage amplitude (nV scale). As an alternative, we measure the convolution between the V_{ANE} pulse and a reference electrical pulse of known width. In this scheme, we amplify the pulse with two 10 kHz-15 GHz, 15 dB amplifiers (Picosecond Pulse Labs model 5867) and use a high-speed (.5-18 GHz) electrical mixer (Remec model MM94PG-40) to multiply the pulse, V_{ANE}, with an electrical mixing pulse, V_{pulse}. When the relative delay between the pulses, τ, is systematically varied, we measure the temporal

convolution of the two pulses, $\int_0^T V_{ANE}(t)V_{pulse}(\tau - t)dt$, where T is the laser pulse repetition period. The width of resulting mixed-down signal as a function of τ is most strongly determined but the width of the longest pulse entering the mixer. This measurement is depicted schematically in Figure 3.9.

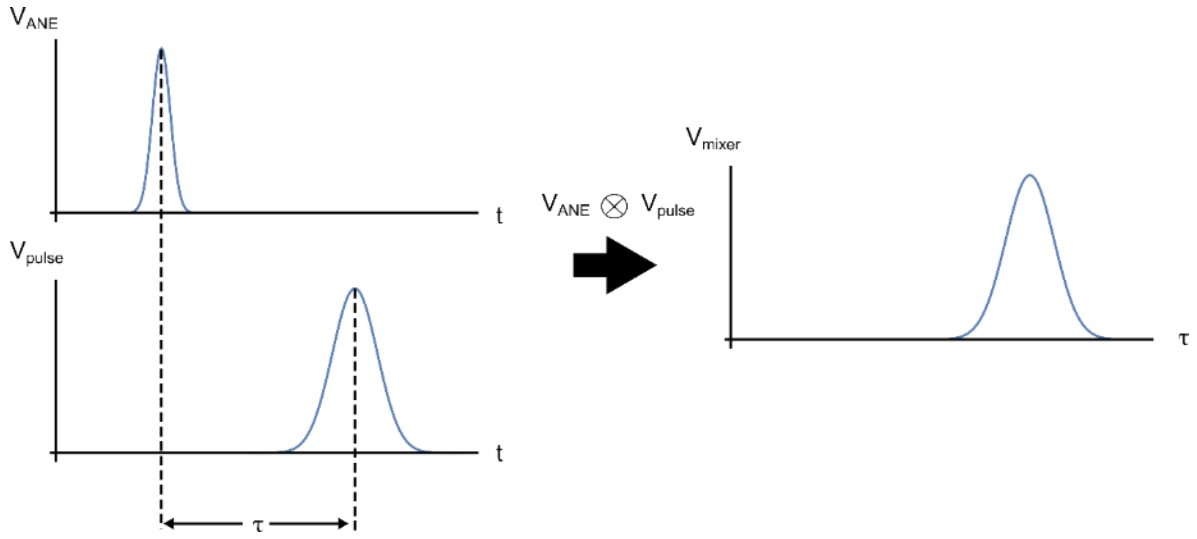

Figure 3.9 Schematic Depiction of Temporal Convolution Using an Electrical Mixer. A depiction of the idealized temporal convolution measurement using a .5-18 GHz mixer. For two pulses of different widths, the resulting measurement has a pulse full-width-at-half-maximum that is equal to the width of the longest pulse.

We note that when used for TRANE measurements, the delay τ is fixed and the pulse V_{ANE} is multiplied by a pulse from a pulse pattern generator (pulse width ~1.5 ns) after amplification by two 0.1-1 GHz bandwidth 20 dB gain amplifiers (Mini-Circuits model ZFL-1000LN+). This form of homodyne detection is used to convert the short-lived TRANE pulse into a low-frequency signal that can be measured by the lock-in. Lower frequency detection circuitry does not reduce the temporal resolution (see section 3.8.1) and allows us to filter gigahertz frequency noise induced in the magnetic channel by the AC driving field. Additionally,

using a wider V_{pulse} decreases the measurement's sensitivity to variations in the delay between the V_{ANE} and V_{pulse}.

3.8.6 Sensitivity

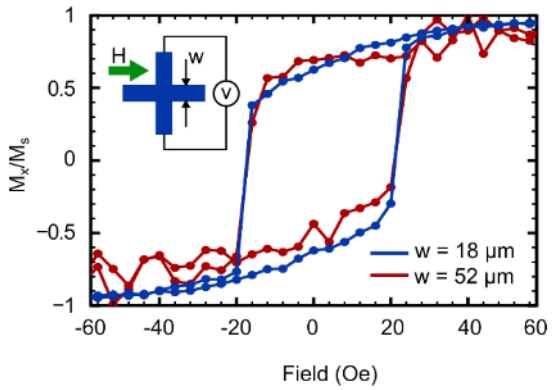

Figure 3.10 Comparison of hysteresis measurement sensitivity**.** In this graph we plot TRANE – measured hysteresis loops for two different cross sizes. We observe that the sensitivity is $\theta_{min} = 4.6^o/\sqrt{Hz}$ for the 52 μm cross and $\theta_{min} = 0.73^o/\sqrt{Hz}$ for the 18 μm wide cross.

The sensitivity is calculated using the field-dependent magnetization measurements shown in Figure 3.1c and Figure 3.10. This measurement is done in the transverse geometry – the saturated moment is perpendicular to the voltage pick-ups – so that $(V_{TRANE}^{max} - V_{TRANE}^{min})$ corresponds to a 180° rotation. The standard deviation of points at saturation is taken as the detected voltage uncertainty, δ_{TRANE}. As a longer sampling time will reduce the value of δ_{TRANE} regardless of the sample, it is desirable to have a sensitivity figure of merit independent of the sampling time. Thus, the signal-to-noise ratio must be scaled to account for the measurement rate, in the case of a lock-in measurement this is the time constant. This yields an equation for the minimum detectable angle, θ_{min}, with respect to the angle of highest sensitivity, $\theta_o = 90^o$, measurable with the TRANE technique.

$$\theta_{min} = \frac{\delta_{TRANE}}{Sin(\theta_o)\left(V_{TRANE}^{max} - V_{TRANE}^{min}\right)/2}\sqrt{TC} \tag{3.17}$$

3.8.7 Fitting lateral resolution

We measure the value for the lateral resolution by taking vertical line cuts of the 2D scan across a portion of the domain wall (Figure 3.2a and Figure 3.11a). The 4 μm region of the domain wall used for fitting is shown boxed in Figure 3.11a. This region was chosen because it was the portion of the image with the clearest step function behavior. Fits of the line scans where done using a least means squared method to find the Gaussian width, amplitude, and center of a function derived by convolution of a Gaussian with a –1 to 1 step function. The results of the individual fits are shown in Figure 3.11b. The mean of the fits is 460 nm with a standard deviation of 90 nm, the standard deviation is used as the uncertainty as it was larger than the uncertainty of the individual fits.

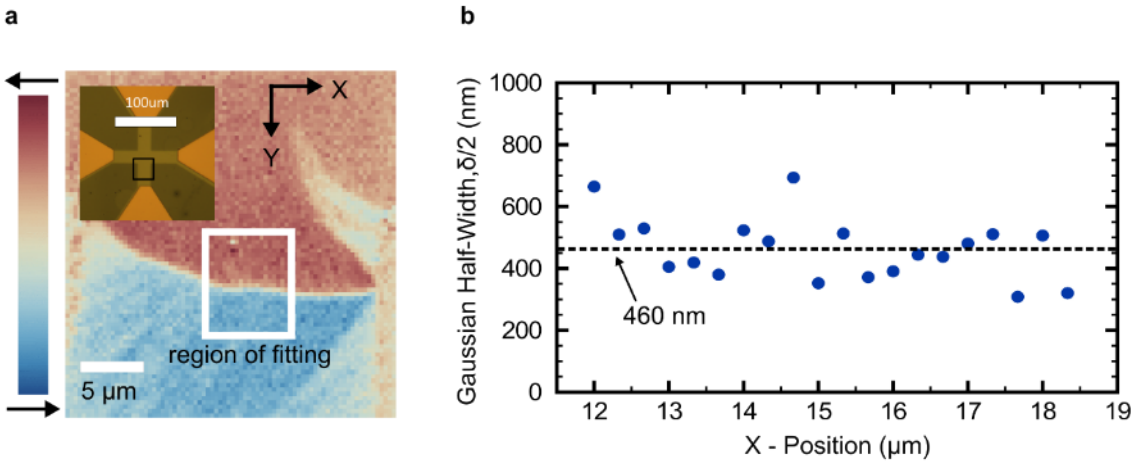

Figure 3.11 Region and results of spatial fitting. a, Spatial map of the static magnetic moment showing the region used for the lateral resolution measurement. b, One-half the Gaussian-width of the pulse that was convolved with the unit step determined by fitting. The x-axis is the horizontal coordinate of the line cut used and the dashed line indicates the mean.

3.8.8 Modification of the resonant line-shapes due to field modulation

To measure the FMR of the permalloy wires we detect the projected magnetic moment perpendicular to the wire. The magnetic moment of the wire precesses about the externally applied magnetic field when driven by a microwave field generated in a microwave antenna patterned parallel to the magnetic wire. The FMR precession angle of a ferromagnet in the linear response regime can be modeled as a driven damped oscillator. The projection amplitude of this motion is the linear combination of even and odd Lorentzian functions.

$$Sin(\varphi)\frac{(H-H_r)/\vartheta}{1+(H-H_r)^2/\vartheta^2} + Cos(\varphi)\frac{1}{1+(H-H_r)^2/\vartheta^2} \qquad (3.18)$$

When measuring magnetic dynamics with TRANE, a time-varying magnetic field is applied across the ferromagnet. This induces an electrical current in the ferromagnetic wire, which creates a large background voltage across the wire which is removed with a lowpass filter.

In addition to the magnetic signal due to FMR, we also detect an induced electrical response from coupling between the microwave antenna and the magnetic channel that is detected because of the temperature induced resistance change. However, since the resistance change contribution is independent of magnetization, we are able to remove it by using a cascaded lock-in technique. We detect the signal by using two lock in amplifiers connected in series, the first demodulation was referenced to a square modulated 9.7 kHz signal from an optical chopper and the second demodulation was referenced to a 14 Oe sinusoidal field modulated at 10 Hz (5 Hz for FMR frequencies above 10 GHz). The TRANE signal detected by the second lock-in can be modeled by

$$Sin(\varphi)\int \frac{\frac{H + H_{mod}Cos(\omega\, t) - H_r}{\vartheta}}{1 + \frac{(H + H_{mod}Cos(\omega\, t) - H_r)^2}{\vartheta^2}} * Cos(\omega\, t)dt + Cos(\varphi)\int \frac{1}{1 + \frac{(H + H_{mod}Cos(\omega\, t) - H_r)^2}{\vartheta^2}} * Cos(\omega\, t)\, dt. \tag{3.19}$$

The resulting analytical equation is then used to fit the resonance data obtained with TRANE to quantify the values of the linewidth, amplitude, phase, and center frequency. We note that the modification to the Lorentzian shape does not add free parameters to the fitting function because the modulation amplitude is a known value. The modulation does impact the uncertainty and it reduces the overall signal amplitude, but at the benefit of increased angular sensitivity.

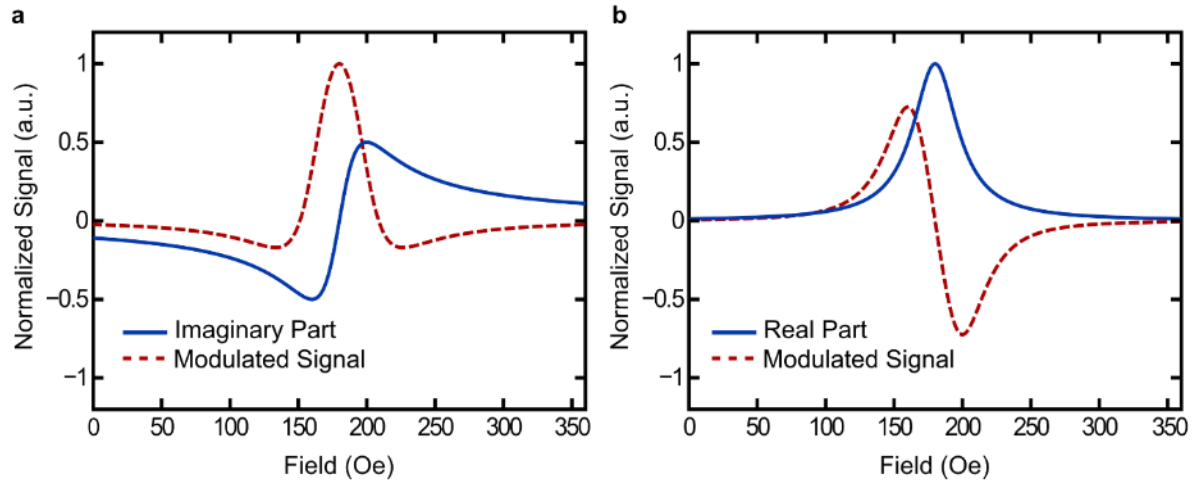

Figure 3.12 Modification of lorentzian functions. The blue curve in each plot shows the modeled, normalized Lorentzian response function for the projected amplitude of the FMR precession for a resonant field, H_r = 180 Oe and line-width of 80 Oe. The dashed, red curves show the corresponding signal line shape as detected by the lock-in when using a modulation amplitude of 20 Oe.

3.8.9 Collection circuit transfer coefficient

To determine the transfer coefficient of the collection circuit depicted in Figure 3.1b and Figure 3.1a, we measure the collection voltage from a calibration pulse. Numerical simulations indicate that ∇T_Z has a width of 10 ps which for our magnetic system translates into a V_{ANE} pulse that also has a width of 10 ps. With the electronics available, we cannot create a 10 ps pulse to directly measure the transfer coefficient. Instead, we extrapolate it through measuring the gain of square pulses of wider widths. Figure 3.13 shows the total gain in the collection circuit as a function of the square pulse width and the fit with our model.

We use equation Eq. (3.5) to model the gain where V_0 is the free parameter to fit the model. The pulse pattern generator signal into the mixer is treated as a periodic triangular function such that

$$V_{PPG}(t) = \sum_n V_{PPG}^0 \, Tri\left(\frac{t + nT}{\delta}\right), \tag{3.20}$$

where V_{PPG}^0 is the peak voltage, δ is the rise and fall time, $f_0 = 1/T$ is the laser repetition rate and Tri is a triangular function given by

$$Tri(x) = \begin{cases} 1 - |x|, & if\ |x| < 1 \\ 0, & else \end{cases}. \tag{3.21}$$

For all measurements, we set the pulse pattern generator to have a peak voltage of 800 mV and a rise and fall time of 800 ps. We can express this in terms of a Fourier series as

$$V_{PPG}(t) = \sum_k V_{PPG}^0(\delta f_0)\, sinc^2(\pi f_0 k\delta) e^{i2\pi f_0 kt}. \tag{3.22}$$

Similarly, we can express the calibrating square pulse train generated by the AWG as

$$V_{sq}(t) = \sum_n V_{sq}^0 \, Sq\left(\frac{t + nT}{\tau}\right), \tag{3.23}$$

where V_{sq}^0 is the peak voltage, τ is the square wave width and Sq is a square pulse function given by

$$Tri(x) = \begin{cases} 1, & if\ |x| < 1/2 \\ 0, & if\ |x| > 1/2 \end{cases}. \tag{3.24}$$

The square pulse train can be expressed in terms of the Fourier series as

$$V_{sq}(t) = \sum_k V_{sq}^0(f_0\tau)\ sinc(\pi f_0 k\tau) e_0^{i2\pi f_0 kt}. \tag{3.25}$$

The square pulse voltage is measured with a sampling oscilloscope to be 2.22 mV and the pulse width is varied from 300 ps to 3 ns.

With the two input signals, the DC component of the mixer output voltage is

$$V_m^{DC} = \frac{V_{sq}^0 V_{PPG}^0}{V_0}(f_0^2\tau\delta) \sum_{k=-K_{max}}^{K_{max}} sinc(\pi f_0 k\tau) sinc^2(\pi f_0 k\delta). \tag{3.26}$$

The bandwidth of the amplifiers and mixer set the maximum frequency of the sum to $K = f_0/f_{max}$ where f_{max} is the maximum frequency bandwidth. For the measurements, the collection circuit bandwidth is limited to a maximum of f_{max} = 1 GHz and the laser repetition rate is f_0 = 25.3 MHz. By fitting equation Eq. (3.26) to the calibration measurement with V_0 as the only free parameter, we obtain a best fit of V_0 = 0.41 ± 0.04 mV.

It is desirable to describe the total measured voltage in terms of the peak anomlaous Nernst voltage in terms of a collection circuit transfer coefficient. We define the transfer coefficient γ as

$$V_m^{DC} = \gamma\ Max[V_{ANE}(t)]. \tag{3.27}$$

We can determine γ by using the numerically simulated anomalous Nernst voltage in section 3.8.3 and applying it to calibration fit. Using the voltage multiplier coefficient from the fit in Figure 3.13, our model estimates a transfer coefficient of 0.47 ± 0.04 for the numerically

simulated pulse of approximately 10 ps in width. This is the value for the circuit shown as an inset in Figure 3.13. We note that the transfer coefficient will change for different collection circuit components and mixing pulse durations.

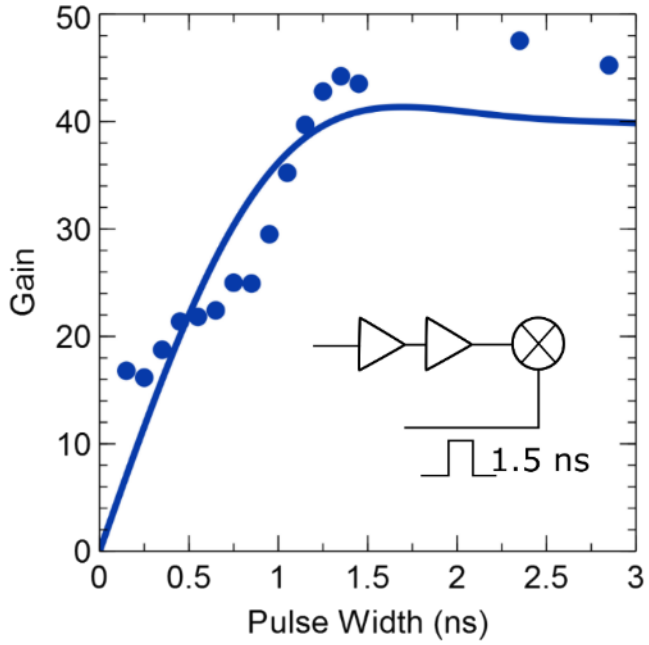

Figure 3.13 Collection circuit gain. We plot the dependence of the collection circuit gain on the temporal width of a calibrating square pulse. The model used to fit the data estimates a transfer coefficient of 0.47 ± 0.04 for a 10 ps TRANE pulse. The amps are two Mini-Circuits ZFL-1000LN+ in series the mixer is a Mini-circuits ZAD-1-1+.

3.8.10 Funding acknowledgements

This work was supported by AFOSR. The authors would like to thank Isaiah Gray for his help measuring the temperature dependence of permalloy resistivity. This work made use of the Cornell Center for Materials Research Shared Facilities which are supported through the NSF MRSEC program (DMR-1120296) as well as the Cornell NanoScale Facility, a member of the National Nanotechnology Infrastructure Network, supported by the NSF (Grant ECCS-0335765).

CHAPTER 4

IMAGING MAGNETIZATION STRUCTURE AND DYNAMICS IN ULTRATHIN $Y_3Fe_5O_{12}$/Pt BILAYERS WITH HIGH SENSITIVITY USING THE TIME-RESOLVED LONGITUDINAL SPIN SEEBECK EFFECT [97]

4.1 Chapter abstract

We demonstrate an instrument for time-resolved magnetic imaging that is highly sensitive to the in-plane magnetization state and dynamics of thin-film bilayers of yttrium iron garnet ($Y_3Fe_5O_{12,}$YIG)/Pt: the time-resolved longitudinal spin Seebeck (TRLSSE) effect microscope. We detect the local, in-plane magnetic orientation within the YIG by focusing a picosecond laser to generate thermally-driven spin current from the YIG into the Pt by the spin Seebeck effect, and then use the inverse spin Hall effect in the Pt to transduce this spin current to an output voltage. To establish the time resolution of TRLSSE, we show that pulsed optical heating of patterned YIG (20 nm)/Pt(6 nm)/Ru (2 nm) wires generates a magnetization-dependent voltage pulse of less than 100 ps. We demonstrate TRLSSE microscopy to image both static magnetic structure and gigahertz-frequency magnetic resonance dynamics with sub-micron spatial resolution and a sensitivity to magnetic orientation below 0.3 deg/$\sqrt{Hz}$ in ultrathin YIG.

4.2 Introduction

Ultrathin bilayers of the magnetic insulator YIG interfaced with a heavy, non-magnetic metal (NM) such at Pt are being intensely studied for the development of high-efficiency magnetic memory and logic devices operated by spin-orbit torque [98,99], for magnon generation and propagation [100–102], and as a model system for understanding spin-current generation by the longitudinal spin Seebeck effect (LSSE) and spin pumping [33,103–105]. For all of these research areas, it would be useful to have a high-sensitivity and local probe of

magnetization dynamics in the YIG layer, especially for the ultrathin films required in many devices. This has proven challenging, and although magneto-optical techniques such as Brillouin light scattering and the magneto-optical Kerr effect (MOKE) have proven valuable [57,100,106–109], they have not enabled direct time-resolved imaging of magnetic precession or direct imaging of in-plane magnetization of ultra-thin YIG films (20 nm and below). An alternative approach that enables in-plane imaging of YIG/Pt bilayer devices was demonstrated by Weiler *et al*. [43]. In that work, the authors use laser heating to image the in-plane magnetic structure of YIG, but not its dynamics. Here we extend the approach into the time domain to perform high sensitivity imaging of the in-plane magnetic orientation ($< 0.3°/\sqrt{Hz}$) with sub-micron spatial resolution and sub-100 ps temporal resolution. Using TRLSSE microscopy we can observe, for example, that the resonance field in ultra-thin YIG films can vary by up to 30 Oe within micron-scale regions of a YIG/Pt device. Our results demonstrate that TRLSSE microscopy is a powerful tool to characterize static and dynamic magnetic properties in ultrathin YIG.

The principle behind the TRLSSE microscope, shown schematically in Figure 4.1, is the generation and detection of a thermally generated local spin current [68]. For the case of YIG/Pt, a local thermal gradient perpendicular to the film plane is generated by laser heating of Pt. The gradient creates a thermally-induced spin current that is proportional to the local magnetization [54,55,58]. The spin current that flows into the Pt is detected with the ISHE [49,110] in which spin-orbit coupling leads to a spin-dependent transverse electric field. For this work, the resulting voltage can be described as [54,58]

$V_{LSSE} \propto -\xi_{SH} S \frac{\mathbf{M}(\boldsymbol{x},t)}{M_s} \times \boldsymbol{\nabla}\mathbf{T}(\boldsymbol{x},t)$, where, ξ_{SH} is the spin Hall efficiency, S is the spin-Seebeck coefficient, $\mathbf{M}$ is the local magnetization, M_s is the saturation magnetization and $\boldsymbol{\nabla}\mathbf{T}$ is the

thermal gradient. The LSSE has been attributed to both thermal gradients across the thickness of YIG and to interfacial temperature differences between YIG and Pt [54,55,58,111,112]. Our experiment cannot definitively distinguish between these two mechanisms. Thus, here we discuss only $\boldsymbol{\nabla T}$ as single quantity for simplicity and for consistency with our prior work using the anomalous Nernst effect, however, this question requires further study. V_{LSSE} is a read-out of the local magnetization m_y because the electric field is generated in response to the spatially local z-component of the thermal gradient, ∇T_z (coordinates as defined in Figure 4.1) [43,83].

To extend LSSE imaging into the time-domain, we use picosecond laser heating to stroboscopically sample magnetization. We have previously shown [63], in metallic ferromagnets, that picosecond heating can be used for stroboscopic magnetic microscopy using the time-resolved anomalous Nernst effect (TRANE). In TRANE microscopy, the temporal resolution is set by the excitation and decay of a thermal gradient within a single material that both absorbs the heat from the laser pulse and produces a TRANE voltage from internal spin-orbit interactions [113,114]. In the LSSE however, the timescale of spin current generation can depend on both the timescale of the thermal gradient and the timescale of energy transfer between the phonons and magnons. Recent experiments indicate that in the qausi-static regime the magnon-phonon relaxation rate may play a dominant role [59–61,115]. Using picosecond heating and time-resolved electrical detection to move beyond the quasi-static regime, we show a TRLSSE in agreement with a recent all-optical experiment [111].

The samples were grown by the Yang group at The Ohio State University using off-axis sputtering onto (110)-oriented gadollinum gallium garnet ($Gd_3Ga_5O_{12}$, GGG), [116–118] followed by *ex situ.* deposition of 6 nm of Pt with a 2 nm Ru capping layer. Photolithography and ion milling were used to pattern wires and contacts for wirebonding. We present

measurements of a 2 μm × 10 μm wire and a 4 μm × 10 μm wire with DC resistances of 296 Ω and 111 Ω respectively. In this room temperature study, we neglect the potential anomalous Nernst effect of interfacial Pt with induced magnetization [119,120], and we neglect a possible photo-spin voltaic effect [121], neither of which can be distinguished from TRLSSE in presented measurements.

4.3 Experimental methods

Our TRLSSE measurement consists of pulsed laser heating and homodyne electrical detection as shown in Figure 4.2a. We use a Ti:Sapphire laser pulse to locally heat the sample with 3 ps pulses of 780 nm light at a repetition rate of 25.5 MHz. The electrical signal produced at the sample is the sum of the LSSE dependent voltage, $V_{LSSE}(\nabla T_z, \mathbf{M})$, and a voltage, $V_J(\Delta T, J)$, which is generated when a current density J is passing through the local region of Pt with increased resistance due to laser heating [122]. To reject noise and recover the signal of the resulting electrical pulses, we use a time-domain homodyne technique in which we mix the V_{LSSE} + V_J pulse train with a synchronized reference pulse train, V_{mix}, in a broadband (0.1-12 GHz) electrical mixer. The mixer output is the convolution of the two pulse trains given by [122]

$$V_{sig}(\boldsymbol{x}, \tau) = K \int_0^{\Gamma} (V_{LSSE}(\nabla T_z(\boldsymbol{x}, t), \mathbf{M}(\boldsymbol{x}, t)) + V_J(\Delta T(\boldsymbol{x}, t), J(\boldsymbol{x}, t))\, V_{mix}(\tau - t) dt, \qquad (1)$$

where $\boldsymbol{x}(x,y)$ is the laser spot position in the sample plane, Γ is the period of the laser pulses, K is the transfer coefficient, and τ is the relative delay. A relative delay of zero corresponds to the maximum of both pulse trains arriving at the mixer simultaneously.

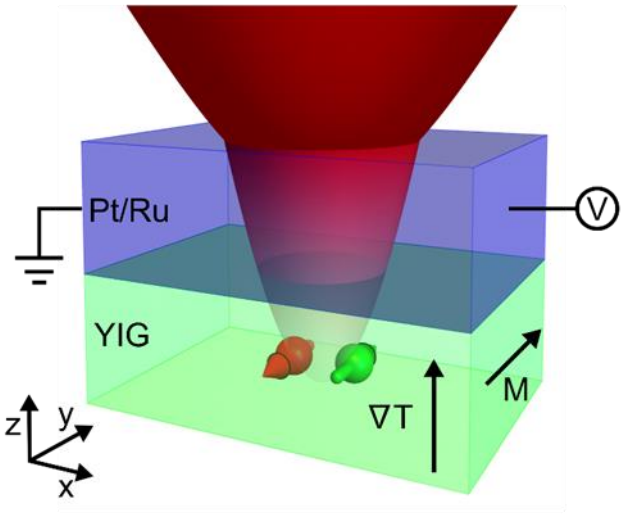

Figure 4.1 Schematic of our TRLSSE measurement. A 780 nm, 3 ps pulsed laser, focused to a 0.606 μm diameter spot, is used to heat a YIG (20 nm)/Pt(6 nm)/Ru(2 nm) film. The heating from the laser creates a temperature gradient, ∇T_z. The pulsed heating drives a pulsed magnon flux, Js, from the YIG into the Pt where it is transduced into a pulsed voltage via the ISHE.

We study the timescale of the LSSE signal generated by a picosecond pulse by measuring V_{sig} as a function of mixer delay τ. Figure 4.2b shows the result of this measurement using a 100 ps mixing pulse reference, V_{mix}, at a saturating magnetic field, H, perpendicular to the wire at H = +414 Oe and – 414 Oe, respectively. In Figure 4.2c we plot the difference between these two voltage traces to reject non-magnetic contributions. We find that the full-width at half-maximum (FWHM) is 100 ± 10 ps, which is followed by electrical oscillations that we attribute to non-idealities in the detection circuit (see section 4.5 for further discussion.) Because the duration of the magnetic component of V_{sig} is experimentally indistinguishable from the FWHM of V_{mix}, we conclude that 100 ps is an experimental upper bound for the TRLSSE signal duration.

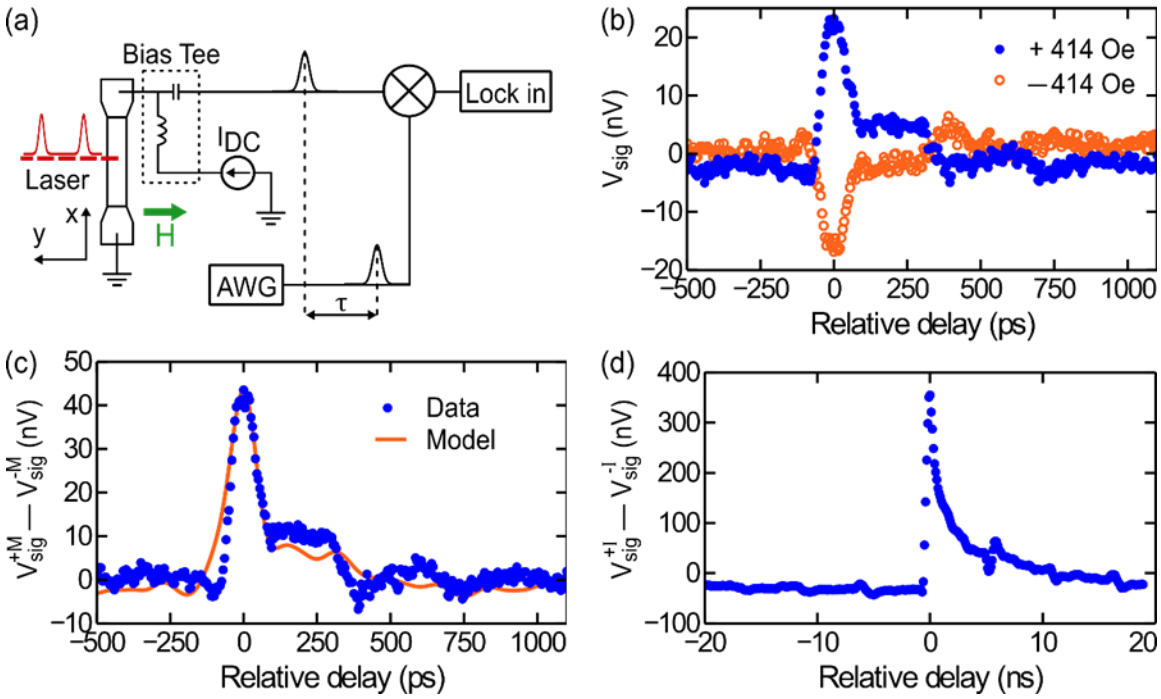

Figure 4.2 Time resolved longitudinal spin Seebeck effect. (a) Schematic of the LSSE detection circuit used for time-resolved voltage measurements. (b) Time-domain measurement of the LSSE generated voltage in the 2 μm wide wire. The time-varying LSSE signal is measured by electrically mixing the pulsed laser generated voltage with a 100 ps voltage pulse from the AWG. Comparing measurements of the YIG at +414 Oe (filled blue circles) and –414 Oe (open orange circles) shows that the signal depends on the orientation of the magnetic moment. Here d.c. level noise and has been removed. The data was acquired with a lock-in time constant of 500 ms and integration time of 2 s per point. (c) The solid blue circles show the difference between the two curves in (b), The orange line is a model, normalized by the data amplitude, of the signal determined by numerically convolving the calculated thermal gradient with the measured mixing pulse. (d) Difference signal of the temperature dependent voltage V_J measured using +/– 0.5 mA and a 600 ps mixing pulse. In (b-d) we report the voltage as detected at the lock-in after passing through the r.f. mixer, not the LSSE signal at the sample itself.

4.4 TRLSSE results

To calibrate the local change in the Pt temperature, ΔT_{Pt}, due to picosecond heating and to quantify the rate of thermal relaxation, we measure V_J in the presence of a DC current, which uses the local Pt resistivity as an ultra-fast thermometer. Figure 4.2d shows V_J as a function of mixer delay, $V_J(\tau) = V_{sig}(\tau, J = 4.2\ \mathrm{MA/cm^2}) - V_{sig}(\tau, J = -4.2\ \mathrm{MA/cm^2})$, for applied currents of ± 0.5 mA. $V_J(\tau)$ is proportional to ΔT_{pt} through V_J, but it is not proportional to either the magnetic state of the sample or ∇T_z. We observe that V_J relaxes to zero faster than the laser repetition period, indicating that the sample thermally recovers between pulses. To quantitatively consider the spatiotemporal thermal evolution, we performed a time-domain finite element (TDFE) calculation of focused laser heating in the wire. Additional details are available in section 4.5.3, and Ref. [63] for a lengthier discussion of the procedure. The comparison of the spatiotemporal profile of the calculation and the known temperature dependence of resistivity enable us to calibrate the spatiotemporal temperature rise due to laser heating. We find that the peak film temperature changes by ~50 K in the platinum and ~ 10 K in the YIG for a laser fluence of 5.8 mJ/cm^2, which is the maximum for the presented measurements. Note that we assume all laser heating is mediated by optical absorption in Pt because YIG and GGG are transparent at 780 nm [123,124]. The TDFE calculation reveals that, in agreement with experiment, ∇T_z across the YIG thickness decays more quickly than the full thermal relaxation of the Pt back to the ambient temperature (e.g. $\Delta T_{pt} = 0$). This difference in timescales between ∇T_z and ΔT_{pt} is important because the magnetic signal in our experiment is sensitive to only $\nabla T_z(t)$, not $\Delta T_{pt}(t)$ of the Pt.

The sub-100 ps spin current lifetime in our experiment is short enough that the TRLSSE is useful for stroboscopic measurements of resonant YIG magnetization dynamics. To confirm

this idea, we use TRLSSE microscopy to measure ferromagnetic resonance (FMR) by driving a gigahertz-frequency a.c. current into the Pt, which generates magnetic torques on YIG from both the Oersted magnetic field and from spin currents generated by the spin Hall effect [125–127]. The current is generated with an arbitrary waveform generator (AWG) that is phase-locked to the laser repetition rate and coupled to the YIG/Pt device through a circulator (see schematic in Figure 4.3a). Synchronizing the a.c. current and the laser repetition rate ensures a constant but controllable phase between the precessing magnetization and the sensing heat pulse for a given driving frequency and magnetic field. In our FMR measurements, we fix $\tau = 0$ and align the wire axis parallel to the external magnetic field. In this configuration, the TRLSSE signal is stroboscopically sensitive to the magnetic projection m_y at a particular phase of the magnetic precession about the *x*-axis. In addition to V_{LSSE}, V_{sig} contains a contribution from V_J that is proportional to the local a.c. current amplitude and phase [122]. We separate the magnetic V_{LSSE} from the non-magnetic V_J by measuring V_{sig} with a lock-in amplifier referenced to a 383 Hz, 7.6 Oe RMS modulation of the external magnetic field. Figure 4.3b shows LSSE FMR spectra as a function of field excited using a 1.2 ± 0.3 mA and 1.4 ± 0.4 mA a.c. current at 4.1 GHz and 4.9 GHz respectively. In the limit that the modulation magnetic field is small compared to the FMR linewidth, we can interpret the resulting signal V_{mod} as a derivative signal that contains a linear combination of the real and imaginary parts of the dynamic susceptibility, χ, $V_{mod}(H) \propto \frac{d\chi'}{dH} Sin(\theta) + \frac{d\chi''}{dH} Cos(\theta)$. This relation is used to fit the FMR spectra to extract the amplitude, phase, linewidth, and resonant field. For more details on fitting see refs [63,122]. To demonstrate that the TRLSSE microscope is a phase-sensitive stroboscope, we rotated the phase of the microwave current by 180° and re-measure FMR. As expected, inverting the phase of the drive inverts the phase of the FMR lineshape (Figure 4.3c).

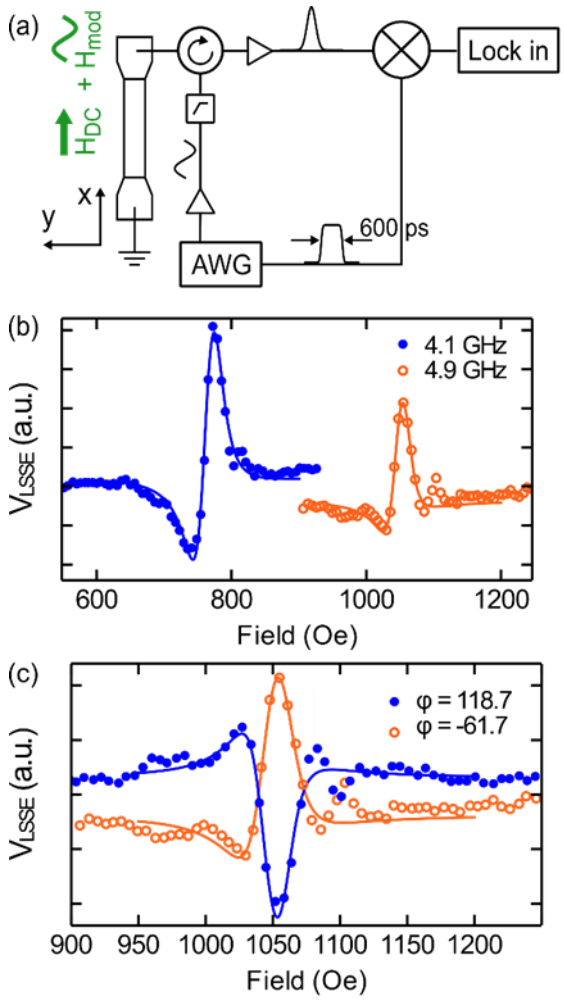

Figure 4.3 Stroboscopic detection of ferromagnetic resonance. a) Schematic of measurement circuit for detection of magnetization dynamics in the 2 μm wide wire. b) TRLSSE detected FMR for 4.1 GHz (blue, closed circles) and 4.9 GHz (orange, open circles) excitation. The solid lines are a fit to the data using a modified Lorentzian. c) Demonstration of stroboscopic FMR detection in which we measure the response of the YIG driven at phases that differ by 180 degrees. The data was acquired with a lock-in time constant of 1s and integration time of 5 s per point.

Next, we quantify the sensitivity of TRLSSE microscopy for our ultra-thin YIG/Pt samples. Figure 4.4 shows representative LSSE measurements of the YIG magnetization versus magnetic field perpendicular to the wire at several optical powers. In this geometry, the positive and negative saturation values of V_{LSSE} quantify the full range of magnetization, $+M$ to $-M$. Then, using the standard deviation of the noise in the LSSE voltage, σ_{LSSE}, we can quantify the angular

sensitivity noise floor assuming small angle magnetic deviations from the wire axis, such as for stroboscopic FMR measurements. The sensitivity is calculated using [63]

$\theta_{\min} = \frac{\sigma_{\mathrm{LSSE}}}{\sin(\theta_o)(V_{\mathrm{LSSE}}^{\max} - V_{\mathrm{LSSE}}^{\min})/2}\sqrt{TC}$ where *TC* is the lock-in time constant. We find a sensitivity of 0.3 deg/√Hz for an optical power of 0.6 mW, corresponding to a laser fluence of 5.8 mJ/cm^2. It is important to note that the sensitivity is sample dependent through both sample geometry and the impedance match with the detection circuit [63].

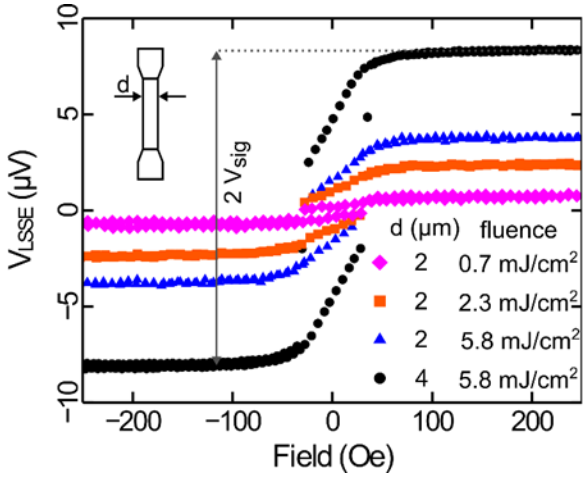

Figure 4.4 Measurement of YIG magnetization with LSSE measuring V_{LSSE} versus external magnetic field for different laser powers and wire widths. For these curves, a DC background was subtracted. The inset shows the wire geometry. We define the signal size to be one-half of the difference in voltage when the magnetization is saturated in opposing directions. The data was acquired with a lock-in time constant of 500 ms and integration time of 2 s per point.

The interface quality of the sample plays a key role in determining the sensitivity. As spin current diffuses into the platinum, it is subject to loss at the interface. A good indication of interfacial spin transparency is the spin Hall magnetoresistance (SMR) [128,129], which is sensitive to the spin mixing conductance at the interface. For the data presented here, the devices show a SMR of 0.063%, which is the largest value by a factor of 2 from the other devices we patterned. This is consistent with a number of recent SMR reports [128–132], and we expect the

high SMR value indicates strong spin transparency at the YIG/Pt interface. We also studied YIG/Pt samples with no measurable SMR which we expect to have a significantly reduced LSSE induced ISHE voltage. We found that the LSSE signal in these devices is approximately an order of magnitude lower for the same laser fluence. Additional details are in section 4.5.4.

Having placed upper bounds on the time resolution and quantified the sensitivity, next we demonstrate the application of TRLSSE microscopy for imaging of static magnetization. We acquire images by scanning the laser focus and making a point-by-point measurement of the TRLSSE voltage and reflected light. Figure 4.5a and b show a reflected light image and saturated LSSE image, respectively, for a 4 μm wide YIG/Pt device. In the reflection image, we see the structure of the wire and the contact pads at both ends. We acquired the TRLSSE image at $H = -405$ Oe and shifted the background level for clarity of the color scale. No other image processing was performed. We observe a uniform magnetization state of the YIG/Pt device, as expected from the previously presented magnetic hysteresis measurements (Figure 4.4). When we reduce the field to near zero ($H = 4$ Oe) and re-image the wire (Figure 4.5c), magnetic texture is revealed that indicates non-uniform canting of the device magnetization. To more clearly show the variation in contrast between images, we plot line cuts of Figure 4.5a-c in Figure 4.5d. Despite the inhomogeneous remanence that is evident in Figure 4.5c, we were not able to observe domains with oppositely aligned magnetization; possibly because once a reversal domain is nucleated, the domain wall propagates without strong pinning.

Without a 180^{o} domain wall the spatial resolution of TRLSSE cannot be directly evaluated. Nevertheless, we use the reflected light image and TDFE simulations to study the possibility that lateral thermal spreading degrades the resolution. To approximate the lateral point spread function of the laser, we fit a scan of the wire step edge to a Gaussian point spread

function. This yields a spot FWHM of 0.606 μm. Calculations of the heating indicate that the thermal gradient does not spread laterally in the Pt, thus we expect that the resolution of the TRLSSE is the same as the diffraction-limited optical resolution in this experiment.

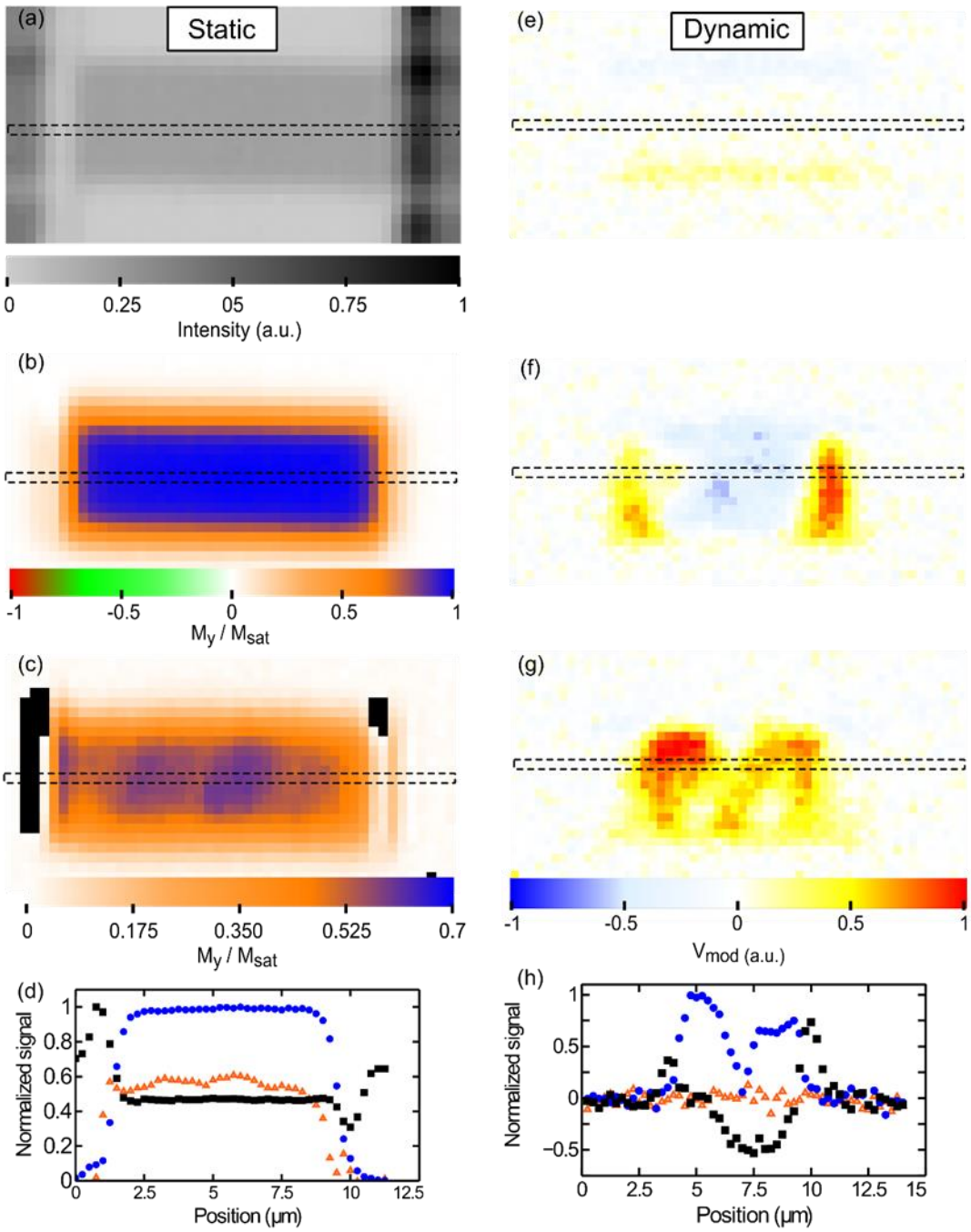

Figure 4.5 Images of the 4 μm wide YIG/Pt wire. (a) Reflected light image of the YIG/Pt wire measured with a photodiode at the same time as the LSSE voltage. (b) Background subtracted LSSE voltage at saturated magnetization and (c) remnant magnetization at 4 Oe after saturation. (d) Line cuts of the 2D scans. The normalized reflection signal is shown with black squares, blue circles represent the saturated magnetization, and the orange triangles represent the

magnetization of the remnant state. Note, that in the line cuts the low field line cut is normalized with respect to the saturation magnetization. The right side of the figure represents the raw images of the 4 μm wire at different fields around the resonance: (e) 896 Oe. (f) 1007 Oe, (g) 1025 Oe. Images (e-g) share the same color scale. Line cuts of the images are shown in (h) black squares, blue circles, and orange triangles correspond to the boxed regions of (e), (f), and (g) respectively. For (e-g) the data was acquired with a lock-in time constant of 200 ms and an integration time of 2 s.

We now demonstrate that TRLSSE microscopy has the sensitivity to image dynamic magnetization in the 4 μm YIG/Pt device, which provides quantitative and spatially localized information about dynamical properties of ultrathin YIG materials. As described above, for FMR characterization we orient the external magnetic field parallel to the wire axis and drive a 1.2 ± 0.1 mA, 4.9 GHz current into the wire. We image dynamical magnetization at a series of magnetic fields near the resonance field, from H = 896 Oe to 1105 Oe, and plot a selection of the unprocessed images in Figure 4.5e-g. The data show that at H far from resonance (Figure 4.5e) where precession amplitudes are tiny, the TRLSSE signal at the center of the wire is well below the detection noise floor. There is a small, current-induced, non-magnetic signal artifact at the edges of the wire which we discuss further in section 4.5.6. For H near the resonant field, H_{res}, the device has a strong, position-dependent TRLSSE response. To quantitatively analyze the data, images are corrected for background offset and sample drift before fitting a resonance field curve for each pixel. We plot a selection of curves from individual pixels in Figure 4.6a. We then construct a spatial map of each fitting parameter: H_{res}, relative phase, ϕ, amplitude, A, and linewidth, ΔH, and offset, all of which are shown in Figure 4.6b-f. We immediately notice spatial variation in these images that is qualitatively similar to the non-uniform magnetic remanence texture shown in Figure 4.5c. Together, these measurements confirm the presence of varying local magnetic anisotropy and quantify both static and dynamic magnetic properties in each

region. The ability to quantitatively relate the spatial variation of static and dynamic properties in ultrathin YIG/Pt devices is a unique capability of our microscope.

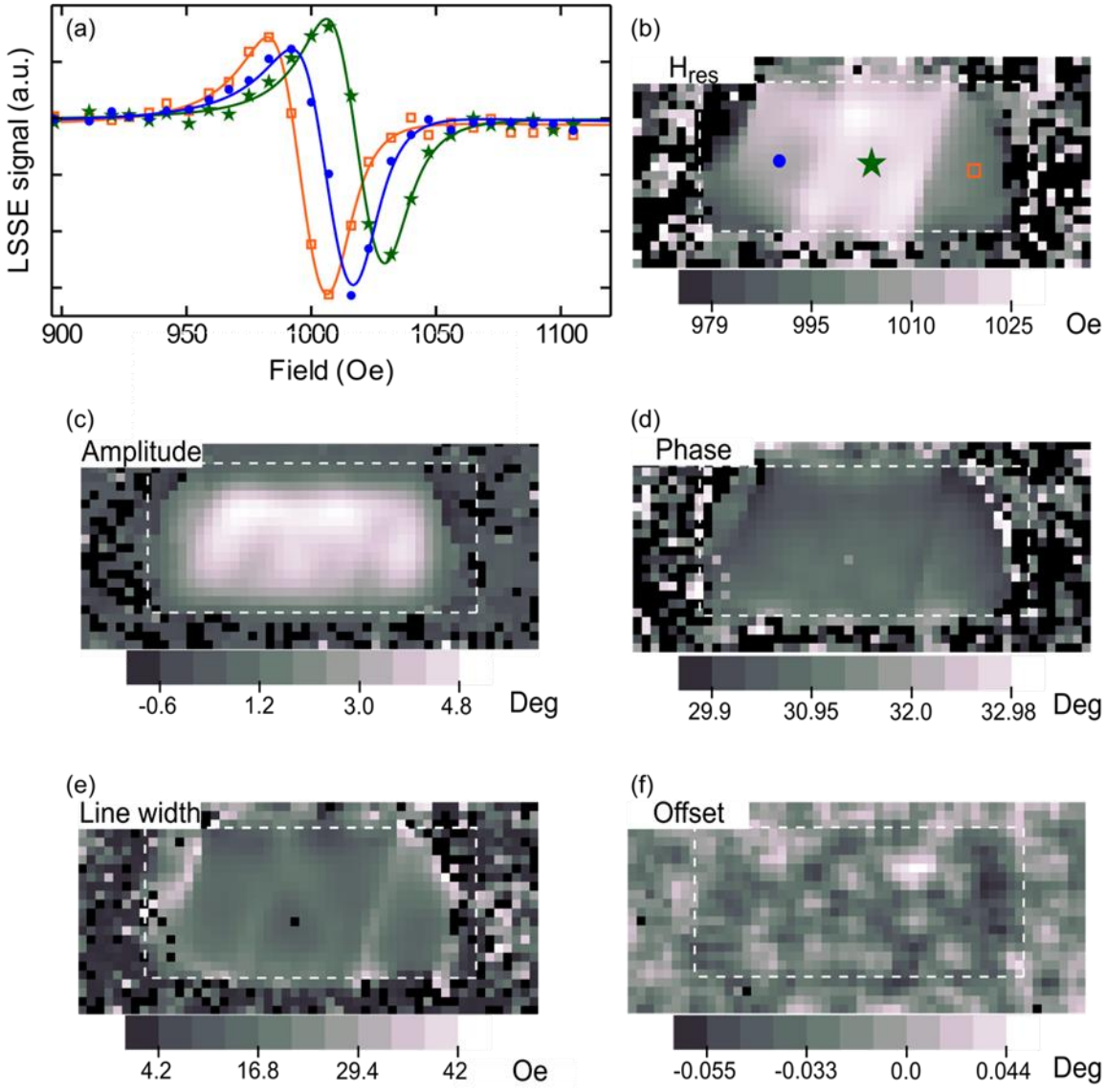

Figure 4.6 Spatial maps of FMR fitting parameters for the 4 μm wide wire. (a) Traces are the pixel values of three points on the sample as a function of magnetic field. b-f) Spatial maps of the FMR fitting parameters made by fitting of the FMR curves at each pixel in the sequence of images measured with LSSE. Before fitting, we correct for image-to-image offset and use a 3x3 pixel moving average to smooth the data. (b) Resonance field, the symbols mark the pixels corresponding to the FMR spectra shown in (a). (c) Resonance amplitude, (d) resonance phase, (e) resonance linewidth (f) offset used in the fit.

In conclusion, we have demonstrated sensitive and high-resolution TRLSSE microscopy of ultrathin YIG/Pt devices that we expect will prove useful for developing spintronic applications. Using picosecond heating, we demonstrate that TRLSSE microscopy is a sub-100 picosecond probe of ultra-thin YIG/Pt device magnetization, both for static magnetic configurations and for dynamical measurements at gigahertz frequencies. We have demonstrated an angular sensitivity of $0.3°/\sqrt{Hz}$, making it one of the most sensitive experimental probes of ultra-thin YIG magnetic orientation.

4.5 Supporting data and experimental details

4.5.1 Optical path

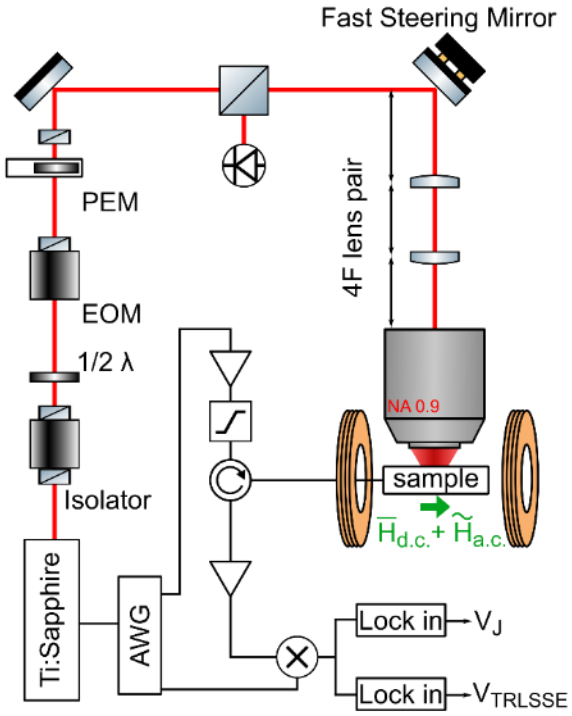

Figure 4.7 Schematic of TRLSSE microscope.

To heat the YIG/Pt bilayers, we use a Ti:Sapphire laser tuned to 780 nm and pulse durations of 3 ps at 76.5 MHz. An electro-optic modulator referenced to the laser pulses is used to reduce the repetition rate to 25.5 MHz, which allows time for thermal recovery. Next, a

photoelastic modulator and a polarizer are used to modulate the optical amplitude at 100 kHz for lock-in detection. The resulting vertically polarized light is focused on the sample with a 0.9 NA objective. A fast-steering mirror with a 4-f lens pair is used to scan the laser focus across the sample. The light reflected from the sample is detected with a photodiode bridge.

4.5.2 Model of TRLSSE temporal convolution

We develop a model of the detection circuit to clarify the impact of circuit bandwidth and electrical artifacts on the TRLSSE traces shown in Figs. 2b and 2c. The time domain measurements shown in Figure 4.2 show that the duration of V_{sig} matches the ~100 ps duration of the mixing pulse. This implies that thermal gradient induced V_{LSSE} must be sufficiently short-lived to sample the mixing pulse, and thus it is suitable for stroboscopic measurement of GHz frequency dynamics. In addition to the main pulse, we also observe oscillations that can be attributed to non-idealities in the mixing reference pulse produced by the arbitrary waveform generator (AWG) and the RF mixer itself. To account for these effects, we develop a phenomenological model of the signal, which we describe as the convolution of the TRLSSE-induced electrical pulse from the sample and the reference pulse from the AWG as a function of relative delay, $\boldsymbol{\tau}$ [63]. We account for bandwidth contributions and the realistic profile of the mixing reference pulse.

The model consists of a 12 GHz low-pass filter leading to the radio frequency and local oscillator inputs of an idealized mixer (Figure 4.8a). The output of the circuit is described by

$$V_{sig}(t) \sim \mathcal{F}^{-1}[\mathcal{F}(V_{mix}) * \mathcal{F}(V_{LSSE}) * LP(f)^2] \tag{4.1}$$

Where *LP(f)* is a first-order low-pass filter $LP(f) = \frac{1}{1+f/f_c}$ for frequency *f* and cut-off frequency f_c = 12 GHz. The Fourier transform $\mathcal{F}(V)$ is given by $\mathcal{F}(V_{\delta t}) = \frac{1}{\sqrt{T}}\sum_{\delta t=1}^{T} V_{\delta t}\ \mathrm{e}^{2\pi i(\delta t-1)(f-1)/T}$ where T = 12.9 ns is the duration of the kernel, δt = 2.5 ps is the time step, and *f* is frequency. In

the experiment, the mixing pulse V_{mix} is generated by an arbitrary waveform generator (AWG) synchronized to the laser repetition rate with a sampling rate of 9.98 GSamples/s. For mixing voltage pulse V_{mix} we use the output of the AWG measured using a LeCroy SDA 11000 Oscilloscope (Figure 4.8b). To model the signal from the sample, V_{LSSE}, we use the normalized thermal gradient determined from time-domain finite element (TDFE) calculations (further discussion below). In the main text, we use a 100 ps mixing pulse to acquire the data presented in Figure 4.8b,c. and a 600 ps mixing pulse to acquire the other data.

Figure 4.1 shows V_{sig} calculated via Eq. (4.1) normalized to the measured data along with the measured convolution. The model qualitatively captures the oscillations at delay times greater than 100 ps. This model, together with the lack of magnetic field dependence, supports the idea that the oscillations in the data are electrical artifacts, not magnetic oscillations.

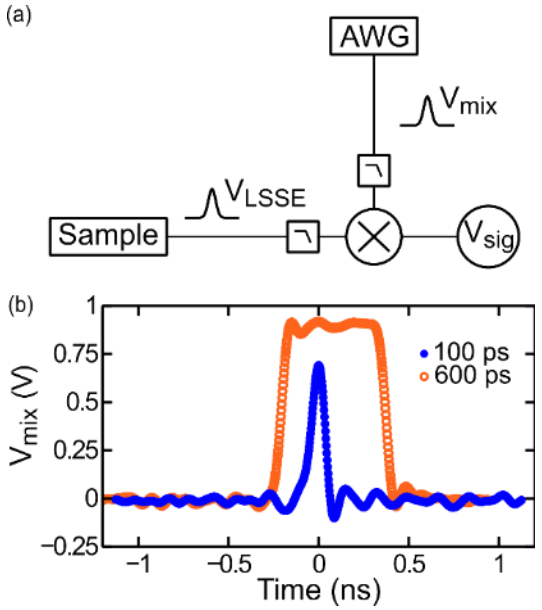

Figure 4.8 Diagram of TRLSSE mixing circuit. (a) Schematic of circuit model for interpretation of time-domain circuit. The arbitrary waveform generator (AWG) creates a mixing pulse that goes through a 12 GHz low-pass filter before being mixed with the pulse from the sample that has also been sent through a 12 GHz low-pass filter. (b) Oscilloscope measurements of the mixing pulses used in the experiments.

4.5.3 Determination of temperature change from laser heating

Although we know the laser fluence, we do not know the film absorbance for this thin-film limit in which the Pt film is much thinner than the optical skin depth. To determine the temperature change in our experiment we use the following methodology: (1) we numerically calculate the spatiotemporal thermal response to focused laser heating assuming the peak absorbed power is 1 W (an absorbed fluence of 0.7 mJ/cm^2). We take the model's predictions for the spatiotemporal thermal evolution to be correct but the total temperature change amplitude as being uncalibrated. (2) We calibrate and measure V_J, which is equivalent to using the sample resistivity change as a thermometer. (3) We calculate the V_J from our spatiotemporal thermal model calculations and compare it to the measured V_J. We assume there is linear response between the amplitude of the absorbed laser energy and the maximum temperature increase, therefore the ratio of the measured to the calculated values of V_J determines the scale factor of the absorbance. This also scales the temperature increase from the model to a value that agrees with our electrical measurement. Additional details have been described previously in the supporting information of Ref. [63].

We base our model on TDFE calculations of thin-film thermal diffusion to determine the spatiotemporal profile of the thermal gradient temperature distribution. We consider a GGG/YIG(20 nm)/Pt(6 nm) trilayer with material parameters given by Table 2. The YIG/Pt layers are modeled as a 2 μm x 10 μm bar to match the measured device. Heat transfer in the structure is calculated using the diffusion equation

$$\rho\, C_p \frac{\delta T(\mathbf{x},t)}{\delta t} - \kappa \nabla^2 T(\mathbf{x},t) = Q(\mathbf{x},t) \tag{4.2}$$

with the COMSOL Multiphysics® software package. In Eq. (4.2) ρ is the material density, C_p, is the specific heat, κ, is the thermal conductivity, Q is the heat source, $\mathbf{x}$ is the 3D spatial

coordinate, and *t* is time. We assume the YIG/ Pt interfacial thermal conductance is 170 W m^{-2} K^{-1} [111].

We also assume that laser heating only takes place in the Pt layer because of the negligible optical absorption in the YIG [133] and GGG [124]. Thus, the laser is effectively a radially symmetric heat source, with radius *r*, in the platinum with a spatial temporal distribution, for positive z, given by, $Q(\mathbf{x},t) = Exp\left(-\frac{z}{\varepsilon}\right) * \left(\frac{1}{2\pi\, d^2}\right) * Exp\left(-\frac{r^2}{2\, d^2}\right) * Exp\left(-\frac{(t-t_0)^2}{2\, w^2}\right)$, where d = 257 nm is the focused laser spot size (see "determination of optical spot size" below), ε = 12 nm is the skin depth [134,135], w = 1.27 ps is the laser pulse width for a 3 ps FWHM Gaussian pulse, t_0 = 100 ps is the time that the heat source is at the maximum. The heat source is applied every 39.6 ns and the simulation runs from time t = 0 ns to t = 42 ns to capture two pulses.

Figure 3.9 shows the result of the model calculation in the space and time domains. The z-component of the thermal gradient within the YIG decays to 1/e in 92 ps and the temperature difference between the Pt and YIG decays in 91ps, time scales that are experimentally indistinguishable in our measurement and consistent with the time domain measurement shown in Figure 4.2b,c. The overall temperature increase within the laser heated region takes longer to relax to room temperature, 295 ps, consistent with Figure 4.2d. These calculations support that the TRLSSE signal originates from $\nabla T_z(t)$ (or indistinguishably in this work, the temperature difference between YIG and Pt) and that it is localized in time making it suitable for stroboscopic measurements.

The model calculation predicts about a 400 K change in the Pt, however, as discussed above, we calculated the amplitude of the laser-induced temperature change without experimental knowledge of the absorbed fluence. Therefore, the true temperature change in the Pt may be scaled up or down to account for correct value of the absorbed laser power. To

establish the absorbance experimentally, we compare the measured values of V_J, which originates from the resistance change of the metal due to laser heating, with a model calculated value of V_J, which is determined from the resistance change expected from our model calculation. Specifically, we calculate V_J using the 3D temperature distribution created from laser heating to determine the sample resistance increase. We use the linear relationship between the resistance and the temperature, $R(T) = R_o(1 + \alpha\, T)$, with the resistance correction factor $\alpha = 1.3 \times 10^{-3}\,K^{-1}$ measured for the Pt films used in our experiment. To compare the calculated value to the experimentally measured V_J, we also determine the electrical circuit transfer function in which we account for the measurement bandwidth and gain (see Ref. [63] for further discussion). From this analysis we find that our experimentally measured V_J is 0.12 times the calculated V_J, indicating the peak temperature change in the Pt is 52 K, corresponding to a peak absorbed fluence of 0.09 mJ/cm^2, 1.6% of the incident laser energy. The uncertainty in the temperature is estimated to be on the order of 25% based on uncertainties in the circuit calibration.

Table 2 Material parameters used in the TDFE simulations of laser heating

	Specific Heat, C_p (J/kg*K)	Density, ρ (kg/m^3)	Thermal conductivity, κ (W/m*K)
Pt	133[a]	21500[a]	71.6[a]
YIG	570[b]	5170[c]	6[b]
GGG	400[b]	7080[b]	7.94[b]

[a]Reference [136]
[b]Reference [137]
[c]Reference [138]

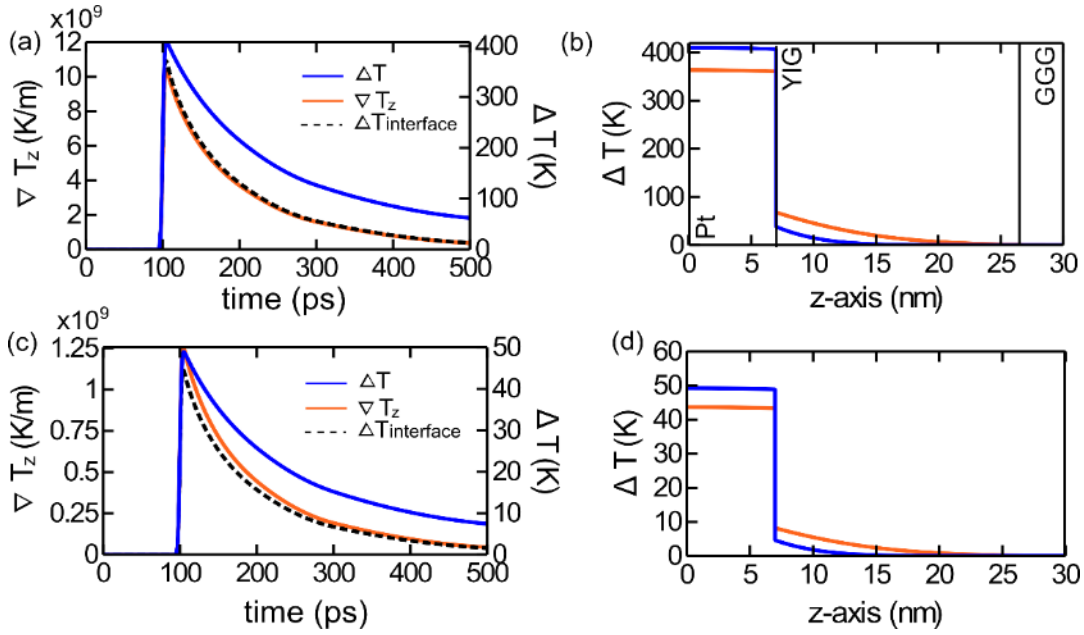

Figure 4.9 Time-domain finite element calculations of the temperature and thermal gradient using COMSOL. (a) Time-domain thermal profiles at the YIG/Pt interface calculated with COMSOL assuming an absorbed fluence of 0.7 mJ/cm^2 and showing the z-component of thermal gradient in the YIG (orange curve), change in temperature of the Pt (blue curve), and temperature difference between the Pt and the YIG across the interface (black dashed line). The laser turns on at 100 ps in the calculation. (b) Calculated temperature vs. z-axis position showing heating as a function of film depth at the maximum temperature difference (orange curve) and 16 ps later (blue curve). (c,d) The curves from (a) and (b) scaled by the correction factor.

4.5.4 Effect of interface spin transparency

The spin Hall magnetoresistance (SMR) is the change in resistance due to spin-dependent transport in a heavy, nonmagnetic metal that shares an interface with a ferromagnet [129]. Thus, for bilayers of the same materials but different spin mixing conductance, measuring SMR provides insight into the efficiency with which spins can cross the interface. The efficiency of interfacial spin transport is important for TRLSSE measurements because in order for the magnetization to be transduced into a voltage, the thermally driven spins must cross the interface.

For the data presented in the main text we find a SMR of 0.063%. We compare the signal from this wire with a relatively strong SMR to the TRLSSE signal from a wire without detectable SMR above the 0.003% noise floor of our lock-in measurement. Both wires were 2 μm x 10 μm with resistances of 296 Ω and 220 Ω for the sample with and without SMR respectively. The sample without SMR had a thinner YIG film (8 nm), however this is not expected to effect the SMR since SMR is an interfacial effect [128].

Figure 4.10 shows representative plots of the TRLSSE signal versus field for the different wires at similar laser powers. We find that the sample with SMR has a signal approximately an order of magnitude greater than the sample without. The difference is consistent with the model of TRLSSE driving spin current across the YIG/Pt interface. We also note that even though the signal is reduced, it is still measurable in both samples, enabling measurement of YIG magnetization even in systems that cannot be measured electrically.

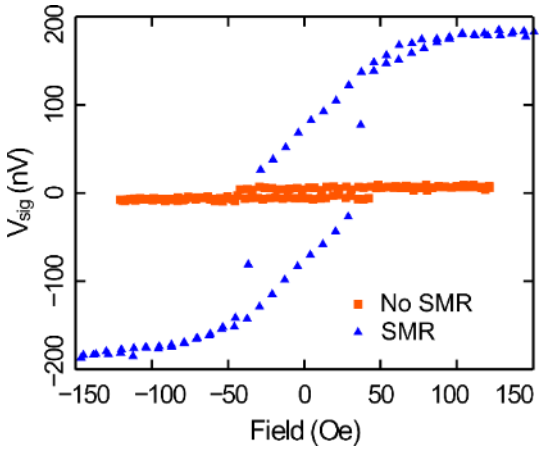

Figure 4.10 TRLSSE signal as a function of applied external field for a samples with 0.063% SMR (blue triangles) and a sample with no measurable SMR (orange squares). The applied laser fluences are 5.4 mJ/cm^2 and 6.7 mJ/cm^2 for the blue an orange curves respectively. For the data presented here, the laser repetition rate was 76.5 MHz and no amplifier was used between the sample and the RF mixer.

4.5.5 Determination of optical spot size

We determine the diameter of the illuminated area by modeling a Guassian laser focus and fitting the traces of the image shown in Figure 4.5a. Figure 4.11 shows a y-axis cross section of the image. The trace shows an approximately flat region on the wire surface and a sigmoidal edge due to the convolution of the sharp wire edge with the point-spread function of the laser focus. To fit the reflection signal, *I*, at the edge, we use the convolution of a Guassian with a step function,

$$I = \frac{1}{b\sqrt{2\pi}} \int_{-\infty}^{\infty} \exp\left(-\frac{(x-a)^2}{2b^2}\right) \Theta(x-a)dx, \tag{4.3}$$

in which b determines the Guassian width, a is the center of the peak, and Θ is the step function defined as $\Theta(x-a) = \begin{cases} 0, x < a \\ 1, x \geq a \end{cases}$. The fit of the data yields b = 0.240 ± 0.007 μm and b = 0.274 ± 0.010 μm for the left and right edges respectively. We take the average to be the optical spot size. We attribute the difference between the two edges to a slight out-of-plane tilt of the sample leading to asymmetry in the reflection.

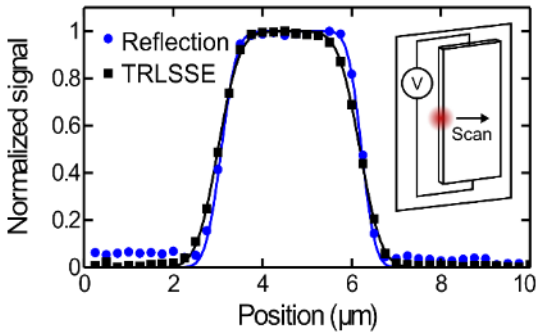

Figure 4.11 Fit of step edge signal for determination of optical spot size. (a) Line cut in y-axis direction of the reflected light image, shown in Figure 4.5a, and the TRLSSE image of the static saturated moment, shown in Figure 4.5b. (inset) Schematic representation of the sample tilt that can lead to the observed anisotropy.

As a comparison, we fit a y-axis scan of the TRLSSE signal to Eq. (4.3). The result gives $b = 0.380 \pm 0.006$ μm and $b = 0.381 \pm 0.009$ μm for the left and right edges respectively. This difference corresponds to a difference of ~1 pixel between the rise-width of the reflection signal and TRLSSE signal.

4.5.6 Analysis of dynamic TRLSSE images

To image the ferromagnetic resonance of YIG in the 4 μm wide wire a series of images was taken at fields ranging from 896 to 1105 for an applied RF power of 1.1 mA. A selection of unprocessed images is shown in Figure 4.5e-g. Although the signal is quite clear, we account for sample drift and noise, before fitting the FMR curves.

We correct for sample drift using autocorrelation to find the image overlap. The kernel for the autocorrelation is a 5 ×12.5 μm region from the center of the reflected light image at H = 896 Oe (the first image in the series). We determine the drift of subsequent images by finding the distance between the centers of the kernel and the minimum of the autocorrelation. Most of the sample drift is on the order of a pixel (0.25 μm) with a maximum sample drift of $\Delta y = 0.75$ μm and $\Delta x = 0.25$ μm. We correct for the offset by shifting the images and then cropping the borders. The scans cover a large enough area that the cropped region is well away from the wire. After correcting for the sample drift, we remove the background from the vibration edge artifacts by subtracting the TRLSSE signal of the wire at 896 Oe from the subsequent images. Finally, we reduce random pixel to pixel noise, smoothing the signal with a 3x3 pixel moving average. The 3x3 pixel window is approximately the sampling spot size (see determination of optical spot size).

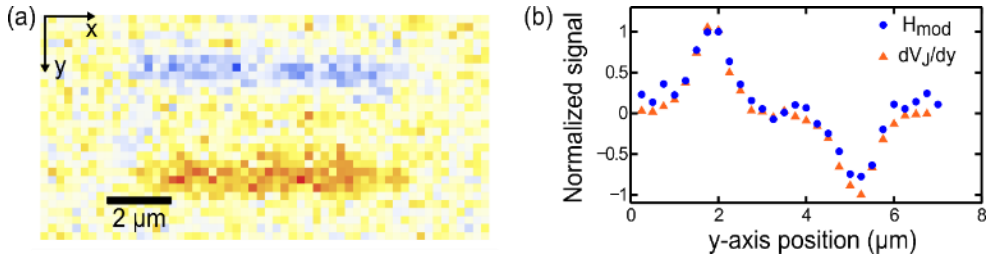

Figure 4.12 Analysis of the edge artifact in FMR imaging. (a) Spatial variation of the TRLSSE in a 4 × 10 μm YIG/Pt wire at 911 Oe. The signal measured by a lock-in amplifier referenced to the frequency of an a.c. magnetic field. (b) Profile of the TRLSSE signal shown in (a) (blue circles) and the derivative of V_J from the same area of the wire (orange triangles). The trace is the average of twenty-six y-axis line scans from along the length of the wire.

We attribute the small signal features at the edges of the wires in Figure 4.5 to magnetic field modulation induced relative motion between the microscope objective and the sample. As mentioned in the main text, we separate V_J (which is in principle non-magnetic) from V_{TRLSSE} (which is magnetic) by adding a modulation magnetic field (7.6 Oe RMS, ω_H = 383 Hz) to the d.c. magnetic field. We then demodulate V_{sig} with respect to ω_H using a lock-in amplifier. Although this procedure is effective for isolating V_{TRLSSE} from V_J when we focus in the center of the wire (away from the wire edge), the modulation field induces a tiny "wobble" in the laser focus on the sample. When the laser is focused on the sample edge and a current is applied to the sample, the wobble introduces a slight modulation of V_J at ω_H because $\frac{dV_J}{dH} = (\frac{dV_J}{dy})(\frac{dy}{dH})$, where $\frac{dy}{dH}$ is due to field-induced mechanical motion and $\frac{dV_J}{dy}$ is large at the sample edge. We note that these edge signals are independent of external field but that they are sensitive to the current amplitude and phase, both of which are consistent with this interpretation of the artifact. In Figure 4.12 we plot both the profile of the externally modulated field signal in the y-direction and the numerical derivative of V_J measured by the lock-in referenced to the 100 kHz laser modulation rate, which demonstrates their correspondence.

4.5.7 Funding acknowledgements

This research was supported by the U.S. Air Force Office of Scientific Research, under Contract No. FA9550-14-1-0243, and by U.S. National Science Foundation under Grants No. DMR-1406333 and DMR-1507274 and through the Cornell Center for Materials Research (CCMR) (DMR-1120296). This work made use of the CCMR Shared Facilities and the Cornell NanoScale Facility, a member of the National Nanotechnology Coordinated Infrastructure, which is supported by the NSF (Grant No. ECCS-1542081).

CHAPTER 5

IMAGING MAGNETIZATION WITH NEAR-FIELD SCANNING MAGNETO-THERMAL MICROSCOPY

5.1 Chapter introduction

The magnetic configuration in thin films, and devices made from those films, is determined by a rich energy landscape that can vary over nanometer length scales. At these scales, the orientation and magnitude of the magnetization is determined by both exchange and dipole interactions. Short-range exchange interactions, such as the Dzyaloshinskii-Moriya interaction (DMI) can cant magnetization and create quasi-particles known as skyrmions less than 100 nm across [139–141]. Dipole interactions, which are typically thought of as long-range, can contribute on the nanoscale as well. In nano-patterned devices for example, dipole interactions influence the switching of magnetic tunnel junctions [142,143], and determine the magnon band structure in magnonic crystals [144,145]. Although complex, the energy landscape that determines magnetic behavior is highly tunable, enabling technologies in information storage and processing. Moving forward, to compete effectively with all charge-based technologies, it will be important to understand and engineer magnetic and spintronic devices at nanoscopic lengths scales and picosecond time scales.

A necessary step to understanding and controlling magnetization is the development of microscopy techniques capable of imaging at the fundamental length and time scales of materials. Typically, the fundamental scales correspond to picosecond temporal resolution and sub-100 nm spatial resolution. Currently, to image magnetization with this a spatiotemporal resolution we need to use either x-rays or pump-probe electron microscopy techniques that require special sample preparation and which can only be done at a few facilities. It in addition to

these two methods, it would be useful to have a magnetic microscope that can image magnetic devices on a variety of substrates and no special sample preparation other than what is typical for transport measurements.

Magneto-thermal microscopy provides a route towards this goal. Time-resolved magneto-thermal microscopy using optical heating from focused pulsed lasers has proven useful as a sensitive measurement technique with picosecond temporal resolution; however, thermal gradients generated with far-field optics are still limited by the optical diffraction limit. To tap the full potential of magneto-thermal microscopy we adapt near-field optical techniques to create thermal gradients smaller than far-field Airy spot size. We use an apertureless near-field geometry in which the local electric field is enhanced beneath a sharp tip metallic tip to heat the sample [146,147,147–149]. Importantly, although this geometry is similar to some near-field MOKE measurements, it avoids the polarization artifacts that are prevalent in the near-field magneto-optical microscopy [150].

For several decades, near-field microscopes have been used to enhance the electric field in the gap between a sample surface and a probe tip [151–156]. This enhancement is often due to a combination of the so called ‘lightning rod’ effect and plasmonic effects. The lightning rod effect is a geometric effect in which the electric field is enhanced a sharp point. The plasmonic effects can vary but rely on the optical excitation of electrons at the interface between a metal and dielectric where the real parts of the dielectric constants are negative and positive respectively. This can lead to enhancement of the electric field either by creation of propagating surface waves that are confined by the tip and/or by resonant antenna effects at the gap between the tip and sample surface. Plasmonic antennas are currently being studied for heat-assisted magnetic recording (HAMR) [88,157] and tip-enhanced Raman spectroscopy (TERS) [146,149].

We build on the work in these fields to develop our scanning near-field magneto-thermal microscope.

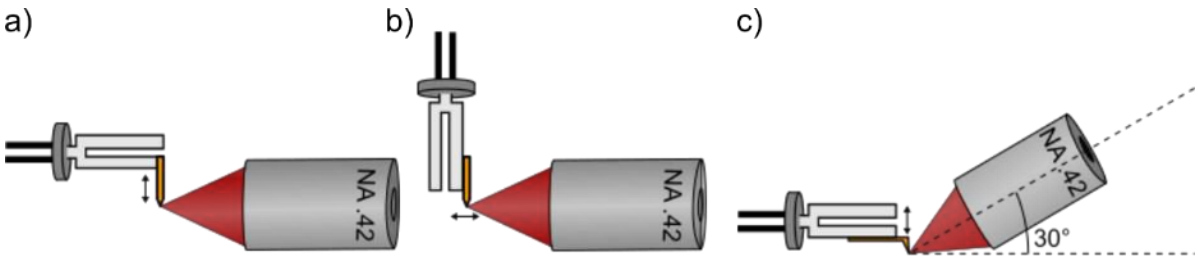

Figure 5.1 Schematic representations of the three scanning probe geometries. a) Tapping AFM with an etched gold wire illuminated at the apex at a zero-degree angle with respect to the surface normal. b) Shear-force geometry with an etched gold wire illuminated on the grating coupler at a zero-degree angle with respect to the surface normal. c) Tapping AFM with a gold-coated silicon cantilever illuminated at the apex at a thirty-degree angle with respect to the surface normal.

In this chapter we present results demonstrating the application of near-field scanning optical microscopy (NSOM) for local heating of thin metallic films and TRANE microscopy. The NSOM is based on a custom-built quartz tuning fork AFM that uses a sharp gold tip. Using a tuning fork enables electrical monitoring of the tip-to-sample distance which removes the need for optics that can contribute spurious optical heating and enables compact packaging. More details on the tuning fork are covered in Chapter 6. There are three scanning probe geometries that we investigate in this chapter: tapping mode with an etched gold wire, tapping mode with a gold-coated silicon cantilever, and shear-force mode using an etched gold wire. The geometries are shown in Figure 5.1. For each of these cases we comment on the advantages and disadvantages. We find the gold-coated AFM tip to give the most consistent results and characterize the sensitivity and estimate the resolution for this case. We conclude with a look toward future work and possible improvements.

5.2 Tapping atomic force microscopy with directly illuminated etched gold wires

The first geometry we explore is the AFM tapping mode shown in Figure 5.1a. The tip is a 250 μm wire that have been etch to a sharp point via the method described in [158]. After etching, the tip is then glued to one tine of a quartz tuning fork and counter balanced by gluing a short piece of wire the opposing tuning fork tine. Counterbalancing increases the tuning fork quality factor from ~200 to ~500. The tuning fork is excited in self-oscillation mode and the tip-sample distance is kept constant by keeping a constant frequency shift using a proportional-integral feedback loop. A flexure stage piezo sample scanning stage moves the sample beneath the tip.

The sample that we used in this experiment was a 2 × 10 μm YIG(20 nm)/Pt(6)/Ru(2) wire. This is the same type of wire studied in Chapter 4, though not exactly the same wire. The YIG/Pt bilayer structure has the advantage that near-field optical excitation of Pt generates a point spread function localized beneath the tip apex. Materials with higher conductivity can generate circular heat spots and less conductive metals are less efficiently excited by the optical field [159]. Moreover, we can apply a current through the platinum and measure the signal due to local, temperature-dependent resistance. Thus, by switching the current polarity, we see a clear signal variation and get an estimate of the sensitivity while the tip is at the surface even without having an external magnetic field.

To heat the samples, 3 ps pulses of vertically polarized, 780 nm light from a Ti:Sapphire laser are focused onto the tip apex at the sample surface with a long working distance, 0.42 NA objective. The microscope objective is oriented at a nearly zero-degree angle with respect to the sample surface normal. To reduce the effect of shadowing from the wirebonds and contact pads, the sample is oriented with the long axis perpendicular to the incident light. We measure the

magneto-thermal voltage from the sample using a custom homodyne detection circuit that has been discussed in Chapter 3. For the work in this chapter, the reference pulse duration is 1 ns and generated by an arbitrary waveform generator (AWG) that is synchronized to the 76 MHz repetition rate of the laser pulses. We increase the signal-to-noise ratio and separate the near-field signal from the background using a dual-demodulator lock-in amplifier.

Each scanning probe measurement generates three simultaneously collected images, the tip height, the voltage from the sample demodulated at the frequency of the optical chopper, and the signal demodulated at the frequency of the tuning fork resonance or its harmonic. Figure 5.2 shows examples of these three images.

To measure the data shown in Figure 5.2, we scan the tip back and forth in the *x*-direction while we change the current and optical illumination as indicated in Figure 5.2a. Figure 5.2b shows the averaged, *x*-direction line cuts measured at the first, third, and fifth, harmonic of the tuning fork frequency. Harmonics of the tuning fork frequency are expected because the tip induced near-field signal falls off rapidly with tip height. Thus, observing these higher harmonics is a good indication that the signal is due to a near-field effect between the scanning tip and sample. These harmonics can also be used to improve the signal-to-noise ratio [160].

The dips observed at the edges of the wire are likely due to ac electrical conduction between the tip and the wire. The gold wire on the tuning fork is likely capacitively coupled to the electrode that drives the tuning fork through the piezo electric effect. If the tip contacts the sample (which is mostly likely when it is climbing a step edge) then there will be an electrical artifact at the harmonics of the tuning fork frequency. This interpretation is supported by the fact that the artifacts are overserved even when the laser is blocked and there is no dc current in the wire as seen in Figure 5.2c.

Figure 5.2d-f shows the voltage demodulated at the frequency of the optical chopper. This signal is the voltage generated just by the directed optical heating of the focused light from the microscope objective. It is the averaged traces of this “far-field” data are not only several orders of magnitude higher than the near-field signal, but also less sharply localized around the wire. The lack of resolution is due to the oblique angle of the incident light, nevertheless, the sharper features of the near-field signal has higher resolution by virtue of the sharp tip. It is impossible to make a stronger statement about the resolution since it would require a feature inside the wire that was on the order of the tip point-spread-function or smaller.

We note that in Figure 5.2f, there is periodic intensity variation parallel to the wire length. This is most likely caused by diffraction from the step edge of the wire. This sample structure related artifact appears in Figure 5.6 and Figure 5.8 as well where, again, the ripples are perpendicular to the incident direction of the laser.

The line traces in Figure 5.2c,d were taken when either the laser was blocked (red line) or the dc current was turned off (blue line). The red trace serves as a check that the voltage is generated by the laser, which it is, aside from the edge artifacts. The blue trace on the other hand is not zero and must arise from a thermally generated voltage in the wire itself. To investigate this further and determine whether it originates from the anomalous Nernst effect we measure the wire after applying saturating magnetic fields with a permanent magnet.

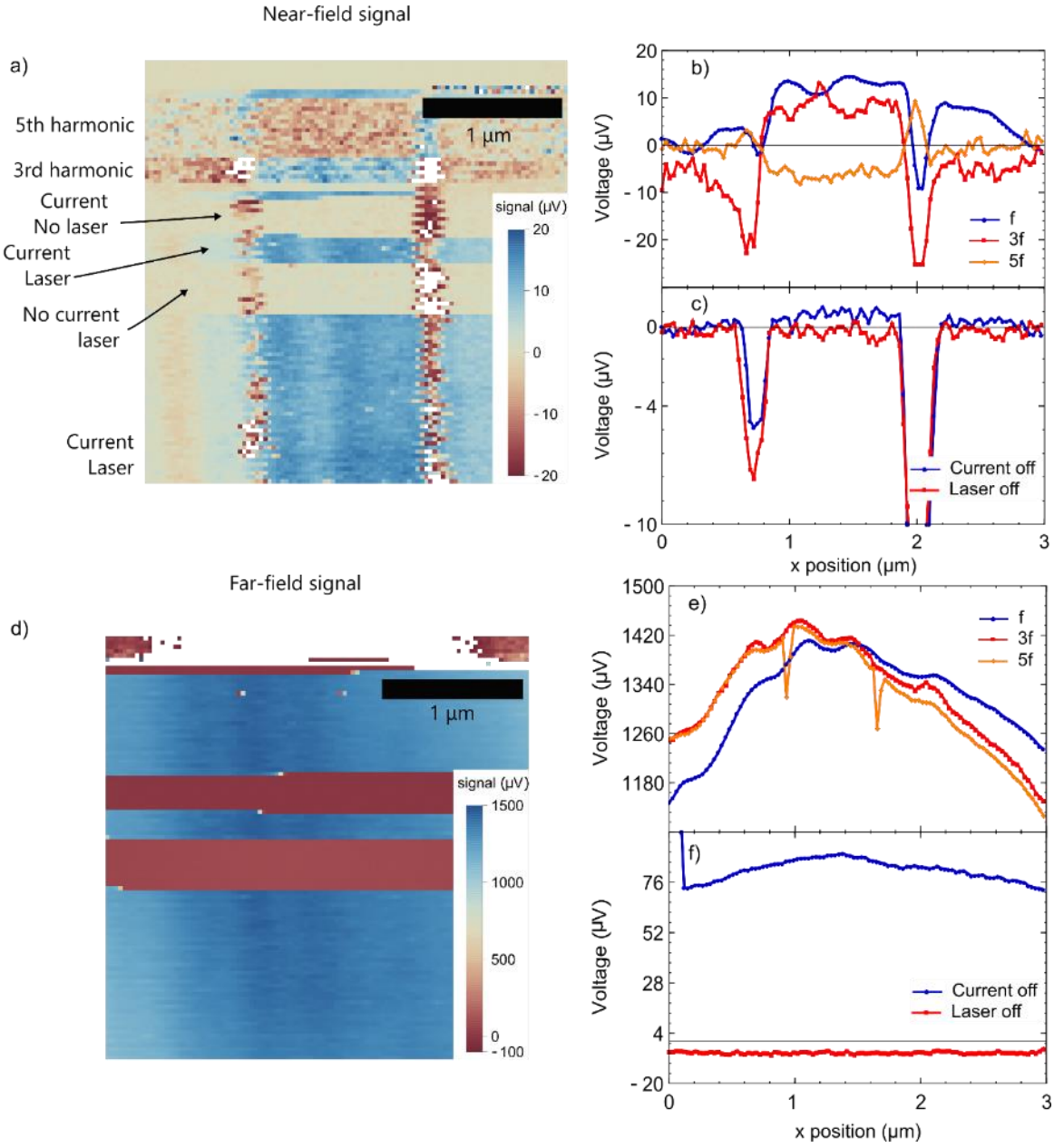

Figure 5.2 Images and line cuts of near and far-field signals using tapping AFM etched gold wires showing sensitivity to current flowing through the wire. a) Signal demodulated at the frequency of the tuning fork or one of its harmonics. b) Traces showing the average of the horizontal line cuts in the region of a) where the laser and current were both on but different harmonics were being measured. c) Average of the horizontal line cuts of a) in the region where either the laser or current was turned off. d) Voltage demodulated at the frequency of the optical chopper. e) Traces showing the average of the horizontal line cuts in the region of d) that match the regions averaged in b). f)

Average of the horizontal line cuts of d) in the region where either the laser or current was off. The current density was 1.25×10^6 A/cm^2 and the laser power was 3 mW.

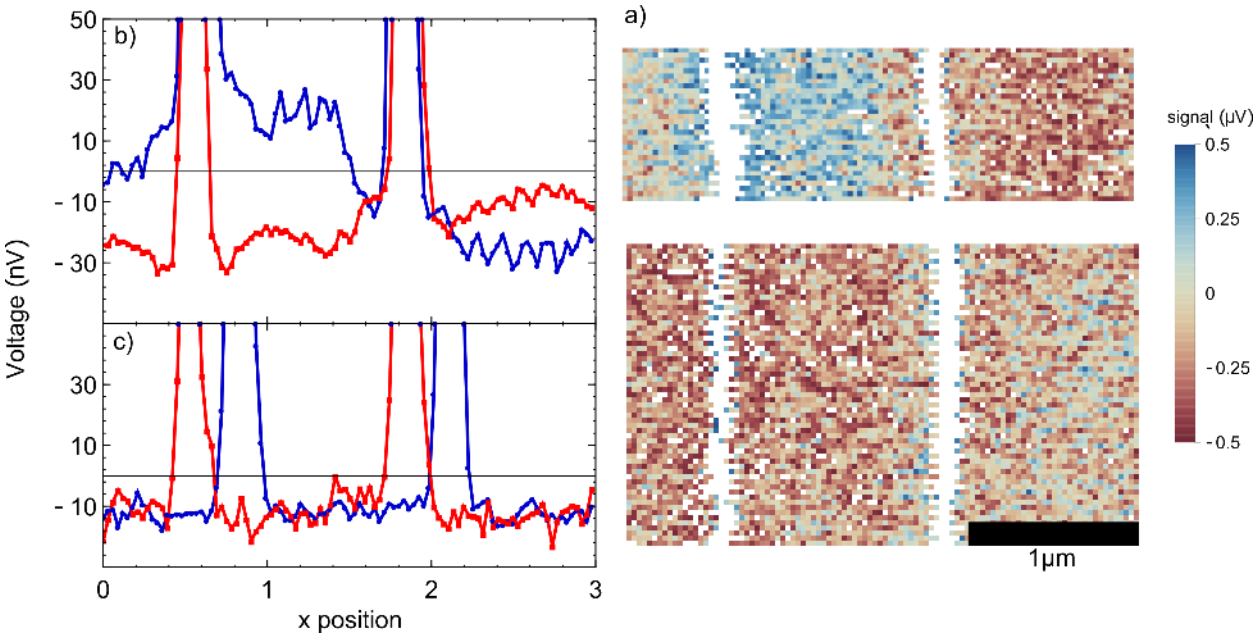

Figure 5.3 Images and line cuts of near and far-field signals using etched gold wires in the tapping geometry. a) 2D plots of the voltage referenced to the frequency of the tuning fork oscillation. The top and bottom images show the scans after the wire was magnetized in opposite directions with a permanent magnet. The scans were taken in zero magnetic field. b) line plots showing the average values of the two images shown in (a). The blue line is the average of the top image and the red line is the average of the bottom image. c) Line plots showing the average of scans taken over the YIG sample but without the laser illuminating the scanning tip.

To confirm that we are sensitive to the magnetization of the YIG we scan the YIG/Pt wire again, this time however, we first use a permanent magnetic to initialize the moment of the YIG perpendicular to the channel length. To saturate the moment, a permanent magnet is brought close to the sample (applied field magnitude is >500 Oe) and then removed so that the scans are taken in zero magnetic field. Thus, the scans measure the remnant state of the YIG magnetization. We confirm that the sample is magnetized by measuring the voltage due to the

far-field heating and find that the voltage switched between +50 μV and -50 μV for oppositely directed magnetization.

In Figure 5.3 we show scans of the YIG/Pt sample after it had been saturated perpendicular to the wire. Part a) of the figure shows the 2D plots of the voltage measured at the frequency of the tuning fork. The figures are noisy and have the same edge artifacts, however, there is a noticeable difference in contrast between the two magnetization directions (top and bottom images). The difference is more obvious when all the lines are averaged in the *y*-direction and plotted as the traces in Figure 5.3b. The signal difference is 550 nV and there is a polarity change suggesting that we are measuring the magnetization state of the YIG/Pt wire via the LSSE and a near-field effect. We confirm that the zero-level is less than the LSSE by blocking the laser during the scan for several lines Figure 5.3c.

The data in Figure 5.2 and Figure 5.3 show a proof-of-concept that scanning probe imaging of magnetic samples is capable of resolution higher than the focused light used to illuminate the tip, that the tip generated signal is sensitive to both the magnetization, and sensitive to the dc current flowing through the wire. There are significant challenges with the data as well. The signal-to-noise ratio is too low to be practical for imaging, the background from direct heating is orders of magnitude above the scanning probe signal, and, most importantly, we cannot confirm that the tip is enhancing the interaction and not simply locally blocking the laser.

Blocking of the laser by the tip is a reasonable explanation because it would also be a non-linear effect that produces harmonics. In principle, the sign of the near- and far-field signals should be opposite if the tip was blocking the light instead of enhancing it. However, at the beginning of the measurement, we adjust the lock in phase to maximize the signal in both the far-field and near-field signals. This could lead to an error in the sign if the signals are out-of-phase

by π. To decrease the background and provide better evidence that the scanning probe tip is leading to an enhancement we next try to use the etched gold wire as a scanning probe tip. To ensure that we do not crush the fragile gold tip, we move to a shear-force geometry.

5.3 Shear-force microscopy with adiabatic nanofocusing

In this section we provide evidence that electrochemically etched gold wires can be used as scanning antennas for local measurement of current in Pt wires. In addition to using the scanning antennas, we also use the shear-force scanning probe geometry shown in Figure 5.1b. In the shear-force geometry, the etched, gold tip is oriented so that it oscillates parallel to the surface of the sample. When the probe is brought close to the surface, the surface exerts a force tip reducing the tuning fork vibration amplitude [161]. The origin of the force is a matter of some debate nevertheless, since all experiments are in air, it is reasonable to believe that a thin layer of water adsorbed to the surface creates a drag on the vibrating tip [162,163]. The lateral vibration of the tip enables us to keep the probe at a constant height, reducing the possibility of contact compared to tapping AFMs. Staying out of contact preserves the tip apex ensuring that the diameter stays well below the optical wavelength. To be even more sensitive to the tip-sample force, and therefore gentler to the probe, we etch the wire from 50 μm wire instead of 250 μm wire. The reduction in mass significantly increases the quality factor of the tuning fork probe to 2000-5000 from 300-500. The quality factor varies significantly from probe to probe.

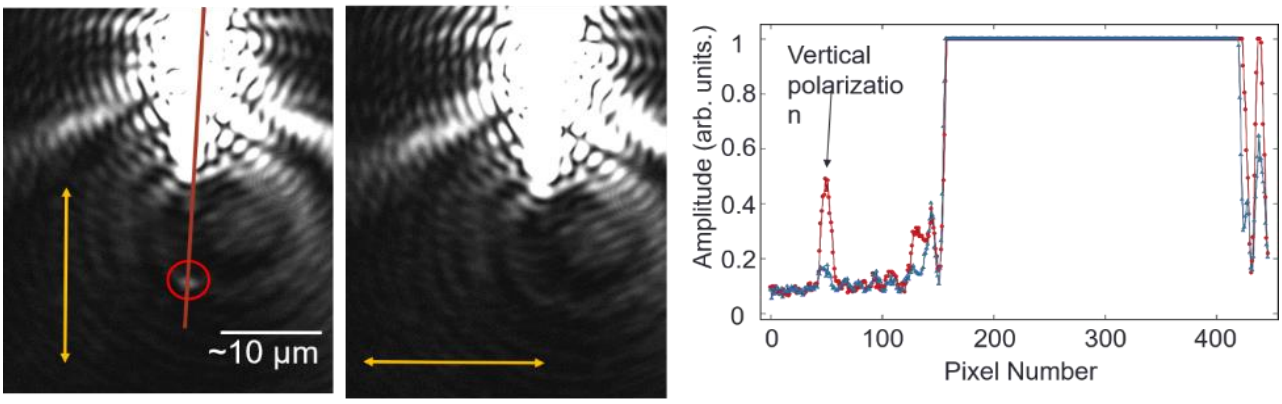

Figure 5.4 Microscope images of antenna showing focusing of surface plasmon polaritons

To make the etched gold wire into a plasmonic antenna we use a focused ion beam to cut a periodic grating into the wire approximately 10 µm away from the apex of the tip. This distance ensures that apex of the tip is well outside the 1 µm area of the laser spot and the region of saturated camera pixels. Background on scanning SPP antennas and our fabrication process can be found in [158]. Figure 5.4 shows two micrograph images of the plasmonic antenna with the laser shining at normal incidence on the grating. In Figure 5.4a, the polarization of the light is vertical (electric field parallel to the wire) while in b) the light is horizontal. We expect SPPs to be excited when the light is vertically polarized but not when it is horizontally polarized. Figure 5.4c shows traces of the intensity along the length of the wire. We see in both the micrographs and the line cuts that there is a bright spot at the apex of the tip when the light is vertically polarized due to the scattering of SPPs that have been confined to the apex of the antenna. This provides evidence that we can fabricate SPP antennas, couple to them, and attach them to tuning forks for scanning probe microscopy.

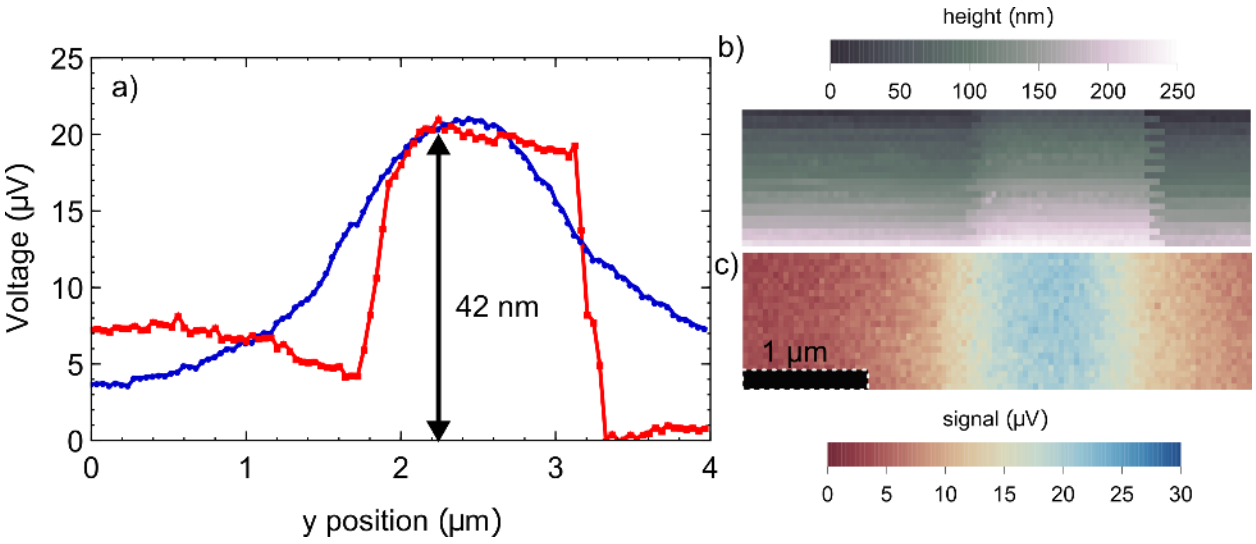

Figure 5.5 Near-field effects using shear-force feedback. a) Line plots showing the average of the line scans measured by the shear-force geometry near-field microscope. Blue is the average of the voltage scans referenced to the frequency of the tuning fork. Red is the average of the topography line scans. b) Height map of the topography of the YIG/Pt wire. c) 2D plot of the voltage at the frequency of the tuning fork oscillation. The scans were takeng perpendicular to the long axis of the sample.

To test the effectiveness of the shear-force geometry combined with the plasmonic antenna, we again measure the YIG/Pt wire. We measure the heating induced by the optical tip-sample interaction by applying a current density of 2.5×10^6 A/cm^2. The quality factor of this particular tuning fork is 4136. We note that in the shear-force geometry, we measure the change in amplitude, not the frequency, to feedback to keep the tip-surface separation constant. The ~50 nm side-to-side amplitude in this configuration is on the order of the apex size and does not provide any modulation of the signal. Thus, there are only two channels in this configuration: the topography and the signal modulated at the frequency of the optical chopper. To check that the signal is created by the probe itself, we use piezomotors to maximize the signal indicating that the laser is focused on the surface of the sample. Then the laser in moved in the z-direction and we observe a dip in the signal followed by a corresponding increase at a displacement of ~10 μm

where we expect the FIB-cut grating to be. We confirmed that the signal goes to zero when the tip is retracted.

Figure 5.5a and b show images of the topography and voltage signal taken using the shear-force scanning probe geometry. We note that over the course of the scan, the position of the tip drifts away from the surface by over 150 nm. The voltage signal however, does not have the corresponding reduction that we expect for near-field interactions that happen on the scale of ~10 nm or less. These two signals together can be explained by a weak tip-sample interaction in the transverse AFM geometry so that the tip is at least several tens of nanometers above the sample surface. In this case, the plasmonic waveguide cannot couple to the Pt surface in the near field, but still radiates into the far-field with a resolution that is higher than the blurred out far-field signal we see in Figure 5.2. It may be possible to improve this by a more carful choice of tuning fork oscillation amplitude although optimization would require simultaneous tuning of the laser position and feedback parameters.

Figure 5.5c shows the averaged lines scans of the topography and voltage. The peaks of the two signals line up and the largest voltage is when the tip is closest to the sample. We also find that there are no edge artifacts, supporting the idea that there was contact between the tip and wire in tapping mode but that the contact is eliminated in the shear geometry. The voltage signal is not sharply peaked, however, and the topography image is also not as sharp as it is in the tapping AFM geometry. Unfortunately, the tip crashed into the surface before we were able to confirm that there was also sensitivity to the YIG magnetic moment transduced through the LSSE. We expect that any magnetization sensitivity would have similar signal-to-noise ratio as the tapping mode geometry because the signal amplitude of the dc current image is similar to that of the tapping geometry.

In summary, experiments using the shear-force geometry successfully show that near-field scanning with a plasmonic antenna is possible without destroying the probe apex. However, the difficulty of the alignment and the fact that far-field background cannot be rejected by demodulation at the tuning fork resonance frequency conspire to make the shear-force geometry challenging. Further development of this geometry might improve on these problems by bringing the sample up to the tip, enabling alignment to the grating independently of the sample. Nevertheless, the ability to demodulate at the frequency of the tuning fork motivates returning to the tapping mode geometry. This time, however we use gold coated AFM cantilevers glued to the tuning fork to increase probe life-time.

5.4 Tapping mode AFM with directly illuminated gold-coated silicon cantilevers

In this section we study the geometry, shown in Figure 5.1c, of a gold-coated AFM cantilever glued to a tuning fork and illuminated at a 30° angle. The motivation for this approach was primarily to increase the tip lifetime. There are several reasons to expect that gold-coated Si tips will be more robust than pure gold wires: The Si substrate has a significantly higher yield stress than gold, reducing damage from bending. The cantilever's spring constant is significantly lower the quartz tuning fork, so if the tip crashes, the cantilever will bend before the tip breaks. Finally, the cantilever is very light, so that the quality factor of the tuning fork is near the value of a bare fork in air. The higher quality factor increases the force sensitivity so that there is less force needed to keep a constant tip-surface separation. The other benefit of using commercial AFM tips is that they are relatively inexpensive and reliably have a tip apex of 30 nm or less.

We illuminate the apex of the AFM probe by focusing light from a 0.42 NA long-working distance objective, as before. In this case, however, the objective is tilted 30-degrees with respect to the surface normal. The tilt gives more efficient optical coupling because the light

is not blocked by the side of the sample substrate and because it reduces background heating from light scattering within the sapphire substrate. To further improve optical access, we use AFM cantilevers with the tip at the end of the beam (OPUS 3xc-GG) so that it is less likely to be shadowed by the cantilever overhang.

The samples we use for the study are CoFeB (4 nm)/Hf(.3)/Pt(4) wires that are 2, 5, and 10 μm wide. These are the same samples used for demonstrating the capability to measure spin torque angles in [164], and further details of the fabrication can be found there. The samples are mounted such that the long axis is parallel to the optical beam. The electrical detection circuit is the same as in the prior two sections.

We first test the sensitivity of the AFM tip geometry to the magnetic moment of the CoFeB by taking scans after saturating the magnetization in opposite directions. The scans were done at zero field and the results are shown in Figure 5.6. We note immediately that the signal from the wire itself is much larger and less noisy than what we measured in the Figure 5.2. Figure 5.6a shows line scans of the raster-scanned images at right. We observe that for oppositely directed magnetizations we have opposite polarity signals with similar amplitude. The signal-to-noise ratio is sufficient to see the difference individual traces (joined plot markers), not just in the averaged line scans of the entire scan (thinner line with no plot markers).

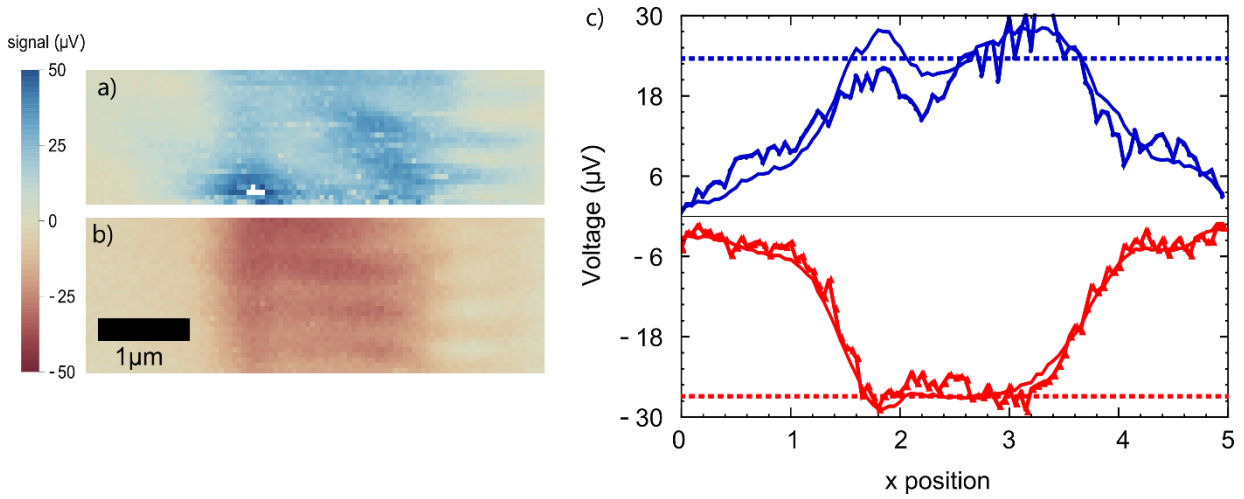

Figure 5.6 Scanning near-field TRANE image of oppositely directed magnetization in 2 μm wide CoFeB/Pt wires. a-b) 2D plots of the voltage measured at twice the frequency of the tuning fork. The scans are taken with the commercial AFM tip glued to the tuning fork and operating in tapping mode. c) Line traces of the 2D plots. Blue corresponds to the data in a) and red corresponds to the data in b). The solid lines without data points represent the average of all the scan lines and the thicker lines with data points are single line scans taken from the middle of the images. The dotted lines are the mean voltage when the tip is over the sample at ± magnetic saturation.

With sensitivity to magnetization established, we now turn to observations of domains in wider structures. We note that in wider samples, we expect the signal to be reduced by the ratio of the wire widths, however, the signal amplitude in the 2 μm wide wire is large enough that we have confidence that we can observe domains with oppositely oriented magnetic moments.

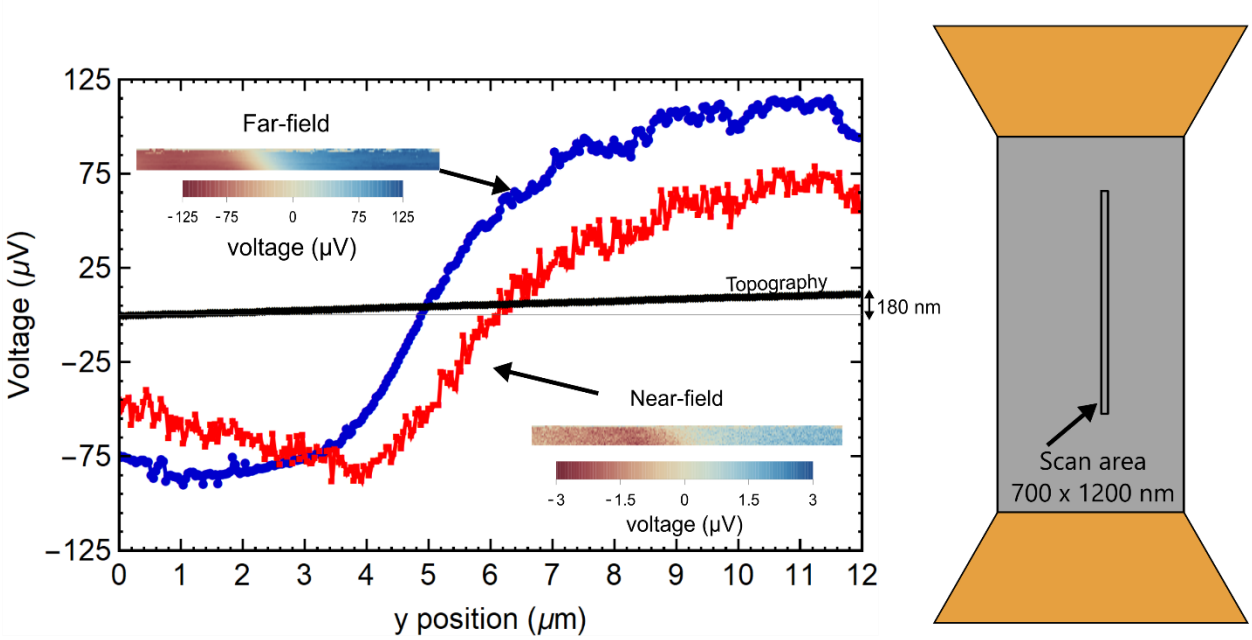

Figure 5.7 Observation of domain wall in 10 μm × 20 μm CoFeB/Pt bar with no near-field coupling. The blue line shows the "far-field" signal, the voltage from the sample that was modulated at the frequency of the optical chopper. The red line shows the "near-field" signal, the voltage modulated at twice the tuning fork frequency, multiplied 50 times so that it can be compared to the far-field signal. The insets show the unscaled 2D plots of the near and far-field. The schematic at right shows scale of the scanning area, depicted as a black outline, with respect to the CoFeB/Pt sample.

Figure 5.7 shows a line scan over a domain wall in a 10 μm wide CoFeB wire measured at the frequency of the focused light modulation. As expected, the extended point-spread-function of the focused light provides low resolution, however, the change in sign is consistent with the presence of a domain wall. In red, on the same plot is the voltage demodulated at the second harmonic of the tuning fork frequency multiplied 50×. The 2D images are inset. When we compare the two traces, it is apparent that the near-field signal does not have increased spatial resolution. We attribute this weak, low-resolution signal to a miss-alignment between the laser and the scanning tip, such that the tip only reflects the near-field light but does not enhance it.

The data in Figure 5.7 provides useful information about this scanning probe geometry even if it does not show the increase in spatial resolution that we set out to achieve. First of all, it demonstrates that the focused light in the 30-degree orientation is capable of detecting the local magnetization of magnetic domains with approximately 1-2 μm resolution. We are prevented from a better estimate of the resolution by a lack of features with known sizes. The data also show us that the background from reflections off the tip can be on the order of a few percent of the modulation-referenced signal, though the exact value depends on the specific sample. This suggests that during alignment of the laser the operator must be careful to check that the effect is not simply from reflections. This could be done, for instance, but confirming that the signal goes to zero sharply when the probe scans over an edge.

After improving the optical alignment and moving to a 5 μm wide wire, we were able to observe domains and enhanced resolution due to the tip. The sample was initialized into a multi-domain state using a permanent magnet but the scanning was done at zero magnetic field. Figure 5.8 shows the topography signal, voltage signal demodulated at the frequency of the light modulation (far-field), and the voltage signal demodulated at the 2^{nd} harmonic of the tuning fork frequency (near-field). The scan was taken over 5 hours and the three images (Figure 5.8 a-c) were acquired simultaneously during the scan. Individual line cuts taken in the scan direction across regions of varying contrast are shown below. We see from both the images and line scans that there are regions of different magnetization and these align to the location of the wire as seen in the topography. As in Figure 5.7, the far field signal is larger than the tuning fork referenced signal and has relatively low resolution. Unlike in Figure 5.7 however, the near-field signal shows a superior resolution, and shows features that correspond to the features in the far-field channel.

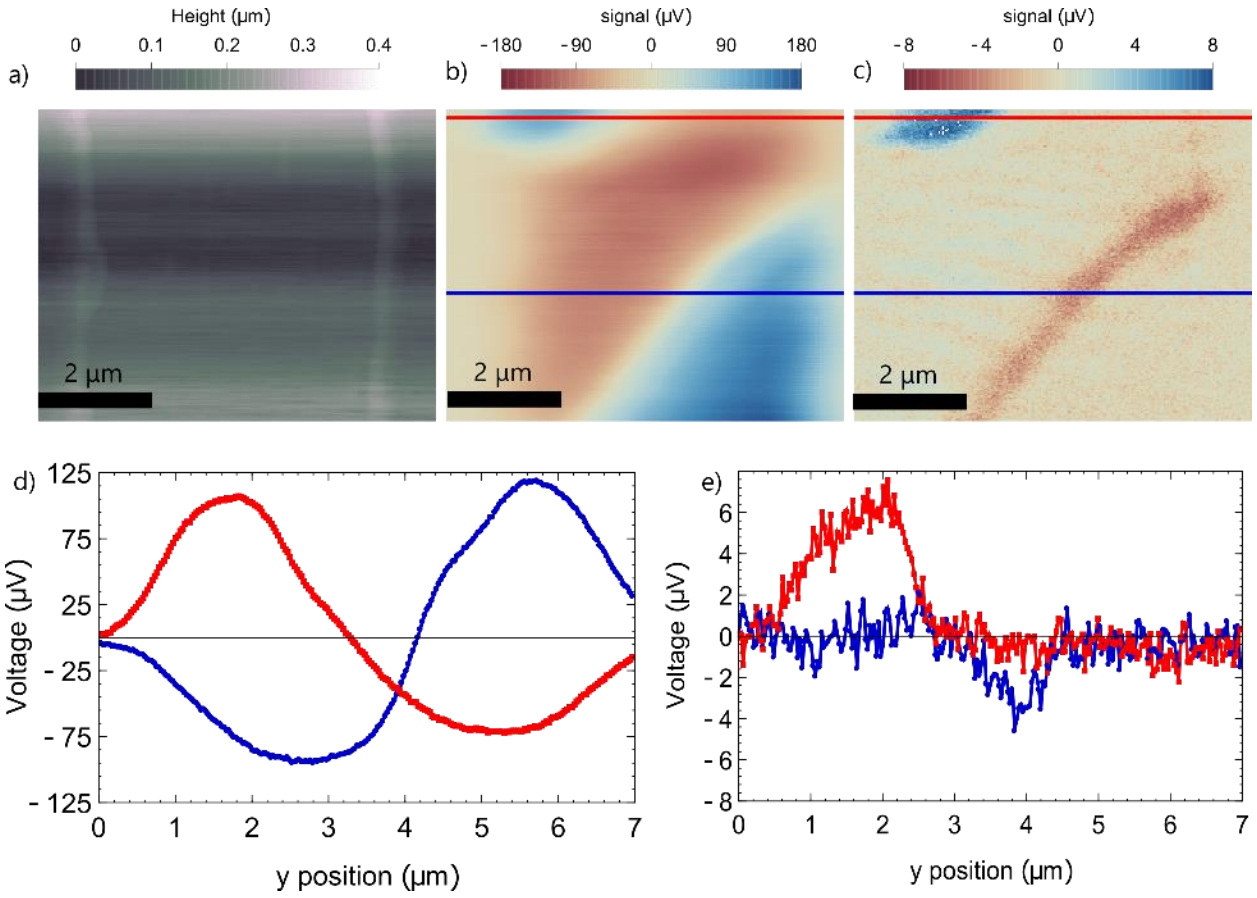

Figure 5.8 Images of magnetic texture in a 5 μm × 15 μm CoFeB/Pt bar. a) Topography image of the bar measured with AFM. b) 2D plot of the voltage demodulated at the optical chopper frequency. c) 2D plot of the voltage demodulated at twice the tuning fork frequency. d) Line cuts of b), the trace color corresponds to the line color in b). e) d) Line cuts of c), the trace color corresponds to the line color in c).

Comparing the far and near-field images more carefully, we note that the signal from the scanning tip drops to zero over most of the wire but does not do so in the signal from direct laser heating. TRANE only measures the component of the magnetization perpendicular to the wire channel. A magnetic moment pointed along the length of the wire would be zero and a moment at some angle oblique to the wire would have an amplitude less than the perpendicular case. Thus, we suggest that the image is not of oppositely aligned moments, but instead tilted in a more complicated fashion.

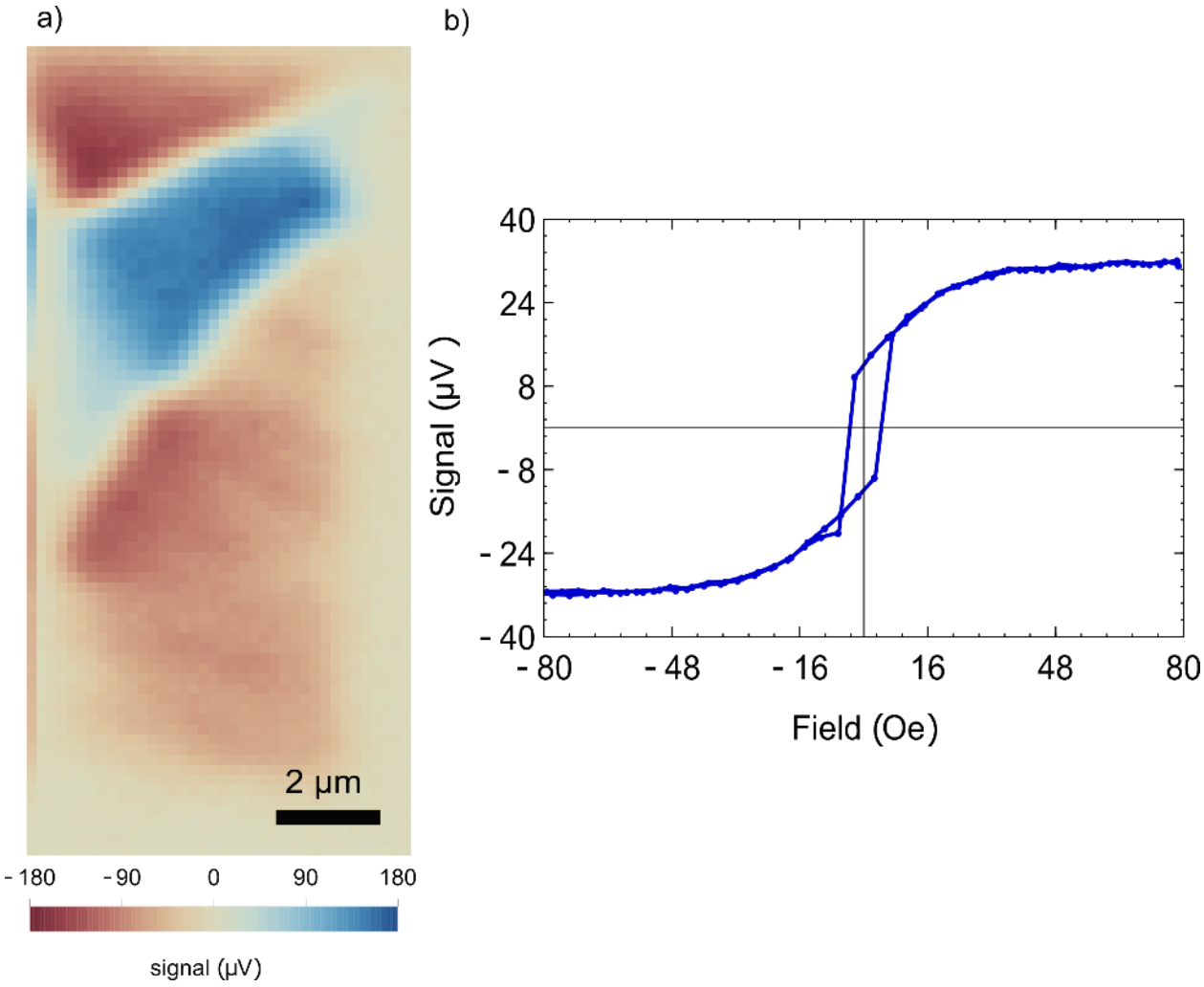

Figure 5.9 Analysis of magnetic texture in a 5 µm × 15 µm CoFeB/Pt. a) Image of a multi-domain magnetization state taken with the conventional TRANE microscope. b) Measurement of the magnetization perpendicular to the long axis of the wire as a function of external field. The external field was also oriented perpendicular to the long axis of the wire.

To examine the possibility of a more complicated, twisted magnetization state we look at the sample in the conventional, focused light TRANE microscope. Unfortunately, the magnetic state shown in Figure 5.8 was not stable and the magnetization reverted to a more uniform configuration before we could measure it with the far-field TRANE microscope. Figure 5.9 however, shows a separately created magnetic texture, imaged at zero magnetic field, that suggests a magnetic vortex. The fact that the magnetic film can be put in these smoothly varying

magnetization states is an indication of low anisotropy. This is consistent with the magnetization versus field measurement shown in Figure 5.9 in which the external field was applied perpendicular to the long axis of the wire but the coercive field was low and there the signal at remanence is much less than that at saturation.

5.4.1 Estimation of spatial resolution and sensitivity

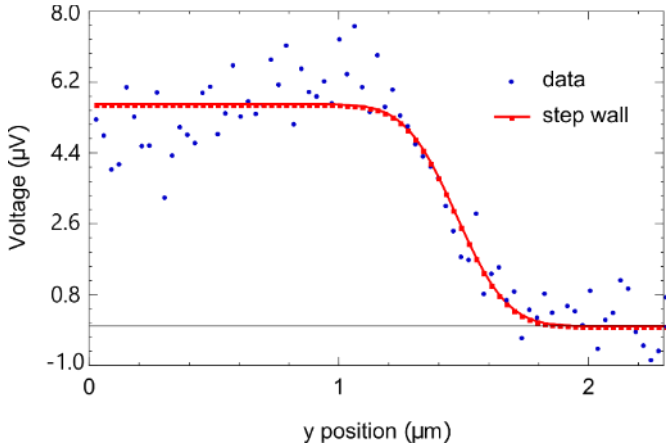

Figure 5.10 Fitting of domain wall edge and analysis of magnetic orientation

The greatly improved signal-to-noise ratio of the AFM cantilever geometry and data in Figure 5.6 and Figure 5.8 allow us to estimate the sensitivity and resolution of the near-field scanning probe signal. To estimate the sensitivity, we use the data of oppositely directed magnetization from Figure 5.6 and Eq. (3.7). The dotted lines in Figure 5.6 show the mean value between 2 and 3 μm at positive and negative saturation. To obtain the standard deviation, we take the standard deviation of the signal off the bar to get a measure of the uncorrelated noise. The time constant of the lock in measurements was 200 ms and so we calculate a sensitivity to the magnetization of 1.4°/√Hz. This is significantly less sensitive than what we have been able to achieve with the conventional TRANE setup, however, we note that this is an upper bound because the magnetic moment is not fully saturated at zero external field. In addition, there is

potential to optimize further by reducing the noise from background light, room vibrations, and sample drift.

To estimate the spatial resolution, we fit the line scan across the domain wall shown in Figure 5.8. We fit the sigmoid to $\frac{A}{2}(1-\mathrm{erf}\left(\frac{y-yo}{\sqrt{2}\delta}\right))$, the FWHM of the curve is given by $(2\sqrt{2\ln 2})\delta$. The fit, shown in Figure 5.10, yields a width of 376 nm. If the domain wall was much narrower than the probing thermal gradient than this would be the size of the gradient. However, unlike in Chapter 3, this is not a good assumption because the AFM tip is quoted as having a tip diameter of < 30 nm and domain walls, even in materials with high anisotropy, are typically not smaller than 10 nm. Moreover, in the CoFeB film, the ability to create a vortex wall indicates that the anisotropy is low and therefore that the domain walls will be wide because the domain wall size is proportional to the ratio of exchange stiffness and anisotropy. Thus, it is physically reasonable that the domain walls could be significantly larger than the point-spread-function of the AFM tip. Physically, it is unlikely that the tip was >100 nm given evidence from looking at SEM images of crashed tips and considering the fact that the near-field signal would likely be extremely small due to the small enhancement volume. There is also the possibility that the tip is simply blocking a portion of the surface. We think this is unlikely, however, because the magnitude of the tuning fork referenced signal is significantly larger than the signal measured in Figure 5.7 even though the resolution is improved. If a smaller area was blocked (thereby increasing resolution) the difference between the blocked and unblocked states would also be smaller (which would decrease the signal amplitude measured at the tuning fork frequency harmonic). On the other hand, it is reasonable that the domain wall is 300-400 nm wide. Thus, we conclude that the scanning near-field heating with an AFM tip has a resolution below the

diffraction limited optical spot and may be capable of imaging magnetization with a point spread function of <100 nm.

5.5 Conclusion and next steps

In summary, in this chapter we presented three different scanning probe geometries and used them to measure the magnetization and local current flow in microfabricated wires. We conclude that commercial gold-coated silicon AFM cantilevers provide the best results. We measure a sensitivity to the local magnetic moment of 1.4°/√Hz and estimate the effective point spread function is below 100 nm. Further development is needed, but the results presented here strongly suggest that near-field heating has the potential to enable time-domain imaging of magnetization with spatial resolution similar to magnetic force microscopy or scanning transmission x-ray microscopy.

To provide further evidence that we observe near-field heating, future work should measure the signal as a function of the incident polarization and systematically vary tip-surface distance. The test of the polarization dependence is relatively straightforward, although it requires a reworking of the current optical setup, so that when the waveplate changes it does not move the excitation optics. Measuring the signal versus relative tip height is more difficult because it would ideally be an experiment where the tip and laser are stationary and the sample height is changed; however, this is not possible with the current stages. An alternative is to measure approach curves with the laser at different fixed positions from the sample surface to 100 nm above the surface.

Once the near-field enhancement is firmly established, we need to improve the signal-to-noise ratio if this is going to be a practical measurement. There are a few ways that may increase the signal-to-noise ratio of the scanning probe system. For example, improving the detection

electronics and improving the sample impedance match would greatly improve the signal-to-noise ratio. In addition, cutting a plasmonic coupling grating into the commercial AFM tips may allow light to more efficiently couple into the scanning probe and reduce heating from the laser being directly at the surface. A geometry similar to this has been reported in which modified commercial AFM cantilevers were used to heat Si [146]. In addition, it may be possible to increase the signal-to-noise ratio by adjusting the tuning fork oscillation amplitude and using higher harmonics [160], however, this needs to be studied more systematically. Finally, any of the standard improvements to the stability of a scanning probe system will greatly reduce the noise. These improvements could include adding a vibration isolating enclosure, implementing temperature control, using more flexible cables connecting to the scanning stages to reduce eternal forces, and using higher frequency tuning forks. Longer-term, tuning fork AFM is well suited to vacuum or low temperature measurements, which would reduce the mechanical noise floor and open up further experiments. This would, of course, be a significant investment and we may not be able to neglect the thermal expansion of the optically heated tip.

5.5.1 Funding acknowledgements

This research was supported by the U.S. Air Force Office of Scientific Research, under Contract No. FA9550-14-1-0243. This work made use of the Cornell Center for Materials Research Shared Facilities which are supported through the NSF MRSEC program (DMR-1719875) and was performed in part at Cornell NanoScale Facility, an NNCI member supported by NSF Grant ECCS-1542081.

CHAPTER 6

EXPERIMENTAL DETAILS OF THE NEAR-FIELD SCANNING MAGNETO-THERMAL MICROSCOPE

6.1 Introduction

As discussed in Chapter 3, the spatial resolution of TRANE and TRLSSE measurements is determined by the area of the heated surface and can, in principle, reach nanometer length scales. To heat such deeply sub-wavelength areas we chose a near-field scanning optical microscope (NSOM) configuration because it enables localization of light to areas well below the far-field diffraction limit but still has the advantage of using picosecond pulsed sources [165,166]. In particular, we adapt the approach used in heat-assisted magnetic recording (HAMR) and tip-enhanced Raman spectroscopy (TERS). Both HAMR and TERS rely on using sharp plasmonic tips to enhance electric field through a combination of the so called 'lighting rod' effect and plasmonic enhancement.

Conceptually, magneto-thermal microscopy is very similar to HAMR since both applications require fast, nanoscale heating. Functionally however, the microscope has more in common with TERS microscopes. In HAMR, a magnetic recording medium is heated above, or close to, its Curie temperature to reduce the field magnitude required to write a bit of information. Publications from the early stages of this work demonstrated that that near-field optical heating could heat a material by hundreds of degrees in a 20 nm region [157]. In addition, it was shown that the exact spatial pattern and magnitude of the heating depends closely on the plasmonic antenna and the material being heated [88]. Ultimately, HAMR technologies are engineered around an optimized complete system so they lose the generality desirable for magneto-thermal microscopy. We can get similar near-field field enhancement from etched gold

wires and gold coated AFM tips. In TERS measurements for example, it has been shown that gold coated tips can act as plasmonic waveguides in which the optical enhancement is sufficient to cause nonlinear effects, including heating [146,149].

In this chapter we describe the design and operation of a custom NSOM used for magneto-thermal microscopy. The geometry used here is an apertureless NSOM which combines a tuning fork atomic force microscope (AFM) a with sharp gold tip. The geometry, shown in Figure 6.1, has three parts: the quartz tuning fork AFM, the optical elements, and the electrical measurement circuit. The electrical measurement circuit is identical to the one used in the far-field setup. The primary difference being that the signal synchronization is done via the phase-locked loop (PLL) control electronics rather than through a data acquisition card. The other components will be discussed in more detail in the following sections.

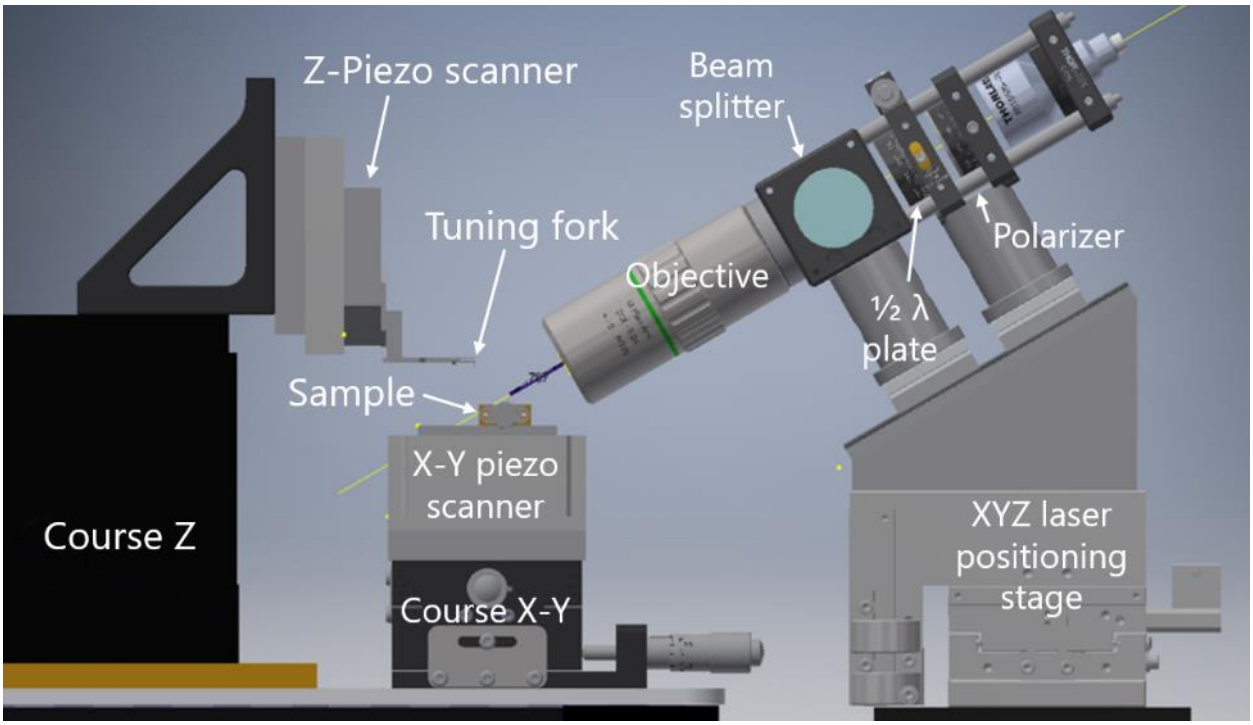

Figure 6.1 Illustration of the near-field scanning optical microscope used for magneto-thermal microscopy.

6.2 Quartz tuning fork atomic force microscope

In this work, we use a quartz tuning fork to scan a sharp metal tip above the sample and measure the topography. Quartz-based tuning fork AFMs have an advantage over Si-cantilever AFMs in that they do not require a laser that could scatter and produce artifacts and that it is straight-forward to customize the probe because it is simply glued to the fork. Our AFM consists of a commercial quartz tuning fork with a sharp tip attached which acts as the scanning probe; a phase-locked loop (PLL), to drive the tuning fork at resonance; a proportional-integral (PI) controller [167], to control the tip height above the surface; and the scanning stages, to scan the sample and adjust the tip-sample distance.

The piezoelectric quartz tuning fork is the heart of the scanning probe system. Here, we use 32.768 kHz oscillators (Raltron, R26-32.768-12.5), removed from the vacuum can. Each tuning fork has 2 square tines with aluminum electrodes that excite a mechanical scissor-mode oscillation. The electrical behavior of the tuning fork is described by a Butterworth-van Dyke circuit shown in Figure 6.2 [168–171] where the reactive elements are related to displacement of the tines by the piezoelectric coefficient, ς with units of C/m. The current flowing through the fork is given by, $I = \varsigma \frac{\mathrm{d}x}{\mathrm{d}t}$, so that on resonance the current passing through the tuning fork increases dramatically. The quality factor of the tuning fork is high, typically > 5000 in air, so that by measuring the current flowing through the fork we can detect changes in the resonance of a few Hz. By monitoring the resonance, we can measure the force applied to the oscillator when it is brought close to the surface of the sample.

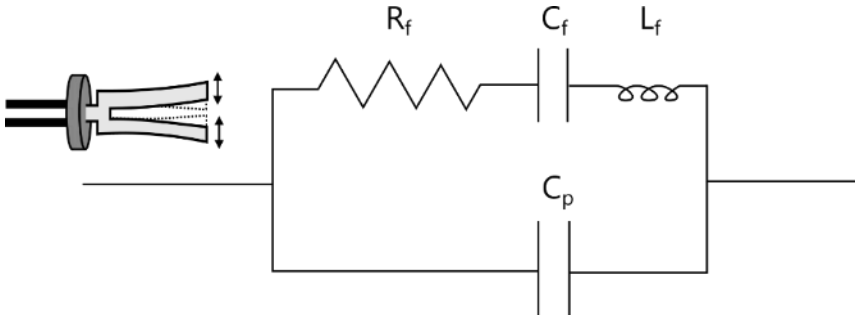

Figure 6.2 Circuit model for a quartz-tuning fork. The piezoelectric oscillator can be described by a characteristic capacitance, inductance, and resistance: C_f, L_f, and R_f. There is also a parasitic capacitance, C_p, that comes from the electrical traces on the circuit board and the tuning fork packaging.

The fundamental limit on the sensitivity of the tuning fork at room temperature is the thermal motion of the tuning fork. It is possible to calculate the noise power spectrum, S_F (units of N/√Hz), by knowing the quality factor of the resonator, Q, the fundamental frequency, f_o, the temperature, T, and the rms noise due to thermal motion of the tuning fork, x_{rms} [172]

$$S_f^{1/2} = \sqrt{\frac{2}{\pi f_o Q}} \frac{k_b T}{x_{rms}} \tag{6.1}$$

For a quartz tuning fork, not limited by electrical noise, the sensitivity to force can be less than a piconewton [172,173]. The sensitivity goes down when the symmetry of the tuning fork is broken by gluing a tip to one tine but it can still have sufficiently high Q to measure a few piconewton forces if the quality factor of the tip stays above 1000 [174,175]. This force sensitivity is required when using the etch gold wire in tapping mode so that tip does not get bent. The exact force required to bend the gold tuning fork is difficult to calculate and the yield strength for nanoscale gold is not well known. However for a yield strength of 500×10^8 Pa [176,177] a 30 nm diameter tip would bend with 35 μN. The actual sensitivity must be well below this to ensure the integrity of the tip apex during hours of scanning.

To characterize the force sensitivity and tip-surface interaction, we measure the vibration of the tuning fork as a function of tip height. The curve informs us of the force between the tip and the surface; whether it is attractive or repulsive and how long range it is. The force curve also gives a measurement of the sensitivity of the scanning probe feedback. In this work, we use force-curves to determine if a scanning probe is sufficiently sensitive to the surface. More detailed interpretation is possible, but beyond the scope of this work. Further information can be found in the literature [178,179].

We performed force curves for the three different scanning probe geometries shown in Figure 5.1, beginning with tapping mode using an etched gold wire (the case of Figure 5.1a). Figure 6.3 shows two sets of approach curves corresponding to two tuning fork probes. Each probe tip was made from a 50 μm diameter wire electrochemically etched to a point <100 nm. Tuning fork A had a quality factor of 657 and tuning fork B had a quality factor of 2384. The difference in Q between A and B is most likely due to differences in attaching the gold wires to the tuning forks. The curves show the change in frequency and the change in amplitude over the course of nine approaches. We show every other curve measured for clarity. For tuning fork A, we find that the lower Q leads to a noisier trace and a lack of sensitivity. As a result, each successive curve gets closer to the surface as the tip gets gradually destroyed. We confirm this result by imaging the tip in the SEM and find that the tip is indeed flattened. Tuning fork B tells a different story. By virtue of the much higher Q, successive approaches result in curves that consistently touch down at the same height. There is still significant variation between curves of where the tip starts to retract. However, it is telling that surface found by each curve drifts rather than marching closer to the surface. Even after an hour of scanning the tip over a sample we find the tip is still sharp (Figure 6.3f).

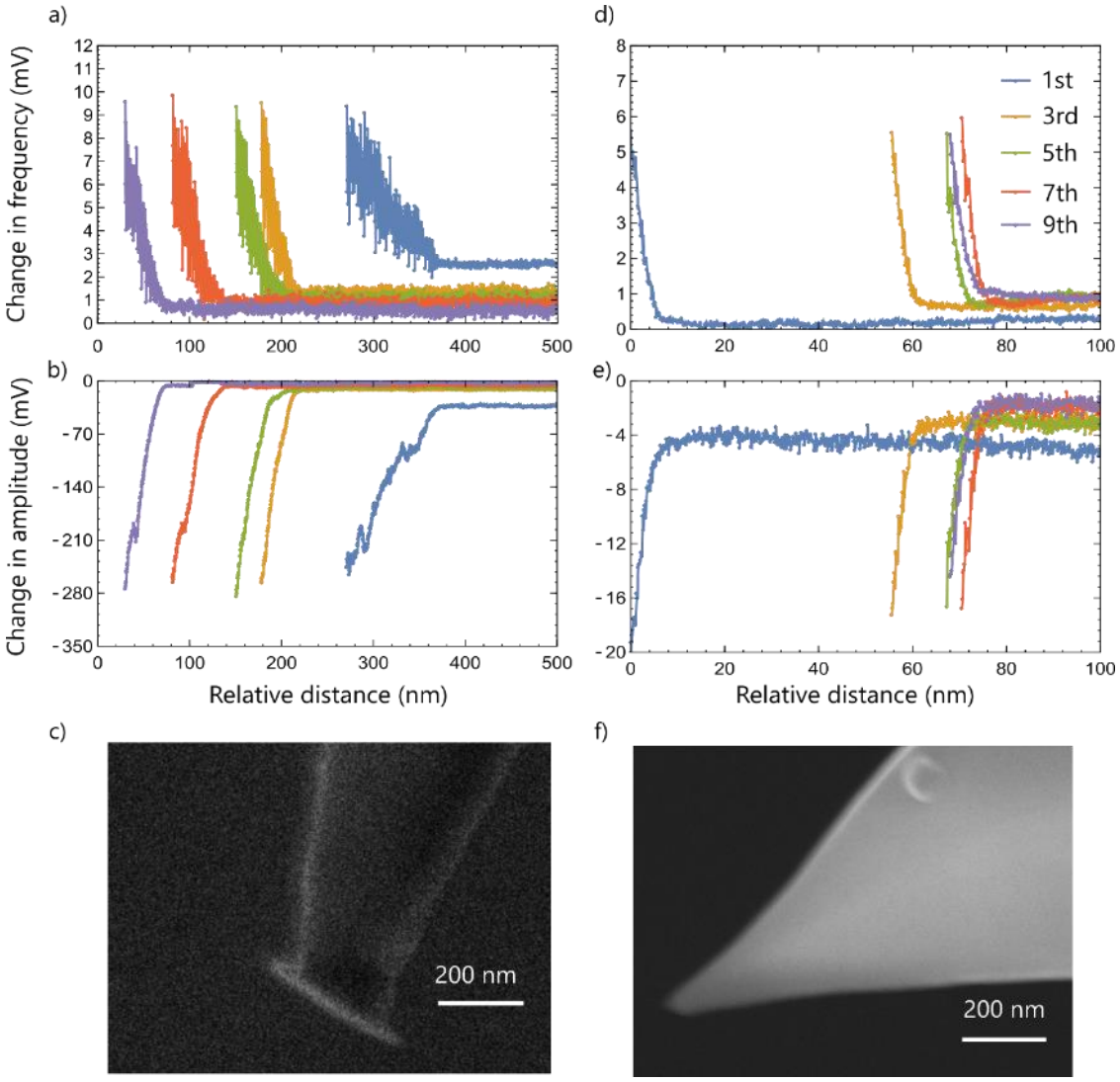

Figure 6.3 Tuning fork frequency and amplitude change versus distance for the etched gold wire tip in the tapping geometry. The left and right columns show data from tuning forks A (Q = 657) and B (Q = 2384) respectively. a-d) Show the change in frequency and amplitude of the of the tuning fork as a function of distance. In each panel the distance is relative to the closest distance measured. Panels c) and f) of the figure show SEM images of scanning tips A and B respectively after the approaches and, for B, an hour of scanning.

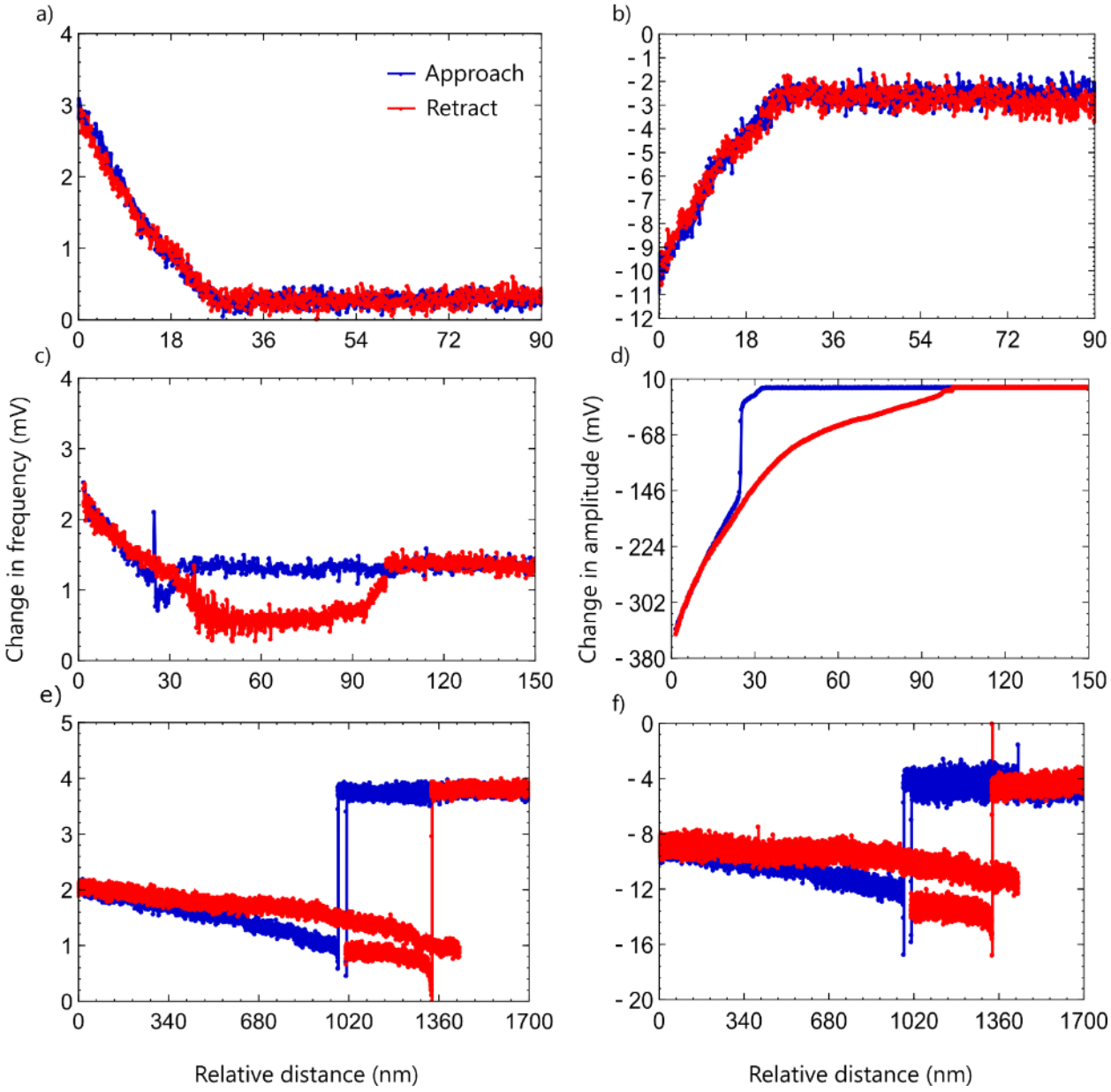

Figure 6.4 Tuning fork frequency and amplitude change versus distance for gold coated Si cantilevers in the tapping geometry for three different probes. The three probes were differentiated by the length that extended past the end of the tuning fork: a-b) short cantilever, c-d) intermediate length, e-f) long cantilever. In each case the offsets have been removed to enable comparison.

Next, we measure the frequency-distance curves of the scanning probes made by gluing gold coated Si AFM cantilevers to a tuning fork and operating in the tapping geometry (Figure 5.1c). For all of the tuning forks measured, the quality factor was >2000, however, we found that

the distance the tuning fork extended from the end of the tuning fork played a significant role in tip-surface interaction. We were not able to measure the exact lengths of the cantilevers however the difference was sufficient that we could distinguish between them in a 30x magnification stereoscope. Figure 6.4 show three sets of curves for the approach and retraction of increasingly long cantilevers. For the case of the shortest cantilever, in which the tip of the cantilever was very nearly aligned to the end of the tuning fork, we measure an approach and retraction curve that looks very similar to the high-Q tapping mode etched wire probe. There is a linear response right after contact and the approach and retraction overlap without hysteresis.

For the probe that sticks out a little further, we estimate ~200 μm, we observe a short region of snap-in and that, when retracted, the tip feels an attractive force for 60 nm (see Figure 6.4c,d). The snap-in and attraction is particularly pronounced in the amplitude of the tuning fork oscillation. This behavior can be explained by the Si cantilever bending independently of the tuning fork when it is close to the surface and getting stuck in a thin water layer on the surface [180] The different regions are shown schematically in Figure 6.5. Despite the hysteretic behavior, the curves were reproducible for 10 approach and retract cycles and good scans could be obtained in the contact regime

Snap-in and long-range attraction are even more pronounced for cantilevers that protrude further from the tuning fork. We show an example in Figure 6.4e,f. The figure shows two different approach and retraction scans because the scan range had to extend over a micron to capture the behavior. In this case, the snap in effect is strong enough that once the cantilever bends downward, the sensitivity is greatly reduced and the tip does not contact with the surface even after a micron of further approach. Compounding the problem of low sensitivity, the curves are also not very reproducible and this tip was unusable for imaging.

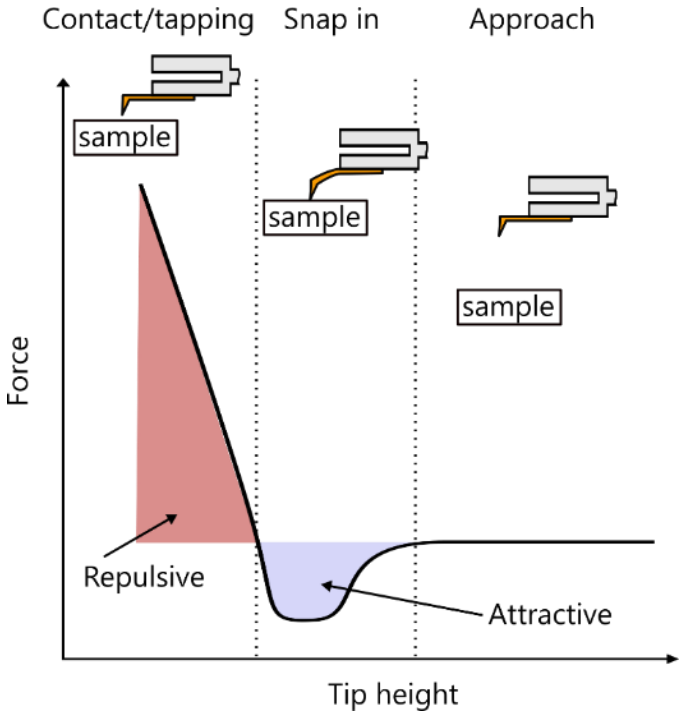

Figure 6.5 Representative illustration of the force curve and likely AFM cantilever behavior. In the attractive region, the cantilever protruding from the fork bends down towards the sample, the measured width of the attractive region is related to the length of the tuning fork sticking out from the fork and the spring constant.

Shear-mode AFM with an etched gold tip presents a quite different case from tapping mode. In the shear mode configuration, as the tip is brought close to the sample it experiences damping due to tip-sample interactions. While the exact nature of these interactions is not well understood [162,181,182], we can still use them to control the distance between the scanning probe and the surface. As in tapping mode, when the tuning fork feels the force from the surface, there is a change in both the frequency and amplitude. In the shear case, however, the amplitude is the more sensitive (see Figure 6.6.) In shear mode there is not an attractive region and it is hard to identify a 'contact' region, making it essential to determine the appropriate amplitude set point to get clean scans. If set too low, the tip will drift away from the surface; if set too high, the

tip will crash, resulting in unpredictable behavior. An example of an incorrectly set value of the feedback is shown in Figure 6.6c-d.

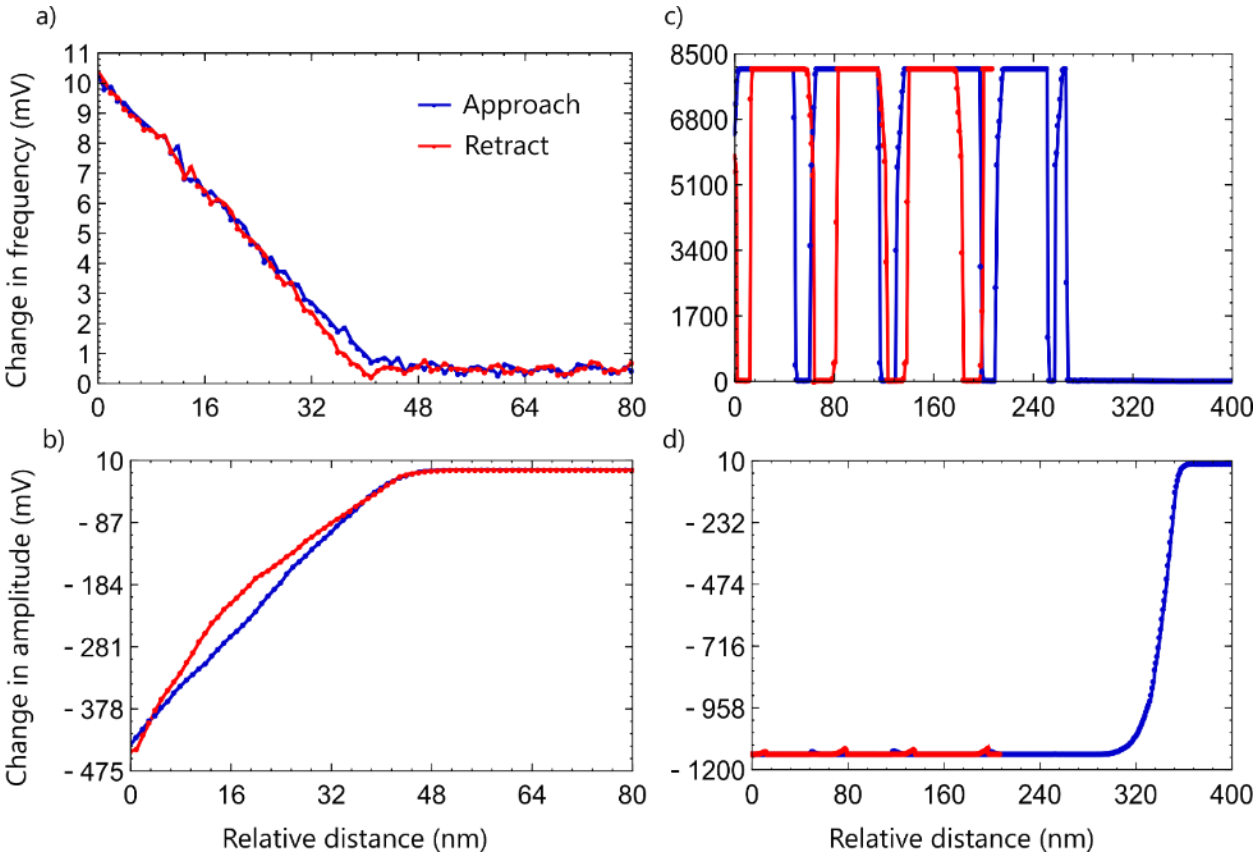

Figure 6.6 Tuning fork frequency and amplitude change versus distance for the etched gold wire in the shear force geometry for two different probes. Frames a-b) show a clean approach curve while c-d) show a curve with an incorrectly chosen setpoint.

6.3 Optical excitation of near-field scanning tip

We show the optical path used to illuminate the scanning probe in Figure 6.7. A Ti:Sapphire laser (Coherent Mira 900) generates 3 ps pulses at 780 nm which are coupled into the a polarization maintaining single mode fiber. Before the fiber, the light passes through a Faraday isolator, half-waveplate, electrooptical modulator (EOM), mechanical chopper, polarizer, and focusing lens. The EOM can be used as a pulse picker to reduce the repetition rate of the laser, although all the data presented in this dissertation were taken using the 76 MHz

repetition rate of the laser. After the light emerges from the fiber, it is collimated and sent through another polarizer and waveplate to ensure that the light is well polarized. We then focus the laser onto the scanning probe using a microscope objective with a 20 mm working distance and 0.42 NA. A beam expander and camera are used to create a microscope (boxed area in Figure 6.7) to help with alignment of the laser, tip, and sample.

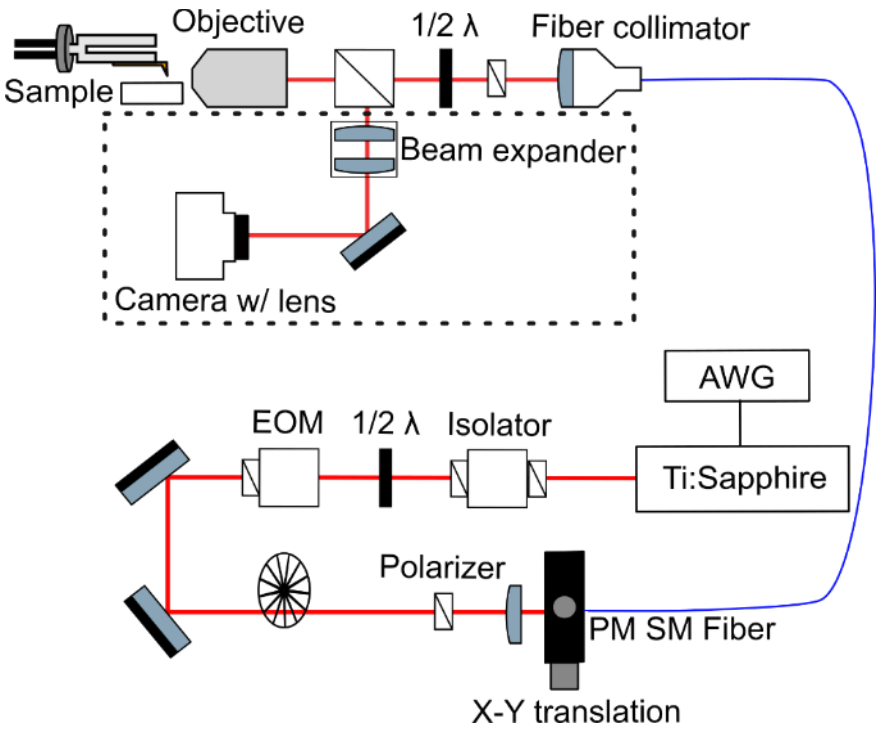

Figure 6.7 Schematic of the optical path used in the scanning probe microscope. EOM is the electrooptical modulator. The dashed boxed area is the optical microscope used to image the tip and sample through the objective. The objective, beam splitter, half-waveplate, polarizer, and fiber collimator are mounted on a xyz – translation stage at an angle of 30° to the optical table as shown in Figure 6.8.

The objective creates a 930 nm laser spot that must be carefully aligned to the scanning tip. This can be challenging because the angle of the microscope objective makes alignment the laser and sample tip non-intuitive. Figure 6.8 shows an illustration of the relation between the objective, tip, and image plane seen in the camera and an example of the camera image. The

microscope objective is on an xyz stage (as shown in Figure 6.1), that is used to focus the image and laser spot. In practice, it is straightforward to use the stage to focus the image of the scanning tip on the camera, however there is only one location that will also be the focus for the laser. To ensure the two coincide, we first mark the location of the laser spot on the camera image, then we block the laser and bring the tip into focus under the mark. Finer alignment can be made at the surface of the sample by maximizing the electrical signal demodulated at the frequency of the optical chopper.

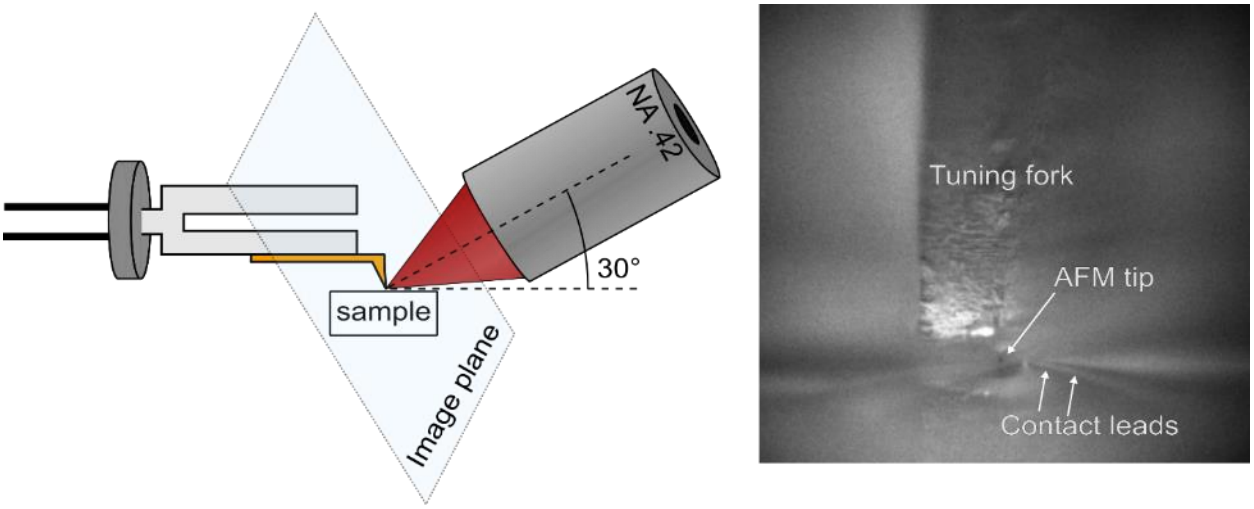

Figure 6.8 Optical imaging geometry. Left, schematic representation of the aligment between the objective, scanning probe, and sample. The plane imaged by the microscope objective is tilted with respect to the sample. Right, camera image of the tip near the surface of a sample.

6.4 Procedure for making scanning probe tips

6.4.1 Etched gold wire probes: shear mode and tapping mode

Here we describe the electrochemical etching procedure used to make the shear and tapping mode gold wire tips. We begin with 0.05 mm, 99.995% gold wire (Alfa Aesar), which we cut to lengths of approximately 3 inches, place on a ceramic sheet, and anneal in air at 800° C

for 8 hours to increase the grain size [183,184]. We tried to anneal the wire by hanging it from a W bar, this was unsuccessful because the W oxidized to bright yellow WO_3. After annealing, we etch the wire to a sharp point using 50/50 HCl/absolute ethanol. Finally, we inspect it using SEM. The etching procedure below is an updated version based on the technique developed by Jonathan Karsch [158]. In J. Karsch's work, the etching procedure was based in 250 μm diameter wires. Here, we use 50 μm diameter wires to reduce the mass on the tuning fork and increase the quality factor and force sensitivity. The thinner wire requires a modified procedure. The most relevant background for the process below can be found in references [185–187]. There are numerous other papers on making STM tips using a variety of different etching techniques that are beyond the scope of this work but which may be of interest to those generally interested in making STM tips [188–197].

The etched wire is the result of an electrochemical reaction in an HCl ethanol solution in which Au reacts with Cl to make soluble $AuCl_4$ through one of three reactions [186,198,199].

$$Au + 4Cl^- \rightarrow AuCl_4^- + 3e^- \qquad E = 1.002\ V$$

$$Au + 2Cl^- \rightarrow AuCl_2^- + e^- \qquad E = 1.154\ V$$

$$AuCl_2^- + 2Cl^- \rightarrow AuCl_4^- + 2e^- \qquad E = 0.926\ V$$

The etch occurs at the solution-air interface and self terminates when the wire below the surface falls off breaking the circuit. The standard electrochemical potentials listed above are not the potentials applied during our etching however the current versus voltage traced we measure are qualitatively similar to those shown in [198].

Table 3 Materials and equipment used for electrochemical etching

Current source, voltmeter, ammeter	A Keithley 2400 works well for this, but you just need ~0.1 V precision and the ability to supply almost an amp. To monitor the etch, it is helpful to be able to plot the current and voltage in real time.
Gold wire	99.995% pure alfa asar. It is worth noting that a former Raschke group member, Samuel Berweger, suggest different brands may etch differently.
Mini grabber	
Alligator clip	The kind without the teeth
Platinum wire	The platinum wire should be made into a ring ~2 inches in diameter and include a piece that sticks out to hold and provide electrical connection. The exact diameter does not matter much
Glass dish	
HCl/Etoh	50/50 by volume 36.5%-38% HCl/Absolute ethanol
Ring stands with clamps and posts	See Figure 6.9
Water and pipette	

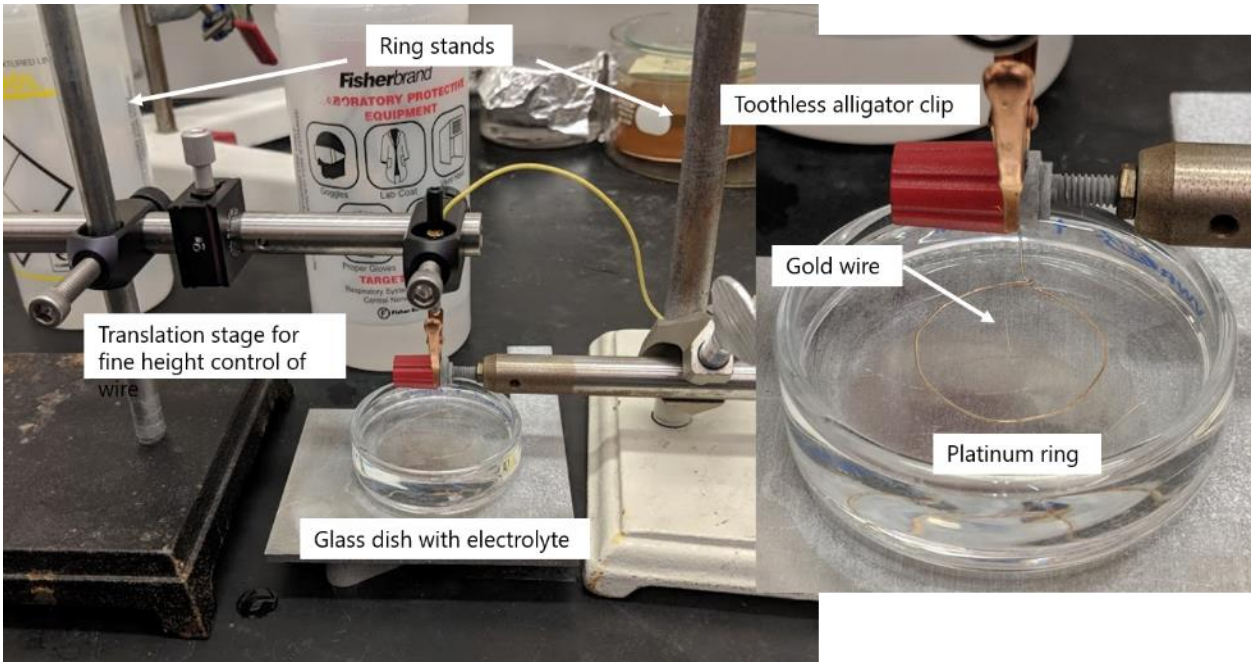

Figure 6.9 Electrochemical etching setup

- Anneal wire at 800° C for 8 hours. The Vulcan 3-550 box furnace was used for this work.
- Assemble the etching apparatus in the vented hood. The platinum ring should be fully submerged below the surface of the acid.
- Clip the wire as straight up and down as possible and lower into the acid mixture. The bottom of the wire should be below the level of the ring, about 3-5 mm below the surface.
- Electrically connect the alligator clip holding the wire to the positive terminal and the Pt ring to the negative terminal.
- Apply 1.9 V for 30 seconds and 2.1 V until the current drops to zero. This was done with a Keithley 2400 controlled via labview. The output with turned off when the current reached 0.005 mA.
- Raise the wire up and take it from the alligator clip with tweezers. Gently rinse with water using a few drops from the pipette.

- Glue or tape the unetched side to a piece of wafer or glass slide so that the wire is suspended above the surface of the box.
- Repeat the above steps to make more tips, then clean up.
- Inspect the wires in a SEM to confirm that the tips are < 50 nm in diameter. Compare the morphology of the tips to the voltage and current profiles measured during the etch and look for trends.

During the etch, we monitor the voltage and current as a function of time. Monitoring the current is particularly important for knowing when to stop the etch, how long the etch took to complete, and if the etch finished before the higher voltage was applied, as sometimes happens. In general, tips that had similar voltage and current time traces should be similar to one another.

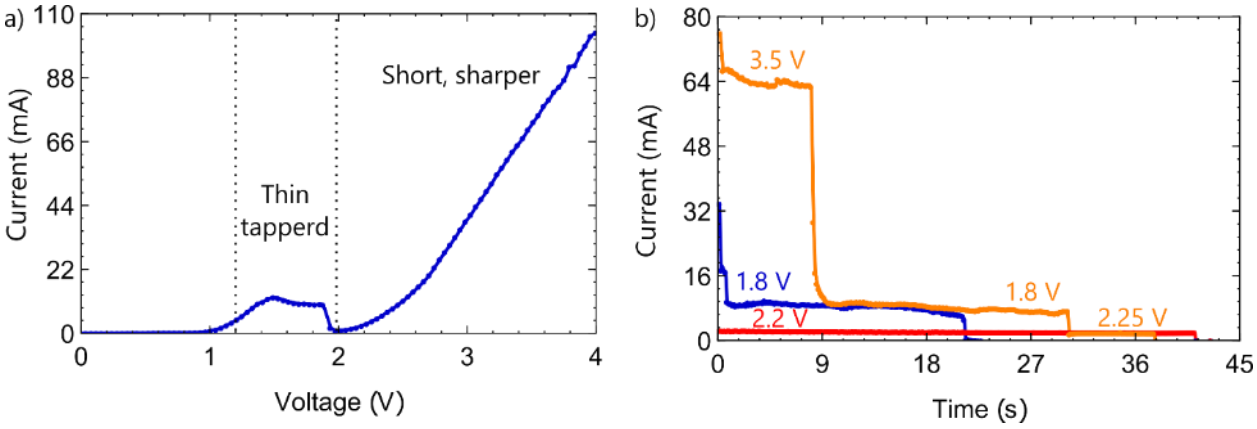

Figure 6.10 Transport measurements characterizing the etching of gold wires. Part a) shows a typical current vs. voltage measurement taken using the Keithley 2400. The dashed line demark regions that we found produce different tip shapes. b) Three current traces measured during the etching of 50 μm diameter gold wires. The red curve was and etch to completion with a applied voltage of 2.2 V and the blue curve was etched to completion using 1.8 V. The yellow curve was a three step etch. The etch self-terminated when the current went to zero.

We attach the wire to the tuning fork by gluing it, either before or after the etching process. The shear mode tips used in this work were glued before the etch and the tapping mode

tips were glued after the etch. In both cases the tuning fork is held in a pin vise, a small amount of glue (Loctite 416) is applied with a thin wire, and the gold wire is placed gently onto the glue. The glue, which was suggested by Mad City Labs, and has a fast setting time and a low viscosity making it easy to work with. Gluing the wire to the tuning fork before the etch reduces the chance of bending the etched tip because it reduced the number of times the sharpened wire has to be handled directly. Unfortunately, the chlorine gas emitted as a product of the etch corrodes the aluminum electrodes so this method can only be used with short etch times. Gluing the wire to the tuning fork after etching enables faster fabrication and inspection. The downside is that it is hard to orient the front of the tip so that it faces the same direction as the front of the tuning fork, this is particularly important if the gratings are cut in the wire before gluing to the fork.

During the development of the scanning probe fabrication procedure we found, in the literature and through experience, a few changes that could improve the electrochemical etching process. We would like to improve the process because it makes wires with a tip apex of < 50 nm only about 50% of the time. The yield is reduced further when the tips are selected for having a smooth surface and tapered cone length of 10 μm.

Of the different etching variables, we explored the relationship between the etching potential and tip morphology the most, finding two general trends that can be related to the current-voltage dependence. First, applying voltage below the 2V drop off in the current yields small cone angles and smooth sides however the tip apex is never less than 100 nm. Applying voltages of greater than 2 V produces wider cone angles and rougher sides, but the apexes of the tips are frequently below 100 nm. Observing these trends lead us to use two etch potentials. The first step is timed and uses a 1.9 V potential that makes a smooth taper, the second step is a 2.1 V

potential that is applied until the etch is complete and the wire below the surface falls off. The purpose of the second step is to 'sharpen' the tip and produce a final result that is < 50 nm.

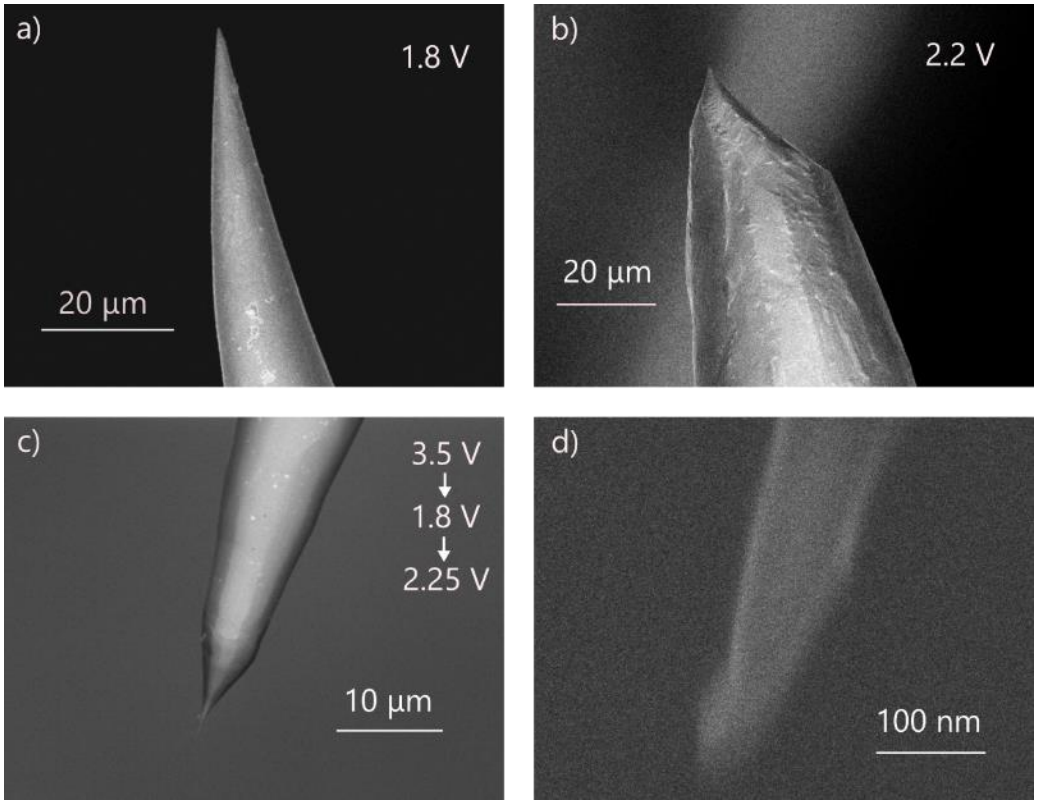

Figure 6.11 SEM images showing the different tip morphologies obtained from different etch voltages. The tips shown in this image correspond to the etch traces shown in Figure 6.10b. a) A tip etched to completion with 1.8 V showing a smooth, long taper. b) A tip etched to completion with 2.2 V showing a less conical shape but sharper tip. c) A tip that was etched using three different voltages. d) The same tip as c) but at higher magnification.

It is important to shut off the current as soon as possible after the etch ends because the tip can continue to etch after the submerged part of the wire falls off. The current source for the etched tips in this work was a Keithley 2400 source meter controlled with Labview. The Keithley output can only be controlled on a time scale of roughly 1 ms, with the exact time depending on the filter settings. It is possible that a sharper tip could be created by using a faster differentiator

circuit that can provide cutoff times faster than 100 μs. We did not test this, however more information about the influence of switching times can be found in references [188,191,195,197].

In addition to the etching voltage, we expect that the yield can be increased by adjusting the annealing, mechanical stability and electrolyte. Annealed wire produces smoother sides than unannealed but they can be faceted, leaving sharp edges that are not ideal for surface plasmon propagation. This may be improved with different annealing conditions [176]. The mechanical stability of the etching apparatus also effects the reproducibility of the wires because the etch happens at the liquid surface making it very sensitive to vibrations and variations in cross section from angling the wire. These problems can be mitigated by shielding the airflow from the hood vent that vibrates the wire and improving the control of the wire alignment to ensure the wire goes straight into the acid mixture. Finally, the electrolyte can also have a large effect on the etch however we have not tested solutions of different acid concentration or types. One reference from the literature suggests that $CaCl_2$ may be a good alternative [194].

6.4.2 Attaching gold-coated silicon cantilever to tuning fork

In addition to the etched gold wire, we also tested commercial, Si AFM tips coated with 70 nm of Au. The cantilevers we tested (OPUS tips 3XC- GG, Figure 6.12) had the tip at the end of the cantilever to improve optical access. Each piece that would go into a traditional AFM holder actually had three cantilevers of different lengths attached to the same piece of bulk Si that we refer to as the "shard". To use the cantilevers in our tuning fork AFM we must attach them to the tuning fork itself after removing them from the shard. It is important that only the cantilevers are attached to the tuning fork because shard is heavy enough to prevent the tuning fork from vibrating. Figure 6.13 shows the process for attaching an AFM cantilever to a tuning fork and the final product.

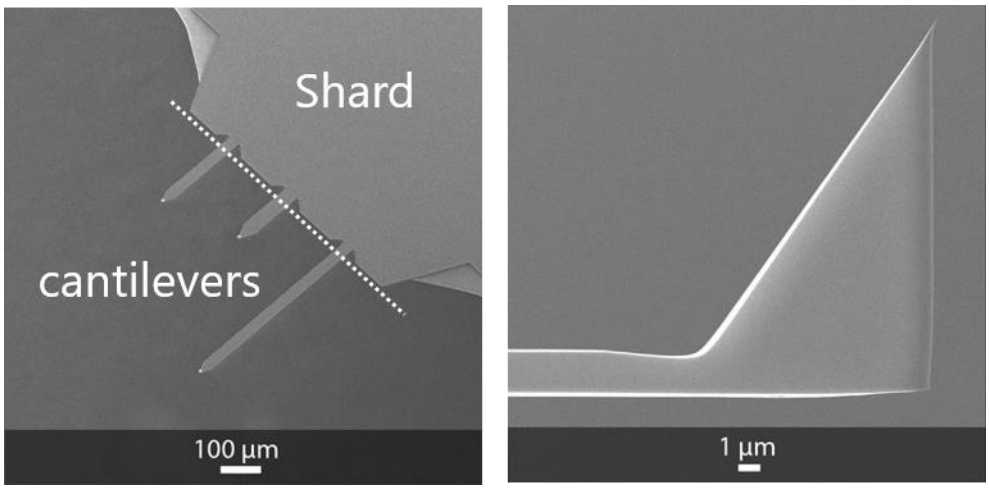

Figure 6.12 Manufacturer's SEM images of the AFM cantilevers used for near-field heating. The dotted line shows where the cantilevers are removed from the larger holding shard. The three cantilever lengths are 500 µm, 240 µm, 175 µm. The apex is specified to be < 30 nm. Figure from [200].

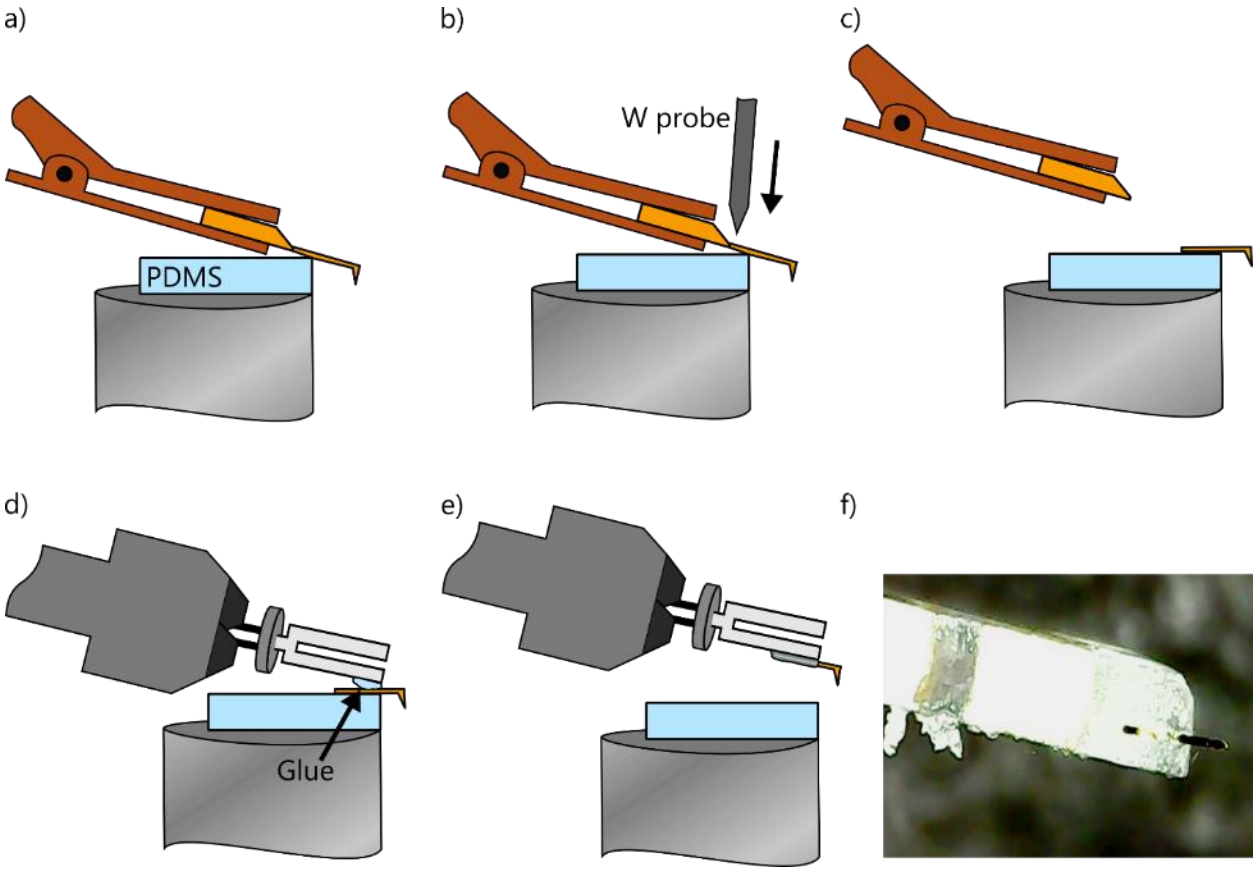

Figure 6.13 Process of attaching AFM cantilevers to tuning fork. a) The AFM cantilever is brought into contact with PDMS leaving the sharp point of the tip suspended. b) A W needle is brought down at the base of the cantilever to separate it from the shard. c) The shard is removed and the alligator clip is replaced with a pin-vise holding the tuning fork. d) Glue is applied to the tuning fork and it is brought into contact with the cantilever. e) The tuning fork is lifted off the PDMS. f) Tuning fork with an attached cantilever view under the microscope at 30x magnification.

We attach the cantilevers to the tuning fork by removing them from the shard then gluing them to the tuning fork. As shown in Figure 6.13, we first hold the back side of the AFM tip with a toothless alligator clip and use translation stages (ThorLabs, DT12XYZ) to bring it down onto a PDMS film on top of a one-inch diameter optical pedestal. The process is monitored with a microscope. The cantilever bends upwards when it is on the PDMS and the user will observe a dramatic change in reflection. Next, a 0.7 μm W-probe from an electrical probe station

(Signatone, SM-35) is brought down to break off the cantilever from the shard. Very little force is needed to break the cantilever at its base. After breaking off all the cantilevers from the shard, the alligator clip, and shard, is removed and replaced with a pin vise holding the tuning fork. A small amount of glue is applied to the tuning fork tine and the fork is lowered down onto the cantilever. After waiting fifteen seconds or so the tuning fork is lifted taking the cantilever with it. We inspect the result in an optical stereoscope, ideally the cantilever sticks straight out from the tuning fork and the tip should be pointing perpendicular to the tuning fork. Figure 6.14 shows a picture of the parts used to assemble the hybrid tuning fork/AFM scanning probe in. This is also the set up used to glue the etched gold wires to the tuning forks.

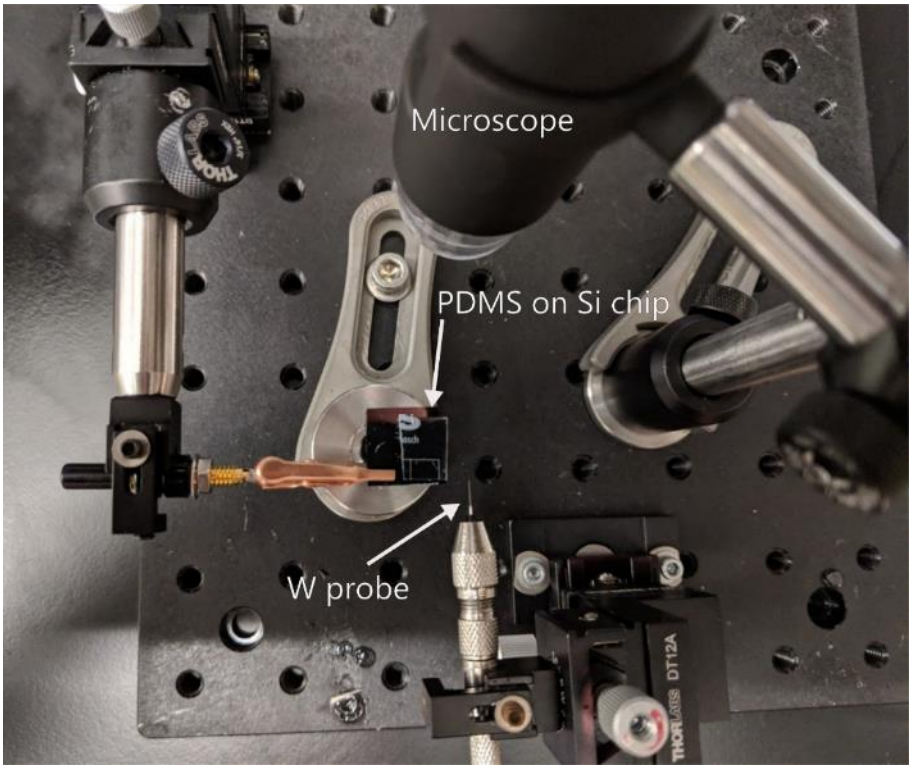

Figure 6.14 Photograph of the station used to attach the AFM cantilevers to the tuning fork and to glue the etched gold wires to the tuning forks.

We note that the length of the cantilever protruding from the end of the tuning fork should be kept short, roughly 5 μm, although out to ~100 μm may produce acceptable results. A

long cantilever does not effectively transfer force to the tuning fork and simply bends when it makes contact with the sample surface. Thus, a cantilever that is much too long will snap-in early during approach curves and the change in frequency versus tip-height will have a shallow slope. The other reason to keep the cantilever short is to ensure that it has a resonance above that of the tuning fork. Otherwise the vibration tuning fork may create unwanted oscillation of the cantilever that will complicate the measurement. The resonance of the AFM cantilever, ν, can be estimated by [201], $\nu \approx \frac{t}{2\,\pi\,l^2}\left(\frac{E}{\rho}\right)^{\frac{1}{2}}$ where t is the cantilever thickness, l is the cantilever length, E is Young's modulus, and ρ is the density.

6.4.3 The process of cutting a plasmonic grating with a focused ion beam

To improve the coupling of far-field light to propagating surface plasmon polariton (SPP) modes, a diffractive grating was cut on both the etched gold wires and gold-coated AFM tips. Details of the SPP coupling and results have been discussed in section 5.3. In this section we discuss the process used to cut the plasmonic gratings. We cut the grating in the plasmonic antenna using a combined SEM and focused ion beam, (FIB, FEI Strata 400 DualBeam). We use an ion beam current of 93 pA at 30 kV, although we found 0.46 nA could be used as well to increase the milling rate at the expense of slightly reduced edge quality. It typically took less than a minute to mill through the gold cone from the side if there was no drifting of the tip due to charging.

In practice, the orientation of the tip in the FIB contributed more to the outcome than the details of the beam. The SEM and FIB beams are oriented at 52° with respect to one another and the stage holding the tip can be tilted so that the surface of the platform holding the gold probe can be oriented perpendicular to either the SEM or the FIB. Figure 6.15 and Figure 6.16 show the two different orientations tested to make SPP coupling gratings.

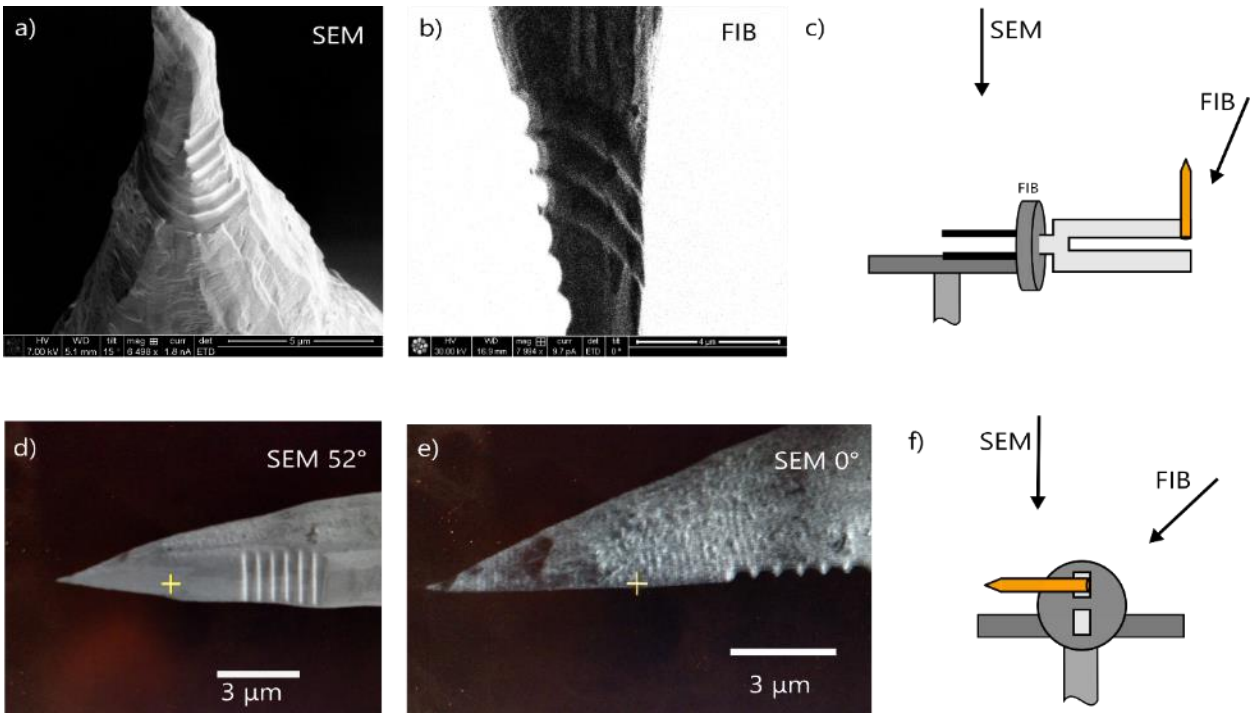

Figure 6.15 Orientation of etched gold wire and tuning fork for FIB cutting. a) SEM image of the etched gold wire after cutting the grating. b) Image taken using the Ga-ion beam after using the beam to cut the grating. c) Illustration of the tuning fork and tip orientation used to cut the grating shown in a) and b). d-e) SEM images of an etched wire after the grating was cut into it. The images were taken at 52° and 0°. f) Illustration of the orientation of the etched wire with respect to the SEM and FIB used to cut the grating shown in d) and e).

The first orientation tested for the etched wires was for tapping mode geometry tuning forks. The wire is glued to the tuning fork and the tuning fork leads are stuck to the FIB specimen holder so that the tip points vertically. Thus, the wire points towards the SEM beam and the FIB cuts the grating without tiling the sample stage. The result is a spiral pattern as shown in Figure 6.15a,b. The advantage to this orientation is that you can rotate the stage to cut all the way around the cone. The main disadvantage is that the alignment is very challenging, slow, and it does not work for the shear-mode geometry.

The second orientation for the etched gold wires is to align the long axis of the wire perpendicular to the SEM beam. To mill the grating the stage is tilted and a sinusoidal pattern is cut into the side. In this orientation, it is also possible to cut a rectangular region off of the side of the cone with the grating as was down in Figure 6.15d,e. This may produce a smoother plane for SPP propagation, however the propagation length has not been tested. This orientation works for both tapping and shear mode orientations, but good results rely on the wire being level with the sample stage. If the wire tilts down or upwards it creates problems with the focus and increases the risk is generating a touch alarm in the FIB system.

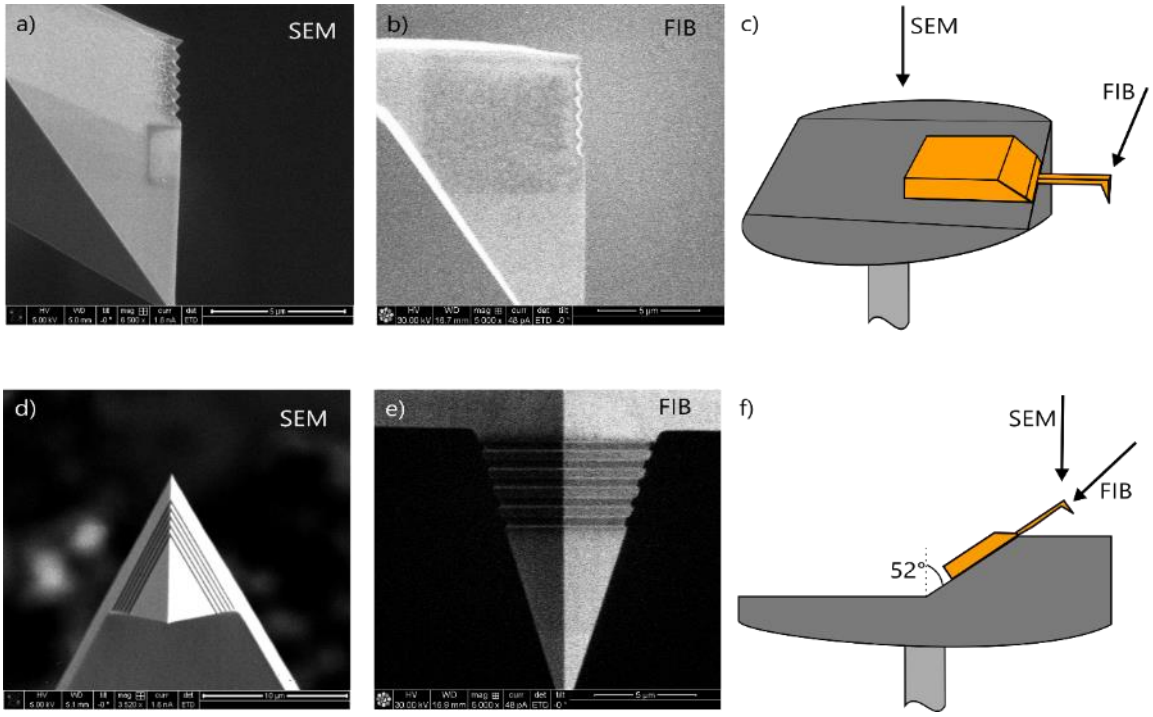

Figure 6.16 Orientation of AFM cantilever for FIB cutting. a) SEM image of the etched gold wire after cutting the grating. b) Image taken using the Ga-ion beam after using the beam to cut the grating. c) Illustration of the tuning fork and tip orientation used to cut the grating shown in a) and b). The AFM tip (shard and cantilever) is mounted on the face of a 52° specimen holder so that the FIB beam cuts across the side of the tip. d) SEM image of the etched gold wire after cutting the grating. e) Image taken using the Ga-ion beam after using the beam to cut the grating. f) Illustration of the orientation of the etched wire with respect to the SEM and FIB used to cut the grating shown

in d) and e), the The AFM tip is mounted on the face of a 52° specimen holder so that the front of the tip was facing the ion beam. The stage was not tilted for either the cutting or capturing the images.

We show the two orientations tested for milling gratings into the AFM, before gluing them to the tuning forks, in Figure 6.16. Both use a specimen holder that has a plane at a 52° angle. We stuck one AFM probe so that the ion beam was perpendicular to the side of the tip and one AFM probe so that the tip was perpendicular to the ion beam, see Figure 6.16c and Figure 6.16f respectively. For the first case, the beam cuts the same sinusoidal pattern used for the etched tips. This effectively cuts the correct shape but also removes, or damages, at the gold coating from the tip. The second orientation is cut by patterning rectangles across the face of the tip. This preserves the gold in the regions not milled and cuts a grating on both the front faces of the trigonal tip.

CONCLUSION

"Someone else always has to carry on the story"

– J. R. R. Tolkien, (Lord of the Rings)

In this dissertation, I have laid out the background and the technical development of both far-field and near-field magneto-thermal microscopy. In the far-field, a microscope objective focuses 3 ps laser pulses onto a magnetic structure. This creates a thermal gradient that transduces the local magnetization into a voltage via the anomalous Nernst effect, in ferromagnetic metals, or the longitudinal spin Seebeck effect in combination with the inverse spin Hall effect, in ferromagnetic insulators. We found that this technique can image magnetization with 10-100 ps temporal resolution, sub-micron spatial resolution, and sensitivity to the in-plane moment of 0.1°-0.3°/√Hz. Following the initial demonstration, we applied magneto-thermal microscopy to phase-sensitive ferromagnetic resonance imaging in ultrathin YIG/Pt bilayers. In the bilayers, we observed spatial variation of the resonance field, amplitude, phase, and linewidth despite the symmetry of the device and the epitaxial growth of the YIG. By comparing the images of dynamics to images of the static magnetization we concluded that spatially varying anisotropy could be responsible for the variation.

In the near-field implementation of magneto-thermal microscopy we use a sharp gold tip a few nanometers across to enhance the electric field and create a nano-sized thermal gradient. After testing etched gold wires in tapping and shear geometry and commercial AFM tips in tapping mode, we find the best results for commercial, gold coated silicon AFM tips. The scanning near-field TRANE microscopy had a sensitivity of 1.4°/√Hz sensitivity which enabled observation of magnetic domains in ultrathin CoFeB/Pt wires. Analysis of the domains indicates that the near-field magneto-thermal microscope is capable of resolution of 100 nm or less. These

results show that magneto-thermal microscopy has the potential to achieve table-top time-domain measurements of magnetic films and devices with resolution approaching x-ray techniques.

Both TRANE and TRLSSE stand out from other magnetic microscopy techniques for their sensitivity (at least in the far-field geometry) to the in-plane magnetic moment, their phase sensitivity, and their ability to be used quantitatively. These traits make TRANE and TRLSSE particularly well-suited to measuring thin-film magnetic devices. In addition, the geometry of the far-field magneto-thermal microscope is compatible with MOKE microscopy. Combining the two techniques could enable simultaneous detection with both magneto-thermal and magneto-optical microscopy. This could open the door to a wider range of samples or provide two independent techniques to corroborate the measurements.

On a more fundamental level, because magneto-thermal microscopy couples to magnetization differently than electron, stray-field, or optical effects, it can enable novel investigations. For instance, antiferromagnetic materials [202] may be imaged using magneto-thermal effects and spin-phonon coupling may be measured in ferromagnetic insulators [203]. Imaging with a thermal spot also enables simultaneous measurement of the excitation and the response. This could enable measurements of materials with anisotropic conductivity, quantification of spin torque angles, and quantification of the current density in the device.

BIBLIOGRAPHY

[1] M. N. Baibich, J. M. Broto, A. Fert, F. N. Van Dau, F. Petroff, P. Etienne, G. Creuzet, A. Friederich, and J. Chazelas, Phys. Rev. Lett. **61**, 2472 (1988).

[2] Seagate Technology LLC, *HAMR Technology*, seagate.com (2017)

[3] B. Dieny and I. L. Prejbeanu, in *Introduction to Magnnetic. Random-Access Memory*, (John Wiley & Sons, Inc, New York, 2017), pp. 101–164.

[4] C. L. Hogan, The Bell System Technical Journal, **31**, 1, (1952)

[5] S. I. Kiselev, J. C. Sankey, I. N. Krivorotov, N. C. Emley, R. J. Schoelkopf, R. A. Buhrman, and D. C. Ralph, Nature **425**, 380 (2003).

[6] S. Kaka, M. R. Pufall, W. H. Rippard, T. J. Silva, S. E. Russek, and J. A. Katine, Nature **437**, 389 (2005).

[7] T. Kampfrath, M. Battiato, P. Maldonado, G. Eilers, J. Nötzold, S. Mährlein, V. Zbarsky, F. Freimuth, Y. Mokrousov, S. Blügel, M. Wolf, I. Radu, P. M. Oppeneer, and M. Münzenberg, Nat. Nanotechnol. **8**, 256 (2013).

[8] T. Seifert, S. Jaiswal, U. Martens, J. Hannegan, L. Braun, P. Maldonado, F. Freimuth, A. Kronenberg, J. Henrizi, I. Radu, E. Beaurepaire, Y. Mokrousov, P. M. Oppeneer, M. Jourdan, G. Jakob, D. Turchinovich, L. M. Hayden, M. Wolf, M. Münzenberg, M. Kläui, and T. Kampfrath, Nat. Photonics **10**, 483 (2016).

[9] D. Rugar, H. J. Mamin, P. Guethner, S. E. Lambert, J. E. Stern, I. McFadyen, and T. Yogi, J. Appl. Phys. **68**, 1169 (1990).

[10] J. R. Kirtley, M. B. Ketchen, K. G. Stawiasz, J. Z. Sun, W. J. Gallagher, S. H. Blanton, and S. J. Wind, Appl. Phys. Lett. **66**, 1138 (1995).

[11] C. L. Degen, Appl. Phys. Lett. **92**, 243111 (2008).

[12] B. M. Chernobrod and G. P. Berman, J. Appl. Phys. **97**, 014903 (2004).

[13] G. P. Berman, A. R. Bishop, B. M. Chernobrod, M. E. Hawley, G. W. Brown, and V. I. Tsifrinovich, J. Phys. Conf. Ser. **38**, 167 (2006).

[14] J. A. Sidles, J. L. Garbini, K. J. Bruland, D. Rugar, O. Züger, S. Hoen, and C. S. Yannoni, Rev. Mod. Phys. **67**, 249 (1995).

[15] Z. Zhang, P. C. Hammel, and P. E. Wigen, Appl. Phys. Lett. **68**, 2005 (1996).

[16] D. Rugar, R. Budakian, H. J. Mamin, and B. W. Chui, Nature **430**, 329 (2004).

[17] M. E. Hale, H. W. Fuller, and H. Rubinstein, J. Appl. Phys. **30**, 789 (1959).

[18] A. K. Petford-Long and J. N. Chapman, in *Magn. Microsc. Nanostructures* (Springer, Berlin, Heidelberg, 2005), pp. 67–86.

[19] A. Feist, N. Bach, N. Rubiano da Silva, T. Danz, M. Möller, K. E. Priebe, T. Domröse, J. G. Gatzmann, S. Rost, J. Schauss, S. Strauch, R. Bormann, M. Sivis, S. Schäfer, and C. Ropers, Ultramicroscopy **176**, 63 (2017).

[20] N. R. da Silva, M. Möller, A. Feist, H. Ulrichs, C. Ropers, and S. Schäfer, ArXiv: 1710.03307 (2017).

[21] R. Wiesendanger, H.-J. Güntherodt, G. Güntherodt, R. J. Gambino, and R. Ruf, Phys. Rev. Lett. **65**, 247 (1990).

[22] S. Loth, S. Baumann, C. P. Lutz, D. M. Eigler, and A. J. Heinrich, Science **335**, 196 (2012).

[23] T. L. Cocker, V. Jelic, M. Gupta, S. J. Molesky, J. A. J. Burgess, G. D. L. Reyes, L. V. Titova, Y. Y. Tsui, M. R. Freeman, and F. A. Hegmann, Nat. Photonics **7**, 620 (2013).

[24] S.-C. Lee, C. P. Vlahacos, B. J. Feenstra, A. Schwartz, D. E. Steinhauer, F. C. Wellstood, and S. M. Anlage, Appl. Phys. Lett. **77**, 4404 (2000).

[25] C. A. Fowler and E. M. Fryer, Phys. Rev. **94**, 52 (1954).

[26] C. A. Fowler and E. M. Fryer, Phys. Rev. **104**, 552 (1956).

[27] E. Beaurepaire, J.-C. Merle, A. Daunois, and J.-Y. Bigot, Phys. Rev. Lett. **76**, 4250 (1996).

[28] X. Shi, P. Fischer, V. Neu, D. Elefant, J. C. T. Lee, D. A. Shapiro, M. Farmand, T. Tyliszczak, H.-W. Shiu, S. Marchesini, S. Roy, and S. D. Kevan, Appl. Phys. Lett. **108**, 094103 (2016).

[29] M. J. Robertson, C. J. Agostino, A. T. N'Diaye, G. Chen, M.-Y. Im, and P. Fischer, J. Appl. Phys. **117**, 17D145 (2015).

[30] P. Fischer, J. Phys. Appl. Phys. **50**, 313002 (2017).

[31] S. Eisebitt, J. Lüning, W. F. Schlotter, M. Lörgen, O. Hellwig, W. Eberhardt, and J. Stöhr, Nature **432**, 885 (2004).

[32] S. R. Boona, R. C. Myers, and J. P. Heremans, Energy Environ. Sci. **7**, 885 (2014).

[33] G. E. W. Bauer, E. Saitoh, and B. J. van Wees, Nat. Mater. **11**, 391 (2012).

[34] T. C. Harman and J. M. Honig, *Thermoelectric and Thermomagnetic Effects and Applications* (McGraw-Hill, Inc, New York, 1967).

[35] H. Callen, *Thermodynamics* (John Wiley & Sons, Inc, New York, 1960).

[36] H. B. Callen, Phys. Rev. **73**, 1349 (1948).

[37] T. Miyasato, N. Abe, T. Fujii, A. Asamitsu, S. Onoda, Y. Onose, N. Nagaosa, and Y. Tokura, Phys. Rev. Lett. **99**, 086602 (2007).

[38] T. C. Chuang, P. L. Su, P. H. Wu, and S. Y. Huang, Phys. Rev. B **96**, 174406 (2017).

[39] A. Slachter, F. L. Bakker, and B. J. van Wees, Phys. Rev. B **84**, 020412 (2011).

[40] A. Slachter, F. L. Bakker, and B. J. van Wees, Phys. Rev. B **84**, 174408 (2011).

[41] M. Schreier, A. Kamra, M. Weiler, J. Xiao, G. E. W. Bauer, R. Gross, and S. T. B. Goennenwein, Phys. Rev. B **88**, 094410 (2013).

[42] A. D. Avery, M. R. Pufall, and B. L. Zink, Phys. Rev. Lett. **109**, 196602 (2012).

[43] M. Weiler, M. Althammer, F. D. Czeschka, H. Huebl, M. S. Wagner, M. Opel, I.-M. Imort, G. Reiss, A. Thomas, R. Gross, and S. T. B. Goennenwein, Phys. Rev. Lett. **108**, 106602 (2012).

[44] F. Brandl and D. Grundler, Appl. Phys. Lett. **104**, 172401 (2014).

[45] K.-D. Lee, D.-J. Kim, H. Y. Lee, S.-H. Kim, J.-H. Lee, K.-M. Lee, J.-R. Jeong, K.-S. Lee, H.-S. Song, J.-W. Sohn, S.-C. Shin, and B.-G. Park, Sci. Rep. **5**, 10249 (2015).

[46] A. von Bieren, F. Brandl, D. Grundler, and J.-P. Ansermet, Appl. Phys. Lett. **102**, 052408 (2013).

[47] C. M. Jaworski, J. Yang, S. Mack, D. D. Awschalom, J. P. Heremans, and R. C. Myers, Nat. Mater. **9**, 898 (2010).

[48] K. Uchida, J. Xiao, H. Adachi, J. Ohe, S. Takahashi, J. Ieda, T. Ota, Y. Kajiwara, H. Umezawa, H. Kawai, G. E. W. Bauer, S. Maekawa, and E. Saitoh, Nat. Mater. **9**, 894 (2010).

[49] K. Uchida, H. Adachi, T. Ota, H. Nakayama, S. Maekawa, and E. Saitoh, Appl. Phys. Lett. **97**, 172505 (2010).

[50] J. E. Hirsch, Phys. Rev. Lett. **83**, 1834 (1999).

[51] S. Zhang, Phys. Rev. Lett. **85**, 393 (2000).

[52] L. Liu, T. Moriyama, D. C. Ralph, and R. A. Buhrman, Phys. Rev. Lett. **106**, 036601 (2011).

[53] S. O. Valenzuela and M. Tinkham, Nature **442**, 176 (2006).

[54] J. Xiao, G. E. W. Bauer, K. Uchida, E. Saitoh, and S. Maekawa, Phys. Rev. B **81**, 214418 (2010).

[55] S. M. Rezende, R. L. Rodríguez-Suárez, R. O. Cunha, a. R. Rodrigues, F. L. A. Machado, G. a. Fonseca Guerra, J. C. Lopez Ortiz, and A. Azevedo, Phys. Rev. B **89**, 014416 (2014).

[56] S. M. Rezende, R. L. Rodríguez-Suárez, and A. Azevedo, Phys. Rev. B **93**, 014425 (2016).

[57] K. An, K. S. Olsson, A. Weathers, S. Sullivan, X. Chen, X. X. Li, L. G. Marshall, X. Ma, N. Klimovich, J. Zhou, L. Shi, and X. X. Li, Phys. Rev. Lett. **117**, 107202 (2016).

[58] M. Schreier, A. Kamra, M. Weiler, J. Xiao, G. E. W. Bauer, R. Gross, and S. T. B. Goennenwein, Phys. Rev. B **88**, 094410 (2013).

[59] M. Schreier, F. Kramer, H. Huebl, S. Geprägs, R. Gross, S. T. B. Goennenwein, T. Noack, T. Langner, A. A. Serga, B. Hillebrands, and V. I. Vasyuchka, Phys. Rev. B **93**, 224430 (2016).

[60] M. Agrawal, V. I. Vasyuchka, A. A. Serga, A. Kirihara, P. Pirro, T. Langner, M. B. Jungfleisch, A. V. Chumak, E. T. Papaioannou, and B. Hillebrands, Phys. Rev. B **89**, 224414 (2014).

[61] B. L. Giles, Z. Yang, J. S. Jamison, and R. C. Myers, Phys. Rev. B **92**, 224415 (2015).

[62] J. Kimling, G.-M. Choi, J. T. Brangham, T. Matalla-Wagner, T. Huebner, T. Kuschel, F. Yang, and D. G. Cahill, Phys. Rev. Lett. **118**, 057201 (2017).

[63] J. M. Bartell, D. H. Ngai, Z. Leng, and G. D. Fuchs, Nat. Commun. **6**, 8460 (2015).

[64] J. Katine, F. Albert, R. Buhrman, E. Myers, and D. Ralph, Phys. Rev. Lett. **84**, 3149 (2000).

[65] S. Mangin, D. Ravelosona, J. a. Katine, M. J. Carey, B. D. Terris, and E. E. Fullerton, Nat. Mater. **5**, 210 (2006).

[66] A. M. Deac, A. Fukushima, H. Kubota, H. Maehara, Y. Suzuki, S. Yuasa, Y. Nagamine, K. Tsunekawa, D. D. Djayaprawira, and N. Watanabe, Nat. Phys. **4**, 803 (2008).

[67] S. I. Kiselev, J. C. Sankey, I. N. Krivorotov, N. C. Emley, R. J. Schoelkopf, R. A. Buhrman, and D. C. Ralph, Nature **425**, 1207 (2003).

[68] Y. Kajiwara, K. Harii, S. Takahashi, J. Ohe, K. Uchida, M. Mizuguchi, H. Umezawa, H. Kawai, K. Ando, K. Takanashi, S. Maekawa, and E. Saitoh, Nature **464**, 262 (2010).

[69] G. S. D. Beach, C. Nistor, C. Knutson, M. Tsoi, and J. L. Erskine, Nat. Mater. **4**, 741 (2005).

[70] A. Yamaguchi, T. Ono, S. Nasu, K. Miyake, K. Mibu, and T. Shinjo, Phys. Rev. Lett. **92**, 077205 (2004).

[71] Y. Acremann, J. Strachan, V. Chembrolu, S. Andrews, T. Tyliszczak, J. Katine, M. Carey, B. Clemens, H. Siegmann, and J. Stöhr, Phys. Rev. Lett. **96**, 217202 (2006).

[72] M. Madami, S. Bonetti, G. Consolo, S. Tacchi, G. Carlotti, G. Gubbiotti, F. B. Mancoff, M. a. Yar, and J. Åkerman, Nat. Nanotechnol. **6**, 635 (2011).

[73] M. R. Freeman and B. C. Choi, Science **294**, 1484 (2001).

[74] T. Trunk, M. Redjdal, A. Kákay, M. F. Ruane, and F. B. Humphrey, J. Appl. Phys. **89**, 7606 (2001).

[75] R. Allenspach, M. Stampanoni, and A. Bischof, Phys. Rev. Lett. **65**, 3344 (1990).

[76] X. Z. Yu, Y. Onose, N. Kanazawa, J. H. Park, J. H. Han, Y. Matsui, N. Nagaosa, and Y. Tokura, Nature **465**, 901 (2010).

[77] L. O. Brien, D. Petit, H. T. Zeng, E. R. Lewis, J. Sampaio, a. V Jausovec, D. E. Read, R. P. Cowburn, L. O'Brien, D. Petit, H. T. Zeng, E. R. Lewis, J. Sampaio, a. V Jausovec, D. E. Read, and R. P. Cowburn, Phys. Rev. Lett. **103**, 077206 (2009).

[78] a Ruotolo, V. Cros, B. Georges, a Dussaux, J. Grollier, C. Deranlot, R. Guillemet, K. Bouzehouane, S. Fusil, and A. Fert, Nat. Nanotechnol. **4**, 528 (2009).

[79] Y. Acremann, V. Chembrolu, J. P. Strachan, T. Tyliszczak, and J. Stöhr, Rev. Sci. Instrum. **78**, 014702 (2007).

[80] G. Y. Guo, Q. Niu, and N. Nagaosa, Phys. Rev. B **89**, 214406 (2014).

[81] M. Mizuguchi, S. Ohata, K. I. Uchida, E. Saitoh, and K. Takanashi, Appl. Phys. Express **5**, 093002 (2012).

[82] J. Weischenberg, F. Freimuth, S. Blügel, and Y. Mokrousov, Phys. Rev. B **87**, 060406 (2013).

[83] A. von Bieren, F. Brandl, D. Grundler, and J.-P. Ansermet, Appl. Phys. Lett. **102**, 052408 (2013).

[84] H. Schultheiss, J. E. Pearson, S. D. Bader, and a. Hoffmann, Phys. Rev. Lett. **109**, 237204 (2012).

[85] T. Suzuki, J. Appl. Phys. **40**, 1216 (1969).

[86] A. Yamaguchi, K. Motoi, A. Hirohata, H. Miyajima, Y. Miyashita, and Y. Sanada, Phys. Rev. B **78**, 104401 (2008).

[87] N. Mecking, Y. S. Gui, and C. M. Hu, Phys. Rev. B - Condens. Matter Mater. Phys. **76**, 224430 (2007).

[88] M. H. Kryder, E. C. Gage, T. W. Mcdaniel, W. A. Challener, R. E. Rottmayer, G. Ju, Y. T. Hsia, and M. F. Erden, Proc. IEEE **96**, 1810 (2008).

[89] W. A. Challener and V. Amit, in *Mod. Asp. Electrochem. No 44*, edited by M. Schlesinger (Springer, New York, 2009), p. 53.

[90] N. C. Emley, Magnetic Multilayer Nanopillars for the Study of Current-Induced Reversal of a Thin Magnetic Layer, Ph.D., Cornell University, 2005.

[91] Y. Q. Zhang, N. Y. Sun, R. Shan, J. W. Zhang, S. M. Zhou, Z. Shi, and G. Y. Guo, J. Appl. Phys. **114**, 163714 (2013).

[92] G. L. Eesley, Phys. Rev. B **33**, 2144 (1986).

[93] E. R. E. Dobrovinskaya, L. L. A. Lytvynov, and V. Pishchik, *Sapphire: Material, Manufacturing, Applications* (Springer, 2009).

[94] C. Ho, M. Ackerman, K. Wu, S. Oh, and T. Havill, J. Phys. Chem. Ref. Data **7**, 959 (1978).

[95] and H. P. J. W. D. Bonnenberg, K. A. Hempel, *See Notes* (n.d.).

[96] E. a Owen, E. L. Yates, and A. H. Sully, Proc. Phys. Soc. **49**, 323 (2002).

[97] J. M. Bartell, C. L. Jermain, S. V. Aradhya, J. T. Brangham, F. Yang, D. C. Ralph, and G. D. Fuchs, Phys. Rev. Appl. **7**, 044004 (2017).

[98] B. Behin-Aein, D. Datta, S. Salahuddin, and S. Datta, Nat. Nanotechnol. **5**, 266 (2010).

[99] K. Ganzhorn, S. Klingler, T. Wimmer, S. Geprägs, R. Gross, H. Huebl, and S. T. B. Goennenwein, Appl. Phys. Lett. **109**, 022405 (2016).

[100] C. W. Sandweg, Y. Kajiwara, A. V. Chumak, a. a. Serga, V. I. Vasyuchka, M. B. Jungfleisch, E. Saitoh, and B. Hillebrands, Phys. Rev. Lett. **106**, 216601 (2011).

[101] H. Kurebayashi, O. Dzyapko, V. E. Demidov, D. Fang, A. J. Ferguson, and S. O. Demokritov, Nat. Mater. **10**, 660 (2011).

[102] P. Pirro, T. Brächer, A. V. Chumak, B. Lägel, C. Dubs, O. Surzhenko, P. Görnert, B. Leven, and B. Hillebrands, Appl. Phys. Lett. **104**, 012402 (2014).

[103] K. Uchida, J. Xiao, H. Adachi, J. Ohe, S. Takahashi, J. Ieda, T. Ota, Y. Kajiwara, H. Umezawa, H. Kawai, G. E. W. Bauer, S. Maekawa, and E. Saitoh, Nat. Mater. **9**, 894 (2010).

[104] K. Uchida, H. Adachi, T. An, T. Ota, M. Toda, B. Hillebrands, S. Maekawa, and E. Saitoh, Nat. Mater. **10**, 737 (2011).

[105] S. R. Boona, R. C. Myers, and J. P. Heremans, Energy Environ. Sci. **7**, 885 (2014).

[106] V. E. Demidov, M. Evelt, V. Bessonov, S. O. Demokritov, J. L. Prieto, M. Muñoz, J. Ben Youssef, V. V. Naletov, G. de Loubens, O. Klein, M. Collet, P. Bortolotti, V. Cros, and A. Anane, Sci. Rep. **6**, 32781 (2016).

[107] D. A. Bozhko, A. A. Serga, P. Clausen, V. I. Vasyuchka, F. Heussner, G. A. Melkov, A. Pomyalov, V. S. L'vov, and B. Hillebrands, Nat. Phys. **12**, 1057 (2016).

[108] M. B. Jungfleisch, W. Zhang, J. Sklenar, J. Ding, W. Jiang, H. Chang, F. Y. Fradin, J. E. Pearson, J. B. Ketterson, V. Novosad, M. Wu, and A. Hoffmann, Phys. Rev. Lett. **116**, 057601 (2016).

[109] M. Montazeri, P. Upadhyaya, M. C. Onbasli, G. Yu, K. L. Wong, M. Lang, Y. Fan, X. Li, P. Khalili Amiri, R. N. Schwartz, C. A. Ross, and K. L. Wang, Nat. Commun. **6**, 8958 (2015).

[110] C. M. Jaworski, J. Yang, S. Mack, D. D. Awschalom, J. P. Heremans, and R. C. Myers, Nat. Mater. **9**, 898 (2010).

[111] J. Kimling, G.-M. Choi, J. T. Brangham, T. Matalla-Wagner, T. Huebner, T. Kuschel, F. Yang, and D. G. Cahill, ArXiv 1608.00702 (2016).

[112] S. Hoffman, K. Sato, and Y. Tserkovnyak, Phys. Rev. B **88**, 064408 (2013).

[113] T. Miyasato, N. Abe, T. Fujii, a. Asamitsu, S. Onoda, Y. Onose, N. Nagaosa, and Y. Tokura, Phys. Rev. Lett. **99**, 086602 (2007).

[114] N. Nagaosa, J. Sinova, S. Onoda, A. H. MacDonald, and N. P. Ong, Rev. Mod. Phys. **82**, 1539 (2010).

[115] S. R. Etesami, L. Chotorlishvili, and J. Berakdar, Appl. Phys. Lett. **107**, 132402 (2015).

[116] H. L. Wang, C. H. Du, Y. Pu, R. Adur, P. C. Hammel, and F. Y. Yang, Phys. Rev. B **88**, 100406 (2013).

[117] H. L. Wang, C. H. Du, Y. Pu, R. Adur, P. C. Hammel, and F. Y. Yang, Phys. Rev. Lett. **112**, 197201 (2014).

[118] J. T. Brangham, K.-Y. Meng, A. S. Yang, J. C. Gallagher, B. D. Esser, S. P. White, S. Yu, D. W. McComb, P. C. Hammel, and F. Yang, Phys. Rev. B **94**, 054418 (2016).

[119] T. Kikkawa, K. Uchida, Y. Shiomi, Z. Qiu, D. Hou, D. Tian, H. Nakayama, X.-F. Jin, and E. Saitoh, Phys. Rev. Lett. **110**, 067207 (2013).

[120] B. F. Miao, S. Y. Huang, D. Qu, and C. L. Chien, AIP Adv. **6**, 015018 (2016).

[121] D. Ellsworth, L. Lu, J. Lan, H. Chang, P. Li, Z. Wang, J. Hu, B. Johnson, Y. Bian, J. Xiao, R. Wu, and M. Wu, Nat. Phys. **12**, 861 (2016).

[122] F. Guo, J. M. Bartell, D. H. Ngai, and G. D. Fuchs, Phys. Rev. Appl. **4**, 044004 (2015).

[123] S. Wemple, S. Blank, J. Seman, and W. Biolsi, Phys. Rev. B **9**, 2134 (1974).

[124] D. L. Wood and K. Nassau, Appl. Opt. **29**, 3704 (1990).

[125] M. Schreier, T. Chiba, A. Niedermayr, J. Lotze, H. Huebl, S. Geprägs, S. Takahashi, G. E. W. Bauer, R. Gross, and S. T. B. Goennenwein, Phys. Rev. B **92**, 144411 (2015).

[126] T. Chiba, G. E. Bauer, and S. Takahashi, Phys. Rev. Appl. **2**, 034003 (2014).

[127] J. Sklenar, W. Zhang, M. B. Jungfleisch, W. Jiang, H. Chang, J. E. Pearson, M. Wu, J. B. Ketterson, and A. Hoffmann, Phys. Rev. B **92**, 174406 (2015).

[128] N. Vlietstra, J. Shan, V. Castel, B. J. van Wees, and J. Ben Youssef, Phys. Rev. B **87**, 184421 (2013).

[129] M. Weiler, M. Althammer, M. Schreier, J. Lotze, M. Pernpeintner, S. Meyer, H. Huebl, R. Gross, A. Kamra, J. Xiao, Y.-T. Chen, H. Jiao, G. E. W. Bauer, and S. T. B. Goennenwein, Phys. Rev. Lett. **111**, 176601 (2013).

[130] M. Althammer, S. Meyer, H. Nakayama, M. Schreier, S. Altmannshofer, M. Weiler, H. Huebl, S. Geprägs, M. Opel, R. Gross, D. Meier, C. Klewe, T. Kuschel, J.-M. Schmalhorst, G. Reiss, L. Shen, A. Gupta, Y.-T. Chen, G. E. W. Bauer, E. Saitoh, and S. T. B. Goennenwein, Phys. Rev. B **87**, 224401 (2013).

[131] N. Vlietstra, J. Shan, B. J. van Wees, M. Isasa, F. Casanova, and J. Ben Youssef, Phys. Rev. B **90**, 174436 (2014).

[132] C. Hahn, G. de Loubens, O. Klein, M. Viret, V. V. Naletov, and J. Ben Youssef, Phys. Rev. B **87**, 174417 (2013).

[133] S. H. Wemple, S. L. Blank, J. A. Seman, and W. A. Biolsi, Phys. Rev. B **9**, 2134 (1974).

[134] J. H. Weaver, Phys. Rev. B **11**, 1416 (1975).

[135] A. D. Rakić, A. B. Djurišić, J. M. Elazar, and M. L. Majewski, Appl. Opt. **37**, 5271 (1998).

[136] E. W. M. Haynes, editor , *CRC Handbook of Chemistry and Physics*, 97th Edition (CRC Press/Taylor & Francis, Boca Raton, FL.2017).

[137] A. M. Hofmeister, Phys. Chem. Miner. **33**, 45 (2006).

[138] A. E. Clark and R. E. Strakna, J. Appl. Phys. **32**, 1172 (1961).

[139] I. Dzyaloshinsky, J. Phys. Chem. Solids **4**, 241 (1958).

[140] F. Hellman, A. Hoffmann, Y. Tserkovnyak, G. S. D. Beach, E. E. Fullerton, C. Leighton, A. H. MacDonald, D. C. Ralph, D. A. Arena, H. A. Dürr, P. Fischer, J. Grollier, J. P. Heremans, T. Jungwirth, A. V. Kimel, B. Koopmans, I. N. Krivorotov, S. J. May, A. K.

Petford-Long, J. M. Rondinelli, N. Samarth, I. K. Schuller, A. N. Slavin, M. D. Stiles, O. Tchernyshyov, A. Thiaville, and B. L. Zink, Rev. Mod. Phys. **89**, 025006 (2017).

[141] X. Z. Yu, Y. Onose, N. Kanazawa, J. H. Park, J. H. Han, Y. Matsui, N. Nagaosa, and Y. Tokura, Nature **465**, 901 (2010).

[142] S. V. Aradhya, G. E. Rowlands, J. Oh, D. C. Ralph, and R. A. Buhrman, Nano Lett. **16**, 5987 (2016).

[143] G. E. Rowlands, S. V. Aradhya, S. Shi, E. H. Yandel, J. Oh, D. C. Ralph, and R. A. Buhrman, Appl. Phys. Lett. **110**, 122402 (2017).

[144] J. Rychły, P. Gruszecki, M. Mruczkiewicz, J. W. Kłos, S. Mamica, and M. Krawczyk, Low Temp. Phys. **41**, 745 (2015).

[145] A. V. Chumak, A. A. Serga, and B. Hillebrands, J. Phys. Appl. Phys. **50**, 244001 (2017).

[146] X. Chen, B. Dong, and O. Balogun, Int. J. Thermophys. **37**, 26 (2016).

[147] P. Ahn, X. Chen, Z. Zhang, M. Ford, D. Rosenmann, I. W. Jung, C. Sun, and O. Balogun, Sci. Rep. **5**, srep10058 (2015).

[148] Y. Yue, X. Chen, and X. Wang, ACS Nano **5**, 4466 (2011).

[149] A. V. Malkovskiy, V. I. Malkovsky, A. M. Kisliuk, C. A. Barrios, M. D. Foster, and A. P. Sokolov, J. Raman Spectrosc. **40**, 1349 (2009).

[150] T. J. Silva and S. Schultz, Rev. Sci. Instrum. **67**, 715 (1996).

[151] C. C. Neacsu, S. Berweger, and M. B. Raschke, NanoBiotechnology **3**, 172 (2007).

[152] C. Ropers, C. C. Neacsu, M. B. Raschke, M. Albrecht, C. Lienau, and T. Elsaesser, Jpn. J. Appl. Phys. **47**, 6051 (2008).

[153] C. C. Neacsu, S. Berweger, R. L. Olmon, L. V. Saraf, C. Ropers, and M. B. Raschke, Nano Lett. **10**, 592 (2010).

[154] S. Berweger, J. M. Atkin, R. L. Olmon, and M. B. Raschke, J. Phys. Chem. Lett. **1**, 3427 (2010).

[155] S. Berweger, J. M. Atkin, R. L. Olmon, and M. B. Raschke, J. Phys. Chem. Lett. **3**, 945 (2012).

[156] P. F. Liao and A. Wokaun, J. Chem. Phys. **76**, 751 (1982).

[157] W. A. Challener, C. Peng, A. V. Itagi, D. Karns, W. Peng, Y. Peng, X. Yang, X. Zhu, N. J. Gokemeijer, Y.-T. Hsia, G. Ju, R. E. Rottmayer, M. A. Seigler, and E. C. Gage, Nat. Photonics **3**, 220 (2009).

[158] J. C. Karsch, Sr. Thesis (2016).

[159] J. C. Karsch, J. M. Bartell, and G. D. Fuchs, APL Photonics **2**, 086103 (2017).

[160] B. Knoll and F. Keilmann, Opt. Commun. **182**, 321 (2000).

[161] P. Sandoz, J.-M. Friedt, and É. Carry, Rev. Sci. Instrum. **79**, 086102 (2008).

[162] P. J. James, M. Antognozzi, J. Tamayo, T. J. McMaster, J. M. Newton, and M. J. Miles, Langmuir **17**, 349 (2001).

[163] S. Davy, M. Spajer, and D. Courjon, Appl. Phys. Lett. **73**, 2594 (1998).

[164] F. Guo, J. M. Bartell, and G. D. Fuchs, Phys. Rev. B **93**, 144415 (2016).

[165] D. W. Pohl, W. Denk, and M. Lanz, Appl. Phys. Lett. **44**, 651 (1984).

[166] E. H. Synge, Lond. Edinb. Dublin Philos. Mag. J. Sci. **6**, 356 (1928).

[167] J. Bechhoefer, Rev. Mod. Phys. **77**, 783 (2005).

[168] D. W. Dye, Proc. Phys. Soc. Lond. **38**, 399 (1925).

[169] Nanonis GmbH, (n.d.).

[170] Am. J. Phys. **75**, 415 (2007).

[171] J. Otero, L. Gonzalez, and M. Puig-Vidal, Sensors **12**, 4803 (2012).

[172] R. D. Grober, J. Acimovic, J. Schuck, D. Hessman, P. J. Kindlemann, J. Hespanha, A. S. Morse, K. Karrai, I. Tiemann, and S. Manus, Rev. Sci. Instrum. **71**, 2776 (2000).

[173] T. Ludwig, J. Phys. Math. Theor. **41**, 164025 (2008).

[174] Y. Qin and R. Reifenberger, Rev. Sci. Instrum. **78**, 063704 (2007).

[175] J. Melcher, J. Stirling, and G. A. Shaw, Beilstein J. Nanotechnol. **6**, 1733 (2015).

[176] G. Qi and S. Zhang, J. Mater. Process. Technol. **68**, 288 (1997).

[177] K. Gall, J. Diao, and M. L. Dunn, Nano Lett. **4**, 2431 (2004).

[178] H.-J. Butt, B. Cappella, and M. Kappl, Surf. Sci. Rep. **59**, 1 (2005).

[179] B. Cappella and G. Dietler, Surf. Sci. Rep. **34**, 1 (1999).

[180] N. A. Burnham, R. J. Colton, and H. M. Pollock, Nanotechnology **4**, 64 (1993).

[181] K. Karrai and I. Tiemann, Phys. Rev. B **62**, 13174 (2000).

[182] M. J. Gregor, P. G. Blome, J. Schöfer, and R. G. Ulbrich, Appl. Phys. Lett. **68**, 307 (1996).

[183] D. Roy, C. M. Williams, and K. Mingard, J. Vac. Sci. Technol. B **28**, 631 (2010).

[184] S. Schmidt, B. Piglosiewicz, D. Sadiq, J. Shirdel, J. S. Lee, P. Vasa, N. Park, D.-S. Kim, and C. Lienau, ACS Nano **6**, 6040 (2012).

[185] A. J. Melmed, J. Vac. Sci. Technol. B Microelectron. Nanometer Struct. Process. Meas. Phenom. **9**, 601 (1991).

[186] B. Ren, G. Picardi, and B. Pettinger, Rev. Sci. Instrum. **75**, 837 (2004).

[187] C. Lefrou, *Electrochemistry: The Basics, With Examples* (Springer Berlin Heidelberg, Berlin, Heidelberg, 2012).

[188] J. P. Ibe, P. P. Bey, S. L. Brandow, R. A. Brizzolara, N. A. Burnham, D. P. DiLella, K. P. Lee, C. R. K. Marrian, and R. J. Colton, J. Vac. Sci. Technol. Vac. Surf. Films **8**, 3570 (1990).

[189] L. Libioulle, Y. Houbion, and J. -M. Gilles, J. Vac. Sci. Technol. B Microelectron. Nanometer Struct. Process. Meas. Phenom. **13**, 1325 (1995).

[190] M. Klein and G. Schwitzgebel, Rev. Sci. Instrum. **68**, 3099 (1997).

[191] L. Anwei, H. Xiaotang, L. Wenhui, and J. Guijun, Rev. Sci. Instrum. **68**, 3811 (1997).

[192] M. Kulawik, M. Nowicki, G. Thielsch, L. Cramer, H.-P. Rust, H.-J. Freund, T. P. Pearl, and P. S. Weiss, Rev. Sci. Instrum. **74**, 1027 (2003).

[193] D. Gingery and P. Bühlmann, Rev. Sci. Instrum. **78**, 113703 (2007).

[194] M. G. Boyle, L. Feng, and P. Dawson, Ultramicroscopy **108**, 558 (2008).

[195] M. M. Jobbins, A. F. Raigoza, and S. A. Kandel, Rev. Sci. Instrum. **83**, 036105 (2012).

[196] J. K. Schoelz, P. Xu, S. D. Barber, D. Qi, M. L. Ackerman, G. Basnet, C. T. Cook, and P. M. Thibado, J. Vac. Sci. Technol. B Nanotechnol. Microelectron. Mater. Process. Meas. Phenom. **30**, 033201 (2012).

[197] Y. Khan, H. Al-Falih, Y. Zhang, T. K. Ng, and B. S. Ooi, Rev. Sci. Instrum. **83**, 063708 (2012).

[198] B. W. Mao, B. Ren, X. W. Cai, and L. H. Xiong, J. Electroanal. Chem. **394**, 155 (1995).

[199] J. J. Lingane, J. Electroanal. Chem. 1959 **4**, 332 (1962).

[200] (https://www.opustips.com/en/afm-tip-3xc-gg.html).

[201] J. P. Cleveland, S. Manne, D. Bocek, and P. K. Hansma, Rev. Sci. Instrum. **64**, 403 (1993).

[202] S. M. Wu, W. Zhang, A. KC, P. Borisov, J. E. Pearson, J. S. Jiang, D. Lederman, A. Hoffmann, and A. Bhattacharya, Phys. Rev. Lett. **116**, 097204 (2016).

[203] T. Kikkawa, K. Shen, B. Flebus, R. A. Duine, K. Uchida, Z. Qiu, G. E. W. Bauer, and E. Saitoh, Phys. Rev. Lett. **117**, 207203 (2016).